Author:
Goren, Sevda

Title:
Development of an inversion method for the improved determination of the spatial distribution of radioactive materials using UAVs

Development of an inversion method for the improved determination of the spatial distribution of radioactive materials using UAVs

By

SEVDA GOREN

Department of Physics

University of Bristol

This dissertation submitted to the University of Bristol in accordance with the requirements of the degree of Research by Master OF SCIENCE IN PHYSICS.

OCTOBER 2019

Word count: 29007

The global population has been forecast to reach around 8 billion people by 2020, according to the World Bank. This rise will further increase the total global annual energy and resource demands. This population rise is tensioned against a recognised need to urgently decarbonise energy and transport systems to curb further greenhouse gas emissions and mitigate the magnitude of anthropogenic climate change. Although nuclear energy is one of the cleanest energy sources with respect to CO_2 emissions, it still carrier stigma, related to severe nuclear hazards such as the INES level 7 accidents at the Chernobyl Nuclear Power Plant (CNPP) and the Fukushima Daichii Nuclear Power Plant (FNPP) since large amounts of radiological contamination were released into the environment and its impact was felt globally. In retrospect, the response to the CNPP and the FNPP events would have been much quicker and better informed if radiation mapping technologies were more advanced and available; especially unmanned aerial vehicles (UAVs). Therefore, a novel UAV system and an inversion method has been developed to analyse radiometric data for determining the location of radioactive contamination caused by nuclear power plant releases with high spatial resolution. The radiometric datasets were acquired in the Chernobyl Exclusion Zone of Ukraine because of distribution of Cesium-137. The data were measured in total counts per second for airborne and ground surveys. Three-dimensional geographical data were used to define the location of each radiometric surveys. The processing workflow was designed by testing Algebraic Reconstruction method (ART), Karcmarz algorithms, and parameters, to find the optimal processing solution. The processing steps included generating a 3D elevation model derived from geographical data, before numerically accounting for the predicted on-the ground radiation field by back-working (inverting) for geometrical dilution (inverse square law) and attenuation by air. Data processing was coded in MATLAB and executed using the University of Bristol supercomputer. The final radiation maps derived from a novel hyperspectral gamma imaging (HSGI) technique by using ART method achieved high spatial resolution. Combining the results of the processed radiometric data obtained by UAVs and in-situ from the same areas allows for comparison and confirmation of the high spatial distribution of the contaminant sources on the ground.

I would like to thank my supervisor, Prof. Thomas B. Scott, and especially Dr. David Megson-Smith, MSc. Dean Connor, Dr. Kieran Wood, Dr. Peter Martin, Dr. Yannick Verbelen of University Bristol for their unlimited information and supports during my research.

I greatly appreciate Andres Tovar, Associate Professor at Indiana University-Purdue University Indianapolis (IUPUI), for sharing his MATLAB code with me and explaining it in detail.

I am grateful to The Republic of TURKEY, Ministry of National Education, for providing me the financial support to undertake this research in the UK.

I am so thankful to my mother, my father and my identical twin sister for their support, Fatma Goren, Emin Tamer Goren and Ferda Goren are always there when I need them. Thank you to all my relatives and friends for encouraging me at every step in my life.

DECLARATION OF RECEIVED ASSISTANCE

I declare that the work in this dissertation was carried out in accordance with the requirements of the University's Regulations and Code of Practice for Research Degree Programmes and that it has not been submitted for any other academic award. Except where indicated by specific reference in the text, the work is my own work. Work done in collaboration with, or with the assistance of, others, is indicated as such. I have identified all material in this research by master which is not my own work through appropriate referencing and acknowledgement. Any views expressed in the dissertation are those of the author.

SIGNED: ..... DATE:.....

FNPP Fukushima Daicihii Nuclear Power Plant

CNPP Chernobyl Nuclear Power Plant

UAVs Unmanned Aerial Vehicle Systems

ART Algebraic Reconstruction Technique

HSI Hyperspectral Imaging

HSGI Hyperspectral Gamma Imaging

UK United Kingdom

CEZ Chernobyl Exclusion Zone

INES International

ISL Inverse Square Law

REE Rare Earth Elements

ER Exposure Rate

ADR Absorb Dose Rate

NKS Nordic Nuclear Safety Research Secteriats

IAEA International Atomic Energy Association

SRS Savannah River Site

GM Geiger- Muller

MDA Minimum Detectable Activity

GR Ground

CBRN Chemical Biological Radiological Nuclear

GNSS Global Navigation Satellite System

RPAS Remotely Piloted Aircraft Systems

NIR Near-infrared

SWIR Short-wave infrared

SPRD Spectroscopic Personal Radiation Detector

AGRS Airborne Gamma-Ray Spectrometry

TWI Topographic Wetness Index

XRD X-ray Powder Diffraction

GPS Global Positioning System

IDW Inverse Distance Weighting

GS Hand-held Spectrometer

AS Airborne Spectrometer

TAS Traditional Airborne Spectrometer

NORM Naturally Occurring Radioactive Material

AGL Above Ground Level

DEM Digital Elevation Model

DTM Digital Terrain Model

RBE Recursive Bayesian Estimation

MLE Multi Linear Estimation

Eq Equation

WNA World Nuclear Association

UTM Universal Transverse Mercator

WGS	World Geodetic System
NW	North West
GNSS	Global Navigation Satellite System
IMU	Inertial Measurement Unit
LIDAR	Light Detection and Ranging
NBA	Network Bundle Adjustment
BGS	British Geological Survey
2D	2-Dimensional
3D	3-Dimensional
LiPo	Lithium Polymer
N	North
E	East
W	West
S	South
eU	Equivalent Uranium
eTh	Equivalent Thorium
eK	Equivalent Potassium
Bq	Becquerel
m	metres
cm	centimetres
µSv/h	mikroSievert per hour
keV	kiloelectronVolt

cps	counts per seconds
MeV	megalectronVolt
γ	Gamma-ray
ppm	parts per million
mg/g	milligram per gram

1. INTRODUCTION

Radioactivity, which is a ubiquitous physical property in minerals and rocks can be defined by unprompted changes in atomic structure to regain nuclear stability. Radioactivity was first reported by Becquerel in 1896 (Malley, 2011) although firstly, it was discovered by Rontgen in 1895 (Malley, 2011). Its discovery has since prompted academia and associated organisations to discover a plethora of novel radioactive elements/isotopes as well as many different methods for detecting radiation produced by these.

A significant number of radioactive elements are found in most rocks and sediments on the Earth`s surface. Natural radionuclides, especially uranium (^{238}U), thorium (^{228}Th), potassium (^{40}K) and their decay-chain daughter isotopes, have a spectacular importance for understanding the evolution of the Earth and the timescale for cyclic terrestrial solar processes. From a more industrial perspective, radiometric surveys in geophysical applications started with petroleum exploration in boreholes using Geiger-Muller detectors invented in 1928 (Rutherford et al., 1908; Muller, 1928). After proving useful results, further innovation delivered more sensitive scintillation detectors based on the property of luminescence, which gained attention in 1944 because of dead time reduction in Geiger Muller detectors for drilling activities. Scintillation detectors have subsequently been used for geological mapping, mineral exploration and nuclear test applications over many decades. Gamma ray spectrometers, which can distinguish radioactive isotopes depending on their energy of their photon emissions, subsequently appeared from the mid-1960s. This technology advancement marked a step change among from simple measuring of gamma intensity to profiling the contributing radioisotopes.

The global population is expected to reach around 8 billion people by 2020 increasing total energy demands (Nygaard, 1994). This population rise is tensioned against a recognised need to urgently decarbonise energy and transport systems to curb further greenhouse gas emissions and mitigate the magnitude of anthropogenic climate change (Grimes and Nutall, 2010: Marcus and Levin, 2002; Nuttall, 2005). Although nuclear energy is one of the cleanest energy sources with respect to CO_2 emissions, it still carries stigma, related to severe nuclear hazards such as the INES level 7 accidents at the

Chernobyl Nuclear Power Plant and the Fukushima Daichii Nuclear Power Plant since large amounts of radiological contamination were released into the environment and its impact was felt globally. In retrospect, the response to the both events would have been quicker and better informed if available radiation mapping technologies had been more advanced and capable; especially unmanned aerial systems (UAVs) since mapping the radiation spread in the fallout was performed by men on the ground and in helicopters.

Over recent years, there has been a growing interest in UAVs in the research community, but also in numerous applications for industry, defence and emergency response. Their use as an alternative to on-the-ground first responders is potentially significant, as they can provide situation awareness information rapidly, remotely and with high detail, keeping emergency workers better informed and invariably safer (Dong et al. 2014). Moreover, multi-rotor UAVs, which are now commonplace versus the original single rotor UAVs are inherently simpler by mechanical (and electrical) design, providing enhanced safety and manoeuvrability with a concurrent reduction in operating expenses (Zhang et al. 2014). For environmental surveying, multi-rotor UAV's are therefore highly advantageous versus expensive manned aerial surveys or on-the-ground teams which are hampered by terrain and speed (Hatch, 2016, 2017; Niedzielski, 2018).

Airborne gamma-ray surveying has historically been utilised for detection of surface-outcropping radioactive ore bodies (IAEA, 1991, 2013; Fortin et al., 2017) and demonstrated for use in radio-tracing studies where phenomena such as sedimentation and material transport rates can be investigated (IAEA, 1991). In many geophysical studies using radiometric surveys, the main goal is to determine the major geological formations in an area and then to focus on individual radioelement patterns that may reveal specific features of significance such as an ore body or fault line. For such discrimination, gamma spectroscopy has been essential (for example facilitating the differentiation of a deposit rich in potassium from another rich in thorium or uranium). All such studies show rely on the fact that all rocks have inherent radioactivity, which varies according to their composition and age. For example, many coal measures could be classified as ultra-low grade uranium ore deposits based on the presence of uranium in organic material (of which the coal is originally composed) which is a chemical and

redox scavenger of aqueous uranium from percolating groundwater (Burns et al., 1999) The most important difference of thorium rather than uranium is far less mobile in oxidising surface conditions (Mernagh and Miezitis, 2008).

The following review provides an insight into the utilisation of UAV's for plant, environmental surveying and ore bodies of gamma radiation, examining the advantageous physics of using UAVs juxtaposed with issues around sensor weight versus sensitivity and flight time.

An excellent general example of airborne radiometric surveying for highlighting the regional geology of an area is that provided by the TELLUS South West project (2014) which radiometrically mapped the whole of Cornwall in the UK [1]. This British Geological Survey (BGS) study represents the most comprehensive and highest spatial resolution regional survey ever conducted with the results (see figures below) highlighting many of the significant geological features of the region, including major fault lines and granite exposures.

Figure 1. A twin-engine Rheims Cessna F406 aeroplane, fitted with geophysical radiometric survey equipment, used in the Tellus South West survey. Photo courtesy of Fugro Airborne Surveys (Pty) Ltd.

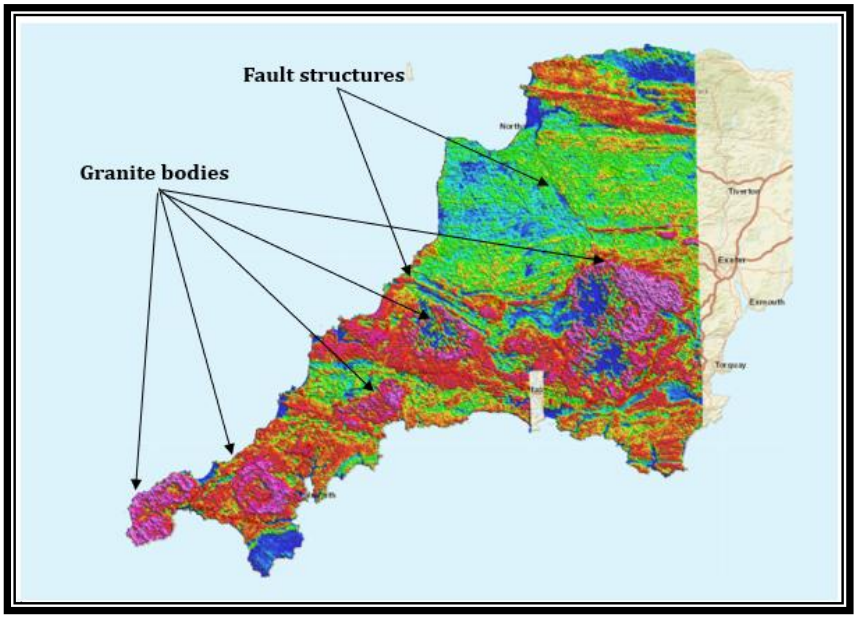

Figure 2. A colour-scaled radiation intensity map of Cornwall recorded by the Tellus SW project (2014)

Moreover, a notable example of Turkey has uranium (9.129 tonnes) and thorium reserves with Barite, Fluorite and Rare Earth Elements (REE) in Kizilcaoren near to Sivrihisar – Eskisehir in Central Anatolia , which are the largest radioactive Thorium resource (13.8%) in the world (Uzmen, 2015). Other thorium reserves are located in Malatya-Darende - Kuluncak, Kayseri - Felaye, Sivas and Diyarbakir. According to the studies carried out by General Directorate Mineral Research and Exploration (MRE), domestic thorium reserves was found to be 380000 tons of ThO_2 containing ores with approximately 0.21 wt.% ThO_2 (Figure 3).

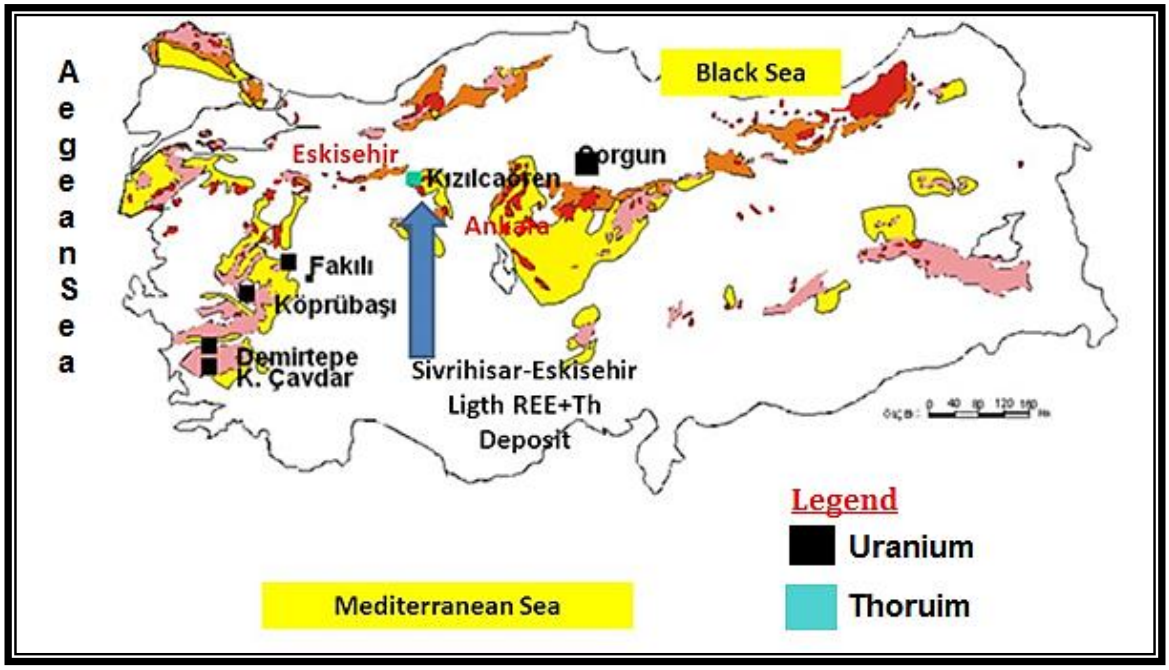

Figure 3. Uranium and Thorium Resources of Turkey modified from [2]

After the Kyoto Protocol , Turkey has sensibly committed to a carbon – free future for electricity generations including the building of several nuclear reactors related to their the total rare earth elements (REE) reserves. Therefore, Turkey requires new UAV systems and methodologies to scan radioactive ore bodies on the ground quickly and to produce high spatial resolution radioactive intensity maps.

This research is to investigate the development of “next generation” methodologies for radiation mapping using UAVs. It describes a new physical methodology of airborne surveys (multi-pass surveys) and a new statistical method of radiometric data processing (a novel inversion algorithm using hyperspectral gamma imaging technique), which have been developed as part of this project to deliver a marked improvement in on-the-ground accuracy for detecting and localising radiation anomalies of Chernobyl nuclear sites in Ukraine. According to the key findings in this research, they will shed light on applications of airborne radiometric survey for discovering new energy sources in Turkey.

1.1. Literature Review

UAV's were utilised at a surprisingly early stage for conducting such surveys, initially using large radio-controlled helicopters with no autonomous capability. For example, in the beginning of the 1960s, Uranium deposits in the Sokolov Tertiary sedimentary basin, Czech Republic were found by single-rotor UAVs. Lo and Pitcher (1996) discovered a potassium deposit in the Ashanti Belt, Ghana but using manual ground-based methods. Bierwirth et al. (1996, 1997) did a research by using airborne radiation mapping techniques for determining soil properties near to Batlow, Australia. According to their results, acid solutions and imaging of potassium (K) are indicators for the determination of aluminium toxicity and low K values indicates geomorphological inactive soils. Moreover, authors could not find any useful correlation between clay content and Th rates because of the several types of clay in the survey site. The low Th zones in their maps were related to montmorillonite group clays. Kaolinite and illite formations were found at high Th zones. It is also understood that the presence of Rn gas from cracks in the soil may reduce the detection of daughter isotopes in ^{232}Th and ^{238}U chains. The down-water movement was a main cause of the replacement of K and Th. K (>1.4%) and Th>15 ppm shows sedimentary depositions, include high thickness of silt. Furthermore, the value in this research was shown the deposition of wind-blown clays or parna. Dickson and Scott (1997) investigated the distribution of radioactive elements in the upper few meters in eastern Australia. Interpretation of conclusions is associated with critical understanding of weathering conditions in soil layers. They made a big step for direct detection of Uranium and Thorium and other ore mineralization due to K- alteration derived from gamma ray spectrometry. Versteeg and Peterson (1997) showed that distinguishability of igneous rocks from kimberlite silts in the Guaniamo area of Venezuela depend on high levels of K, U, Th by using airborne radiometric data. Furthermore, applicability of gamma-ray surveys within igneous formations had been searched out by Broome et al. (1987) and Schetselaar (2002). Aydin et al. (2016) observed

petrochemical assessments of the volcanic and plutonic associations of Central Anatolia (Turkey) conduct to aerial gamma spectrometry. The survey data on acidic intrusions (i.e, granite, monzonite and syneite) have revealed high occurrence of potassium (K), uranium (U) and thorium concentrations. Turhan et al. (2011) prepared the background gamma dose rate of the Çanakkale region, Turkey by using car-borne survey. After that, Uyanik et al. (2011) reported a ground radiometric survey in Turkey by using NaI(Tl) detector and their results are shown that radioelement concentrations of Cünür Hill in Turkey are high because of its trachyandesitic composition, while those measured in the limestone area were low. Beamish (2014) from the British Geological Survey (BGS) presented six radiometric surveys in the UK, done between 1998 and 2013 using an unmanned platform (fixed wing), assessed with actual soil sampling and hand-held measurements of exposure levels. Moreover, this survey examined lots of UK`s lithology and gave a huge knowledge about sources of radioactivity levels in England. This study measured high dose values caused by former industrial activities, such as Uranium mining operations. Then, Martin et al. (2015) developed a novel unmanned aerial system and tested in legacy Uranium mineral veins within Cornwall, England. This tool` succeeded to prepare high spatial resolution maps for all kinds of radioactive scenarios in the world. Moreover, Kaiser et al. (2014) wanted to search the propagation of black sand on Rosetta coastal zone, Egypt started from 1990 by using a plane with 256 channel gamma ray spectrometers. After data collection, exposure rate (ER) and absorbed dose rate (ADR) were calculated. Their results in 2013 were over the universal limits for long period exposure and the highest radioactive regions in amounts of Uranium and Thorium have given the most radioactive heating values that's why their research needs more monitoring because of sea wall construction on the coastal area led to alterations of black sand deposition. Adopting the new developments for radiometric data analysis and remote sensing systems make the differences in geological formations on the interest areas more clear. Uyanik et al. (2015) studied natural thorium concentrations of southwestern of Turkey by using a portable gamma-ray spectrometer and the highest concentration values were obtained from volcanic rocks (Pliocene alkaline basalts). Pirttijarvi` survey report (2016) showed a novel UAV system, spectrometer, test flights and total intensity of gamma radiation\ the intensity of the energy windows upon K, Th, U windows in Rautavaara mine, Kolari. This report wanted to see the general capacity of

their system without some correction steps used in radiometric surveys. It can clearly be seen that results in this project matched the same geological background in survey area. Ochi et al. (2017) found a new simple equation to estimate the vertical distribution of radiocesium in soil by using radiometric data derived from UAV in Japan instead of soil sampling. Cinar et al. (2017) characterized the radioactive levels in northeastern part of Turkey on Sarihan plutons with in-situ spectrometer and their paper reported that the highest value of eU/K and eTh/K were obtained in the Ophiolotoc olistostromal melange in Sarihan plutons. Falciglia et al. (2017) performed a computable identification for ^{241}Am and ^{152}Eu by using UAVs with a cadmium telluride semiconductor (CdTe) detector and the altitude (h), inclination (θ) and detection time were investigated as flight parameters. H and θ were selected as 0 cm – 70 cm and 0°–60°, respectively. Authors believe that previous studies did not cover enough calibrated data, caused wrong radioactivity level interpretations, and emphasized the importance of the parameters above. Detection efficiency and minimum detectable activity concentration were checked at the lab-scale in terms of parameters above, considering ^{241}Am and ^{152}Eu as simulated soil contaminants and analysed due to the reference levels. According to their results, preliminary data can detect these radioisotopes above given parameter values. Mattila et al. (2018) looked for estimation of terrain mobility using topographic wetness index (TWI) and airborne radiation data for Th. According to their results, soil type can be detected by radiation results, Th values can interpret wet places labelled as sandy till and illustrates changes in rut depth. Pires and Carmelo (2018) managed to minimize the lithological background contribution in mineral exploration by using statistical analyses of uranium sources via airborne data. Gatis et al. (2019) explored a new and functional correlation to map upland depth of peat (carbon stored areas), without previous information, using airborne gamma ray and LIDAR information in Dartmoor National Park, UK. Amara et al. (2019) succeeded to produce a new geological map from airborne geophysical data to prove the big changes in the Tefedest Terrane, Algeria.

After big nuclear accidents, most countries have concentrated on environmental applications of airborne UAV surveys include assessing the health risks associated with radon in houses as well as environmental radioactive pollution and emergency response – with ^{137}Cs representing the primary indicator of a nuclear power plant disaster release.

However, detection efficiency and minimum detectable activity (MDA) concentration must significantly be determined for these applications (Tang et al. 2016). There were a lot of studies, about environmental radioactive surveys based on UAV systems, done by several researchers and IAEA in the past.

Hofstter (1994) explained radiation levels in Savannah River Site (SRS), include surface water measurements, mobile laboratory actions, atmospheric radionuclide concentrations, soil sampling, aerial and handheld scanning. Shives et al. (1995) mapped ^{60}Co in sediments along cooling discharge veins in Bulgaria. Tyler (1996) revealed that spatial variability is an essential parameter to determine environmental radioactivity from soil sampling and in-situ\airborne gamma spectrometry. A hexagonal sampling methodology was used to estimate ^{137}Cs values in Glasgow, so soil samples and aerial surveys were compared effectively. After this paper, The RESUME project (1997), included eight countries by using ten airborne and seven vehicle teams, performed by The Nordic Nuclear Safety Research Secteriat (NKS) and published by NKS and Karlsson et al. (2000) with high resolution maps of ^{137}Cs. Although Toivonen (1997) explained that Sodium Iodide (NaI) detectors provide an advantage to detect hidden sources rather than Height Purity Germanium (HPGe) detectors, he suggested that usage of two detectors can be functional in such a project. Sanderson et al. (1997, 2008) checked the effectiveness of track line arrays (between 50 and 500 m) by using big helicopters over radioactive sources (^{137}Cs) and characteristics of gamma-ray spectrometry data in NW England and Scotland. They emphasised that the geological structure of the ground is the initial factor for planning of survey. Grasty (2001) examined radioactive fallouts which are in normal levels, so they managed to stop people` fears caused by the existence of a nuclear power plant in Canada. Kurvinen et al. (2005) developed a prototype that included Geiger Muller (GM), NaI(Tl) and CZT detectors for scanning a radioactive plume and searching point sources on the ground in Finland. It is understood that this prototype opened new doors for all experts. Furthermore, Bollhofer et al. (2008) did an airborne survey in a historic mine of Australia and reported limited radioactive areas, especially in mine and low-grade waste rock dumps considering as equivalent uranium (eU) values. Radiation levels will be reduced by decontamination action plans in searched areas. After the Chernobyl accident happened, Pollanen et al. (2009) searched Cs and Ir values with air sampling and

gamma ray measurements (from cps to external dose rates) with a commercial detector method mounted on UAV. Tests showed that this system could collect airborne radioactive particles and ^{214}Pb \$^{214}$Bi `s peaks could be seen in the gamma-ray spectra.

The Airborne Radiation Monitoring Project by the Ministry of Education, Culture, Sports, Science Technology and the U.S Department of Energy in 2011 helped understanding of radioactive plumes directions after Japan nuclear disasters for important authorities (IAEA, 2011 to 2017). Knoshita et. al. (2011) showed the geographical variations of radioactive iodine, tellurium and cesium on the ground by using a gamma-ray spectrometer for central east Japan from March 15 to March 21. Cresswell et al. (2012) demonstrated lightweight gamma spectrometry systems, discussed their effectivity on urban environments in the UK, developed by SUERC in Glasgow for the presence of ^{137}Cs. Their tool was used to scan complex surfaces in the UK. Bogatov et al. (2013) designed a radiation survey device used a NaI(Tl) detector and 2 Geiger Muller counters mounted on UAV for Cs. This tool could detect surface contamination of 10 Bq/m^2 from 100 m above the ground. Sanada and Torii (2014) calculated distribution of air doses rate as 1m above surface and the cesium levels on the ground were determined by using a LaBr3: Ce detector by using UAVs in this paper. The reason of existence of radioactive releases was explained as FDNPP. Xu et al. (2015) tested four different airborne survey systems, three different survey heights and ground based gamma spectrometry in Japan so their results showed that nuclide specific inventories of airborne and ground data matched each other properly. Zabulonov et al. (2015) tested to find a hidden radioactive waste in Chernobyl Exclusion Zone by using octocopter UAV type dependant on searching flight parameters and contouring methods. Their article presented that there is a significant negative effect on ^{137}Cesium measurements due to high and thick vegetation in survey area. Beresford et al. (2016) identified specific areas in Chernobyl in terms of the importance of semi-natural ecosystems in human dose formations, the characterization and physical behaviour of dangerous particles, bioavailability of radiocesium and the effects of radiation on plants and animals. After a year, they outlined reasons influencing dose rates on different wildlife groups located in Chernobyl Exclusion Zone. Sanada et al. (2016) highlighted UAVs advantages for estimating temporal variation of dose rate distribution and discussed radiation monitoring tools around Fukushima Daiichi nuclear power

station. Martin et al. (2016) investigated mobility of radioactive plumes by using 3D unmanned aerial vehicle radiation mapping methodology on rice paddy fields in Japan so their results claimed that fallout material was not stable and is necessary to follow their pathways for years. Martin and Scott (2016) tried to overcome the misunderstanding of natural Uranium levels in particles around Fukushima Prefecture with electron microscopy at the nanoscale. Moreover, high resolution radiation mapping was done by using multi-rotor system with SIGMA-50 detector operating at low survey altitudes on a Japanese waste storage facility (Connor et al., 2018). Air dose rates (μSv\h) were visualized in 3D and the advantages of rendering radiation intensity in 3D were raised and discussed. Burtniak et al. (2017) monitored highly radioactive regions in Chernobyl by using GR-Smart System (Ground-Smart System). Their results found even very small radioactive sources in their area of interest. Hultquist et al. (2017) aimed to validate radiation measurements using GM counters collected by citizens in Japan. Their results suggested that usable data for nuclear investigations can be obtained from non-traditional and unchecked sources such as local science projects. Mochizuki et al. (2017) demonstrated the use of an aerial imaging drone by using a Compton camera in a schoolyard of Fukushima. This system decreased data collection time by a factor of ten versus ground surveys in difficult areas. Sato et al. in 2018 developed a remote sensing system using a Compton camera and multi-rotor drone in the Hamadori region of Fukushima, Japan. This novel system measures sensitive radioactive distribution quickly. Connor et al. (2018) prepared radioactivity maps for waste storage sites filled with large volumes of material from the stripping of the land surface during the clean-up operations of Fukushima. The authors performed multiple surveys at different times during the construction of the site. They showed a distinct change in dose rate between the two surveys. The differences in dose-rate can be seen from their results easily. Gabrlik et al. (2018) concentrated on localization simulations of radiometric measurements by using both terrestrial robot data and UAVs measurements for sources of Cesium. They concluded that using robots for estimation of radioactive levels would give high quality results for complex terrains. Malins et al. (2018) calculated ambient dose-rate depending on topographic effects for radiocesium fallout. Their outcomes confirmed that surface angles and unconformity in soils are highly considerable issues for determining true values of air dose rates.

More recently, as a result of advancement in detector technology, UAVs have been utilised for soil texture (composition) mapping. Clay content in soils is a vital parameter for productivity of crop rotations. The primary radionuclides (U, Th and K) can strongly be correlated to the concentration of clay in soils. These radionuclides have been present in rocks and sediments since the formation of the soils. Klooster et. al. (2011) showed that the concentration of Th, derived from gamma-ray spectroscopy, is an excellent proxy for soil clay content. Moreover, agricultural land in the southwestern part of the Netherlands was mapped with an MS-1000 gamma-ray spectrometer, mounted on the underside of UAV, by the Medusa Institution. This platform analysed the clay content of soils with higher spatial resolution than would be achievable with discrete soil sampling. Egmond et. al. (2018) investigated soil texture in the east of Flevoland polder in the Netherlands by using a UAV system, ground-based system and traditional ground sampling data. K concentrations in ground-based measurements were slightly higher than UAV data. The average values of U and Th from both data are the same. Calculations of Cs concentrations derived from UAV, were considerably higher than ground-based data, require more accurate elevation calibration rather than used in the article. This study shows that soil texture between 0 and 30 m can be correlated by using linear regression analysis because of the small size of the experimental site. However, more research is needed to obtain more accurate results. The paper further details the expense of UAV operation in agriculture – highlighting that UAV surveying represents a cheaper method than ground-based data collection. As another example, the topography of the land next to Pripyat River next to Chernobyl presents a potential flooding problem. It has become a critical issue after the Chernobyl disaster because of the existence of ^{90}Sr and ^{137}Cs isotopes with this aim, soils and floodplain scenario were prepared in Ukraine (Konoplev, 1996, 1999). Comparison of the $^{137}Cs/^{90}Sr$ ratio in samples and the radiocesium data obtained by γ-survey with UAVs was determined as the most effective way to follow radiation footprints. Briechle et al. (2018) studied uncharacterised biomass for radioactive deposits of the Chernobyl Excursion Zone using a UAV gamma spectroscopy, Lidar and machine learning. It was observed that reliable and accurate results were found by using artificial intelligence methods for 3D vegetation mapping. However, the use of the gamma spectrometry in the classification process for determining radioisotopes proved to be problematic due to radiation levels in this area.

Marques et al. (2018) worked at GammaEx Project (Chemical, biological, radiological/nuclear or explosive (CBRN)), a remote sensing investigation using UAVs in maritime environments. This project aimed to develop Remotely Piloted Aircraft Systems (RPAS) that could perform CBRN tasks remotely; minimizing the risks for human life. Furthermore, the desired systems should be able to operate in a maritime environment, specifically examining the exterior of ships or offshore platforms. They needed to operate in often adverse environments (e.g. with strong air turbulence, and potentially explosive atmosphere), therefore reducing the risks of human exposure to hazardous conditions. The GammaEx M5 Drone platform equipped with a RadEye spectroscopic personal radiation detector (SPRD) spectrometer was operated as a radiation mapping system in this project. The authors did not share their results in this paper. Moreover, recent developments and the need to improve mapping options by using various geophysical methods in terms of soil properties, were discussed by Ameglio in 2018. According to the researcher, using the information gathered from combination of CsI gamma spectrometer, thermal cameras, near-infrared (NIR) hyper-spectral camera, portable short-wave infrared (SWIR) camera, use of reflected GNSS and electromagnetic data would be useful to solve agricultural problems for soil productivity.

This topic has been searched with a growing number of articles focussed on UAV system modelling, detectors types, signal processing methods to distinguish radioactive isotopes energies and inversion methods finding radioactive sources on the ground. For instance, Minty et al. (1997), is perhaps the most important article in airborne gamma spectrometry. In this work, explanations of fundamentals, calibrations and data analysing steps are discussed in terms of dead time, energy drift, background removal, source thickness, source diameter, detector response and distance between source and detector. Towler et al. (2012) detailed radiation mapping and localization capabilities of a remote sensing system developed by Virginia Tech for the Fukushima Daichii nuclear power plant case so that this system produced high resolution and effective maps of radiation intensity. In 2015, Lucas and Jozsef gave a detailed literature review about radioactivity and the advantages and disadvantages of radiation detection systems on UAVs. They also compared between optical remote sensing and hyperspectral imagining techniques for the acquisition of LIDAR data model. Newaz et al. (2016) proposed a new method, usage

of Hough transform (Duda and Hart, 1972) and the Variational Bayesian (Bayes et al., 1763) to localize multiple sources. Utilization of this method with an UAV can find the positions of sources rapidly but also this approach must be implemented with multiple UAVs. Connor et al. (2016) reviewed airborne radiation mapping topics and algorithms for current and future aerial systems methods in detail. They concluded that all detector systems and mapping solutions must be chosen considering the project aim. Future systems should look for more accurate 3D models of radiation distribution to improve their results. Zabulonov et al. (2016) developed a rapid methodology for calculating radioactivity of different materials for extremely low signals whose intensity is much less than the background radiation. Barzilov et al. (2016) designed a small-scale UAV for observing neutron\gamma radiation using the maximum likehood estimation (MLE) algorithm. This was tested with several sensors for source localization purposes. Varley et al. (2016) mapped the activity of ^{226}Ra at legacy sites in Scotland using a machine learning method trained on aerial radiometric data. According to their results, the combination of neural networks and Lanthanum Bromide detectors gave more accurate depth and activity values than traditional sampling methods. Fortin et al. (2017) also reviewed aspects of standard data analysing methods, individual detectors within the systems arrays, directional information on the origin of the signal and single photopeaks from Th, U as an analysing step for modern airborne gamma spectrometry. Stibinger (2017) dealt with cooperative use of multiple unmanned helicopters for localization of radioactive sources using Timepix detectors in the Czech Republic. He showed that the identification of the direction of the radioactivity but he ended that still needed to be considered variations in complex topography and the number of sources. Guss et al. (2017) demonstrated UAV systems (Sandstorm, T-28, 3DR Solo, Tarot Octocopter), using a Geiger Mueller tube and NaI(Tl) detectors to test remote contour mapping through simulation. They validated waypoint detection of a nuclear site in America for ^{137}Cs\ ^{192}Ir isotopes and their airborne measurements (performed in cps). They found that accurate source results can be collected from less than 15 metres. Martin et al. (2018) tested a novel ground-based radiation mapping platform using two Kromek SIGMA-50 detector on the western of the FDNPP and they claimed that their system is able to prepare high resolution maps (based on cps values) for radioactive isotopes. Dess et al. (2019)

improved a background correction method when the characteristic photopeaks for ^{137}Cs and ^{60}Co in the spectrum had S\N ratio below approximately 3.0.

The main issues addressed in this literature review were: a) applications of UAVs to a range of different scenarios and b) processing of radiometric data. Firstly, the use of UAVs for radiometric survey is a milestone responding tool for future nuclear accidents and disasters. The technique is able to produce high spatial resolution radiation intensity maps without the need to endanger workers or incur great expense. These maps are capable of influencing energy policies, mitigation and management plans for potential nuclear incidents in the future and also are quite practical for daily monitoring and scanning of cargo ships and vehicles, increasing productivity in agriculture, and the identification of certain ore deposits dependant on their characteristic radiological footprints. Early studies from before the Fukushima incident in 2011 (Kurvinen et al. 2005; Pöllänen et al. 2009) tested the feasibility of different systems in detecting radiation using fixed-wing UAVs of different sizes and in different scenarios. The studies identified that unmanned systems decrease the risk and/or time of the data collection rather than manned methods. After Fukushima accident, there were a sharp rise in the number of UAV-based radiation detection studies (Furutani et al., 2015; MacFarlane et al. 2014; Martin et al. 2015; Sanada and Torii 2015; Towler et al., 2012). These papers highlighted the implications of UAVs by using several detector systems and pointed out mapping solutions. They found that the choice of systems will strongly change based on the research problem, furthermore, they expressed that the high spatial resolution and sensitive radiation maps can be provided by low altitude UAV surveys relative to the higher altitude methods previously deployed. The second issue in this section is that the well-known standard processing of airborne gamma-ray spectrometry (AGRS) data is based on a simple model of geological or geometrical parameters of the gamma-ray radiation propagation (Grasty and Minty, 1995; IAEA, 1991; IAEA, 2003; Killeen et al., 2015) where flight height changes only slightly along the survey line within the footprint area. This principle of standardising the processing simplifies the research problem and avoids lots of formulations of the inverse problem. Unfortunately, this approach can result in errors of simple and certain AGRS data processing tasks (Schmarz et al., 1992). After 1997s, there was a growing interest in data processing techniques for localization

problems of radioisotopes on the ground (Druker, 2017). This is the most significant research that proposes a different approach related to flight lines and geological parameters where the solutions of inverse problems are used for data processing.

1.2. Hazardous Isotopes

There are many radioactive isotopes, which are potentially hazardous for human and environment. Some radioactive elements have occurred naturally such as uranium (^{238}U), thorium (^{234}Th), potassium (^{40}K) and radon (^{86}Rn) which have a high enough intensity to be measured by airborne surveys (Minty, 1997). Other elements can be produced artificially for special purposes or as waste product of nuclear power reactor. The most persistent is cesium-137 (^{137}Cs). This isotope is created as secondary product of uranium-235 (^{235}U) nuclear fission, which is the main source of power for most of the nuclear power plants and nuclear weapons.

1.2.1. Uranium

Uranium is the most abundant of the naturally occurring actinides (Ac, Th, Pa, U) with values ranging from 1.2 ppm (1.2 mg\g-120mg\g) in sedimentary rocks to 120 ppm in phosphate rocks (Hanson and Langmuir, 1977). The lower members of actinide series are derived from the decay of three, long lived parent nuclides ^{238}U, ^{234}U and ^{232}Th. Due to the radioactivity of Uranium, the element is commonly found in association with its decay products. The Uranium decay series starts with U-238 in an unstable state and ends with Lead 206 in a stable state. Figure 4 illustrates the possible decay routes that can be followed by the decay of uranium 238 to reach a stable state. The route consists of 14 steps and is indicated in Table 1 along with the type of radioactive decay while the remaining eight decay by emitting alpha particle (Koch, 2000). The Uranium decay series also occurs over a wide span of periods stretching from Uranium 238 decaying over 4.5 billion years to reach thorium 234, while 214 Po will decay in a time span of 164 μs to form 210 Pb (Koch, 2000).

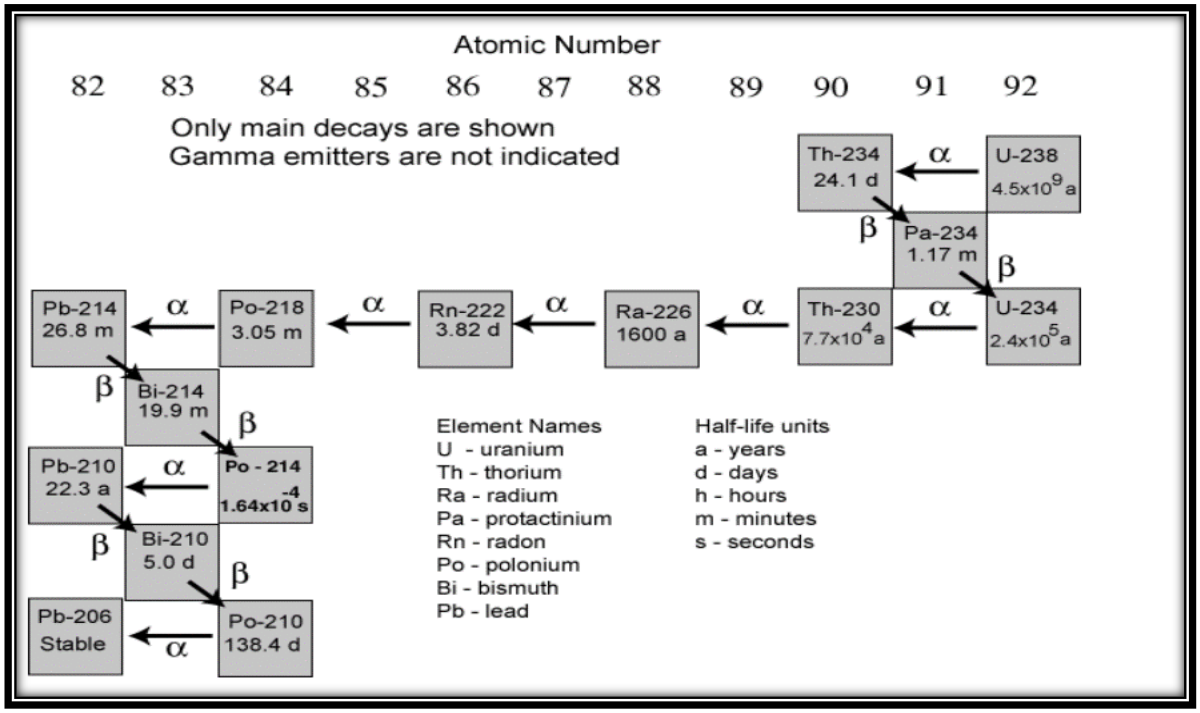

Figure 4. Uranium decay series from **[3]**

Table 1. ^{238}U decay series with half-lives and radiation type from [3]

Isotope	Radiation	Half life
^{238}U	α	4.507×10^{9} a
^{234}Th	β	24.1 d
^{234}Pa	β	1.18 m
^{234}U	α	2.48×10^{5} a
^{230}Th	α	7.52×10^{4} a
^{226}Ra	α	1600 a
^{222}Rn	α	3.825 d
^{218}Po	α	3.05 m
^{214}Pb	β	26.8 m
^{214}Bi	β	19.7 m
^{214}Po	α	1.64×10^{-4} s
^{210}Pb	β	22.3 a
^{210}Bi	β	5.02 d
^{210}Po	α	138.4 d
^{216}Pb	Stable	

Uranium minerals can be classified as primary and secondary in terms of their components (Figure 5). The most abundant Uranium phase is Uraninite which is always at least partially oxidized in the nature, with formula UO_{2+x} with x in the range of 0.0 to 2.5. The structure contains many defects because of oxidation and cationic substitution, as well as, radiation damage. It is commonly black with an iron-block metallic lustre, although various dark shades of brown and green have also been reported for more weathered material. Moreover, it is a common mineral in pegmatites, granites and mainly includes Th, REE, Ca and other elements.

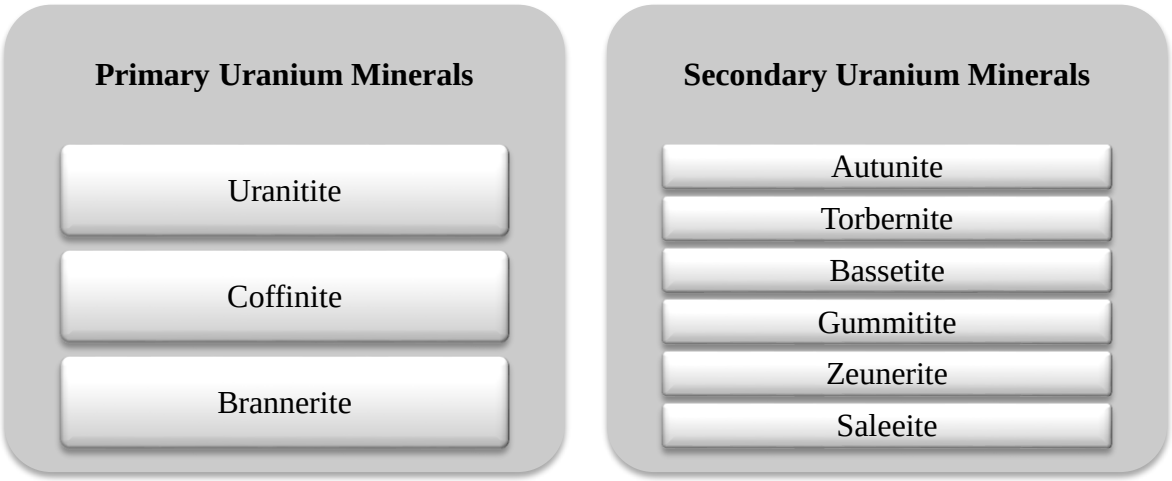

Figure 5. Uranium minerals modified from [4]

After Uraninite, coffinite is the secondary economic ore mineral for U. It is isostructural with zircon. Coffinite is the major U-bearing mineral in many sandstones hosted U deposits and commonly occurs intimately intermixed with organic material such as lignite. Brannerite is typically metamict and requires annealing to produce an X-ray powder diffraction (XRD) pattern and it is a common accessory mineral in numerous Uraninite and Coffinite U deposits. The IAEA reports uranium deposits within 15 main categories of deposit types, according to their geological properties and mineralization structure and economic value. According the literature, the most productive uranium ore mineralization is found in igneous rocks (granites) and sedimentary formations (shales, sandstones, lignite).

1.2.1.1 Cesium- 137

Cesium-137 or radiocesium is a radioactive isotope of cesium formed as one of the more common fission products by the nuclear fission of ^{235}Uranium and other fissionable isotopes in nuclear reactors and nuclear weapons. It is the most problematic one because it easily moves, spreads and is soluble. Cesium-137 and Caesium-134` half-lives are 30.17 and 2.065 years, respectively (Figure 6a). The main photon peaks of Cs-137 and Cs-134 are 662 and 604 keV, respectively (Figure 6b). About 94.6 percent decays by beta emission to a metastable nuclear isomer of ^{137m}Ba. Ba-137m has a half-life of about 153 seconds.

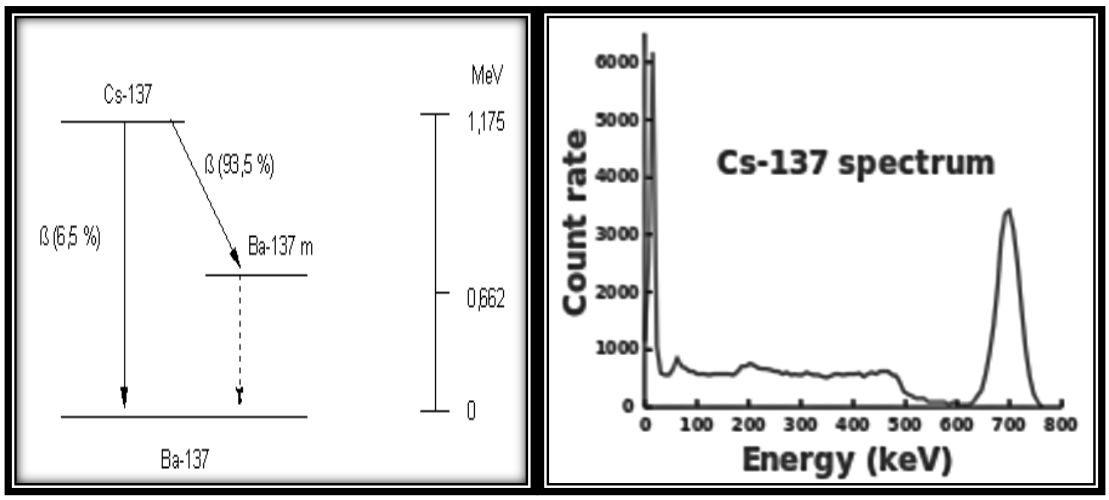

Figure 6. a) Cs-137 Decay Scheme and b) Gamma Energy Spectrum from [5]

After the literature review, this project presents the research question and the rationale of choice of the problem that this project hopes to solve. This is followed by the fundamentals of radioactivity and methods used in the research. After that, the background of survey sites and applications on them were explained. The results section covered all analysing processes for the research problem. Finally, the conclusion chapter consists of the key findings and future focus of this work.

2. DEFINITION OF RESEARCH PROBLEM

Radiometric surveying methods are used for uranium exploration in many countries (IAEA, 1979). The varying distribution of potassium, uranium and thorium in rocks and soils can also help to define localization of mineral deposits, including gold, tin, tungsten and rare earth elements (REE). The resulting radiation intensity maps from regional and local-area surveys can provide information on the location of 'areas of interest' so that closer examination and sampling can be undertaken (Connor, 2016). In some instances (Martin et al. 2016, Connor et al., 2018), when a well calibrated detection system is used, the arising data may be processed to produce dose maps that can highlight areas that would prove concerning for human health. Additionally, when gamma spectrometers are used for surveying, the arising spectral data can be utilised to discern natural background sources from those which are anthropogenically derived. This would be particularly beneficial after a nuclear incident, where radioactive fallout maps are required for planning the emergency response, including evacuations, exclusion zones, access restrictions, crop production policies and aquifer management (Martin et al., 2016; Ameglio, 2018; Beckett, 2003). In the above applications: mineral surveying, nuclear site monitoring and emergency response radiometric data requires:

i. Fast collection
ii. Prompt processing and plotting
iii. Easy distribution/sharing
iv. Optimal spatial resolution
v. Optimal spectral resolution / counts rates

There are physical mechanisms that effect the intensity of the measurements in the air, such as, the Inverse Square Law (ISL) and atmospheric attenuations (Pöllänen et al. (2009) and Sanada and Torii (2015)). These physical mechanisms have a significant impact on the spatial resolution and sensitivity of airborne radiometric surveys. As shown in Figure 7, the spatial resolution is higher and the recorded signal intensity is greater at lower UAV altitudes, although survey coverage may be incomplete. Conversely, at higher altitudes, although the spatial resolution is lower and the recorded signals are

weaker the survey coverage is more comprehensive. Therefore, selecting the correct surveys altitudes is of paramount importance.

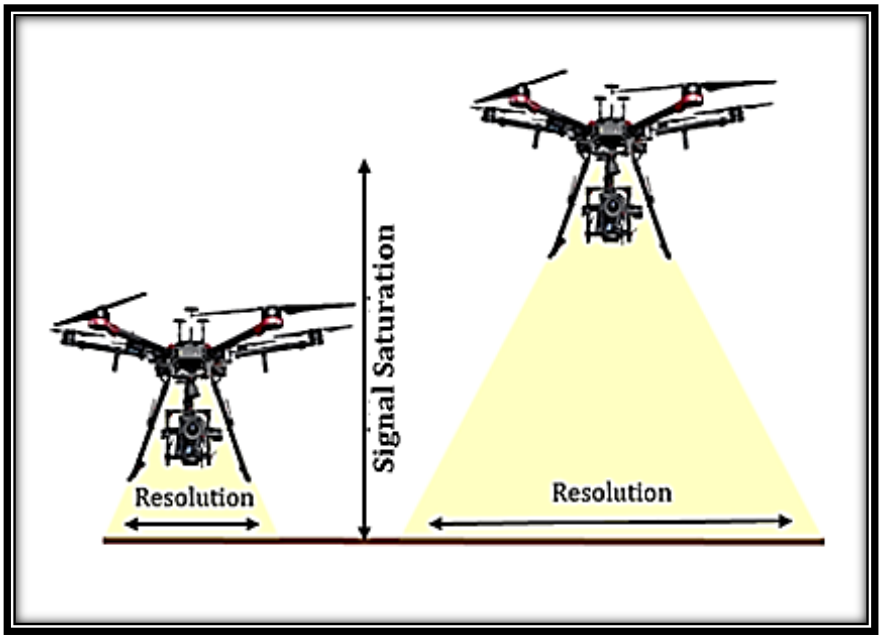

Figure 7. Diagram of research project aim

In airborne surveys, all the data points including; geometrical parameters (topography), global positioning systems (GPS), physical measurements (pressure, temperature, humidity) from UAVs system are assumed to be known. The only unknown parameter is the radiation intensity on the ground. The inverse square law (ISL) merely depends upon distance whereas atmospheric attenuation is proportional to air density and the gamma photon energy. Air density is a function of temperature, humidity, and air pressure. Therefore, all these errors in all of these factors are known to create uncertainty or error in data recorded during a survey. Measurement uncertainties in the distance (i.e. the distance between a source and the detector) is most likely the greatest source of error in any aerial radiometric survey.

With this in mind the main purpose of this project was to enhance spatial resolution of maps of radioactive fallout, derived from UAVs, especially ^{137}Cs caused by nuclear power plants. This included developing a new data processing method for processing airborne gamma-ray spectrometry (AGRS) results which improved upon the current Inverse

Distance Weighting (IDW) methodology currently used. This new processing approach was further extended to develop an inversion method to produce hyperspectral gamma images (HSGI)) of areas within of the Chernobyl nuclear site exclusion zone.

Radiation intensity maps produced via IDW or linear inversion from the total counts data is compared to maps produced using HSGI data processing. The second aim is to search the optimal survey methodologies to be used when deploying a new UAV platform.

3. OBJECTIVES OF RESEARCH PROBLEM

The main purpose of this work was to investigate the research opportunities discussed in section 2. The first step was to analyse several count-rate plots for specific radionuclides from surveys at various UAV flight configurations and to suggest a better surveying methodology. The second step was to improve horizontal spatial resolution and attain a high-quality radiometric map by using a newly developed inversion method to produce hyperspectral gamma images.

4. PRELIMINARIES

4.1. Fundamentals of Radioactivity

Atoms are the smallest particles of mass with specific chemical properties. An atom consists of a nucleus surrounded by electrons. Positively charged protons and uncharged neutrons surrounded the nucleus. Radioactive nuclei have surplus energy, are not stable and want to transform into their stable nuclei to different isotopes over years. They emit alpha, beta particles and gamma rays during their transformation process which have important properties as below

- To affect the photographic film base such as optical rays or X-rays
- To ionize gases and make them conductive
- To occur scintillation on minerals/chemical components

This transformation, termed radioactive decay, results in release of energy or radiation emission in the form of particles arrays. The Radioactivity decay is a stochastic process and the time/direction of the emission cannot be predicted. According to radioactivity

decay law, it can be explained as a reduction in the number of atoms for a radionuclide with time (Equation 1) (D'Auria , 2018).

$$N_t = N_0 e^{-\lambda t} \quad (1)$$

N_t = the number of atoms present after time t (seconds (s)); N_0 = the number of atoms present at time t=0; $\lambda =$ the decay constant of a radionuclide (s^{-1}). However, certain properties can be used to describe a collection of these atoms such as half-life and activity. Half-life, symbol $t_{1/2}$, describes a time interval during which one half of atoms undergo the decay process. It means that every atom has a 50% probability of decaying during this time. Half-life of atoms ($t_{1/2}$) changes between a few nanoseconds to hundreds of years which can be calculated from Equation 2 (D'Auria, 2018).

$$t_{1/2} = \frac{0.693}{\lambda} \quad (2)$$

The product of λN gives the activity (Bq) of radionuclide. The other physical conditions do not affect the radioactive decay.

4.2. Radioactive Decay and Radiation

Radioactive materials emit in different ways e.q. X-rays.

4.2.1. Alpha Decay and Radiation

The process of alpha decay consists of a nucleus releasing an alpha particle, comprising two protons and two neutrons, which is identical to a helium nucleus. It is a relatively massive particle whilst also being weakly penetrating compared to other types of radiation. An alpha particle can be stopped with paper or skin. It is dangerous if it enters the body by inhalation or ingestion because large exposures can result in damage to nearby tissues, such as the lining of lung or stomach cancers. Its formula can be seen below (D'Auria, 2018).

$$^{A}X \rightarrow {}^{A-4}Y + \alpha \text{ (Alpha emission)}, \; Z_Y = Z_x - 2 \qquad (3)$$

4.2.2. Beta Decay and Radiation

Beta$^-$ decay is realized by the emission of a beta particle identical to a negatively charged electron. Beta$^+$ decay, which is not rare, is accompanied by the emission of a positively charged positron. Beta radiation is an electron emitted by an unstable nucleus. The initial velocity of beta particles is close to light speed and alpha particles are bigger than them and can ionize atoms. It can be observed by sheets of plastic, glass or metal (D'Auria, 2018).

It is not generally affective beyond the top layer of skin, but high volumes of beta emitters can cause skin burns.

$$^{A}X \rightarrow {}^{A}Y + \beta \text{ (Beta emission)}, \; Z_Y = Z_x + 1 \qquad (4)$$

4.2.3. Gamma Ray and Radiation

Gamma rays consist of photons in the highest observed range of photon energy. They have high energy; short wavelength and they are located at the end on the energy spectra. When gamma radiation passes through matter due to interactions with electrons, ionization in atoms occurs. Gamma rays penetrate high density materials, for example, steel or lead (Figure 8). High doses of it can transport into internal organs without inhalation or ingestion (D'Auria, 2018).

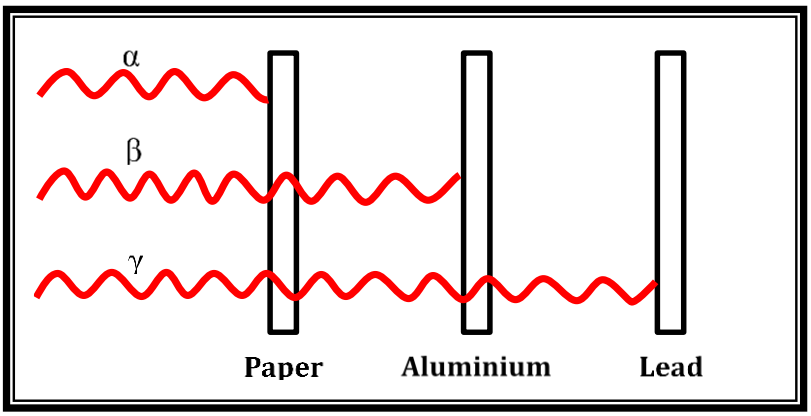

Figure 8. Gamma-ray emissions

4.2.3.1 Interaction of Gamma Radiation with Matter

Instrumental detection of any particle or radiation depends on the production of charged secondary particles which can be collected together to produce an electrical signal. Alpha and beta particles generate a signal within a detector by ionization and excitation of the detector material. Gamma photons are uncharged and do not have ability to do this. Gamma rays interact with atoms of matter by three ways. The first one, photoelectric absorption, arises by interaction of the gamma ray photon with one of the bound electrons in an atom.

The electron is ejected from its shell with a kinetic energy, E_e,

$$E_e = E_\gamma - E_b \qquad (5)$$

where E_γ is the gamma ray energy and E_b is the energy binding the electron in its shell. The atom is left in an excited state with an excess energy of E_b (D'Auria, 2018).

Compton scattering (Figure 9) is a direct interaction of the gamma ray with an electron, transferring part of the gamma ray energy. It can be explained by below formula and μ_0 and Θ are defined the electron mass and the scattering angle, respectively (D'Auria, 2018).

$$E_e = E_\gamma - E_\gamma' \quad E_e = E_\gamma \left\{ 1 - \frac{1}{1 + E_\gamma \left(1 - \frac{\cos\theta}{\mu_0 c^2} \right)} \right\} \qquad (6)$$

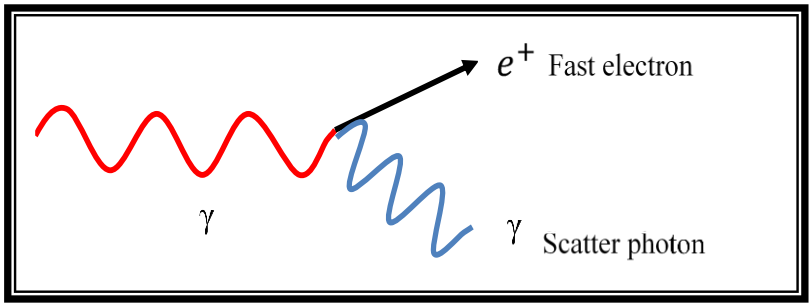

Figure 9. Compton scattering

The third one is pair production (Figure 10) which is only seen within the gamma ray spectrum when the energy level is higher than 1022 keV. It involves the transfer of energy from a gamma ray to an electron/positron near to the atomic mass, after that it disappears (D'Auria, 2018).

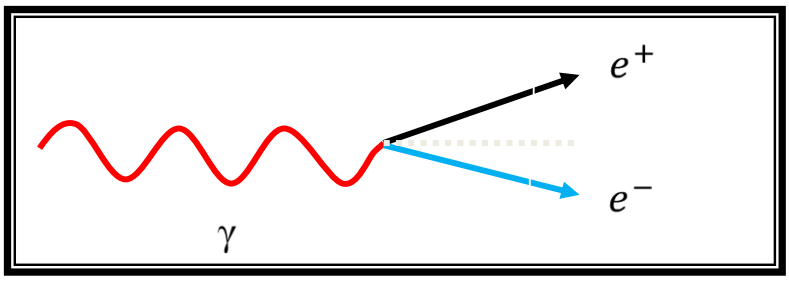

Figure 10. Pair production

There are three possible explanations for pair production

- Positron decay of a radionuclide
- High energy gamma rays from the source
- High energy cosmic rays

4.2.3.2. Types of Gamma Ray Detectors

Gamma ray detectors are the best system of choice for environmental radiation detection applications using UAVs (Connor, 2018). Light yield, energy resolution and decay time are important criteria for detection of gamma-rays. Light yield is a measure of the efficiency of scintillators to convert the incident radiation to the light output and is presented in units of photons/MeV. The higher the light yield the better the efficiency of the scintillator. Energy resolution of the detector is represented by full width at the half maximum (FWHM) of a photopeak. The smaller energy resolution or FWHM is the higher the quality of detection results. There are several commercial off-the shelf detectors with benefits and handicaps. These can be divided into five categories.

4.2.3.2.1. Plastic Scintillators

Plastic scintillators are generally used and cost effective for the detection of radioactive material at ports-of-entry. Furthermore, these detectors can be designed very large and in combination, can scan large areas such as highways and railways. They have low resolution and it is ineffective for identification of a radiation source for UAVs (Cerrito, 2017).

4.2.3.2.2. Sodium Iodide (NaI) Scintillators

NaI scintillators are the typical spectrometers that have been used for a long time. As such, the technology is well-developed and they operate at room temperature, unlike the other common spectroscopic detector high-purity germanium. Crystals can be made much larger than 2”x4”x18” but are much more expensive than plastic detectors. These crystals are commonly suitable for hand-held surveys. The utility of using NaI detectors is to find the location and identification of the source on the ground (Cerrito, 2017).

4.2.3.2.3. High-Purity Germanium (HPGe) Detectors

HPGe detectors are used in the laboratory for the detection and identification of radioisotopes. High quality data make them ideal for gamma spectroscopy. On the other hand, they require to be cryogenically cooled, and they are significantly more expensive than a NaI detector because of dimensions. The cooling requirement also results in a much heavier instrument. Laboratory systems are generally cooled using liquid nitrogen while field-deployable systems are typically mechanically cooled (Cerrito, 2017).

4.2.3.2.4. Lanthanum Bromide (LaBr3) Detectors

LaBr detectors have similar features as NaI detectors. They have slightly better energy resolution than NaI detectors at room temperature. Large enough crystals are essential to make $LaBr_3$ a viable long-range detector (Cerrito, 2017).

4.2.3.2.5. Cadmium Zinc Telluride (CZT) or Cadmium Telluride (CdTe) Detectors

CZT and CdTe detectors have significant energy resolution at room temperature. However, their crystals are much smaller than the other types of scintillators, so they measure low-resolution total counts and they are useful for UAV applications (Cerrito, 2017).

5. CURRENT METHODS

5.1. Current Radiometric Methods & Data Acquisition

The “radiometric” or “gamma ray spectrometric” method is a geophysical process to determine distribution of gamma radiation caused by K, U and Th in rocks and soils (Haldar, 2013). Gamma rays can be measured using two methods. Firstly, the total counts measurement which monitors gross level of the gamma radiation field detects the presence of anomalous sources; and secondly, intensity and energy of radiation measured using spectrometers which help to distinguish the source of the radiation related to energy levels (IAEA, 1995). These methods have been used for directly radioactive mining operations, geological mapping, flow studies, environmental mapping and oil explorations.

Radiometric measurements can be obtained using as by ground and airborne surveys. Airborne survey is an essential component of geological mapping and exploration programs as it provides a continuous coverage of the structure and composition of the subsurface over large areas in a relatively short time. Gamma ray measurements are based on total count rates per second of natural primordial radionuclides, are counted by using handheld spectrometers (GS) and airborne spectrometers (AS) which are two kinds of tools: traditional airborne spectrometer (TAS) and UAV. The system examples of GS, TAS and UAV are shown in Figure 11.

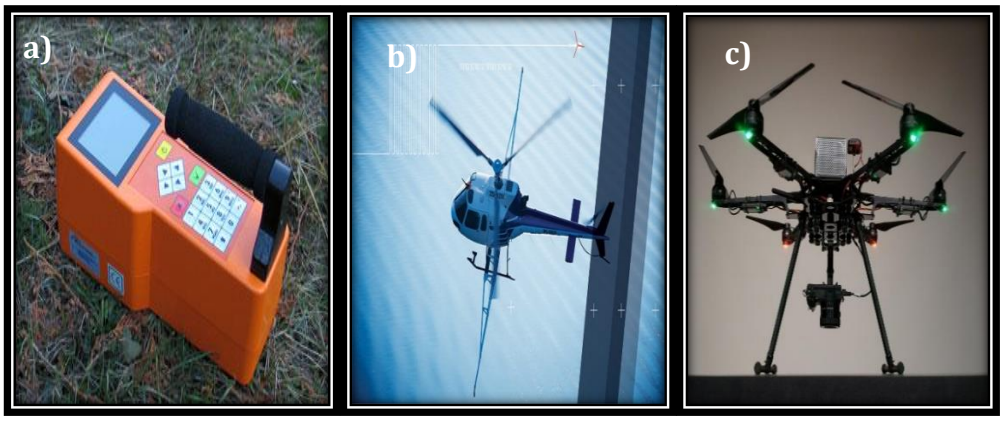

Figure 11. Radioactivity measurements tools a) Handheld (GS) b) TAS c) UAV from [6, 7, 8]

A UAV, commonly known as a drone, is an aircraft without a human pilot on board. This technology can survey large areas in detail, quickly saving hours and can be mapping potential radioactive regions across the world. Lots of developments in UAVs have been done in several countries which can be found in section 1.1. A significant example was revealed by D. Beamish in 2014. He noted that challenges for traditional airborne systems (TAS) occur in the production of high-resolution data from high altitudes (between 50 and 250 m) in the UK. He explained that there was a need for UAVs and high spatial resolution, especially for risky areas.

A receiver (detector), a transmitter for data transfer, a method to locate a source and an algorithm for source identification are required for a UAV-mounted radiation system Any detector must also be suitable for the payload weight capacity. In this study the detector was a scintillating crystal which converts gamma rays to visible photons and then transfers the data to a grand station. Data collection in radiometric survey is contributed to the comparison of the AS and the GS results that each AS point should be obtained across the footprint scale of GS. This data acquisition has a significant impact on the choice of AS and GS points (Figure 12).

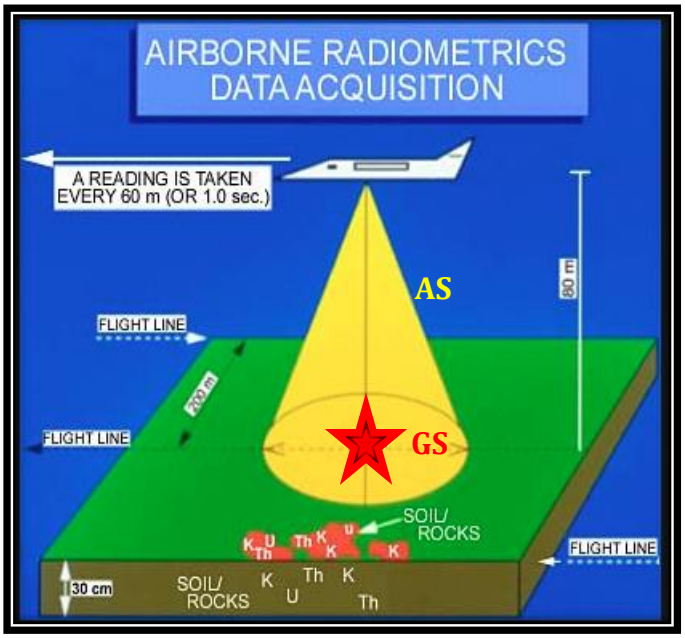

Figure 12. Diagrammatic representation of gamma ray measurements modified from [9]

Airborne geophysical surveys are planned on a regular grid along parallel lines (Figure 13) and the intervals of flight lines depend on the survey aims. The flight lines for geological, environmental mapping are usually between 50 m and 400 m. The regional geochemical applications may be 1 km or bigger. The small-scale surveys are generally done between 1 m and 50 m.

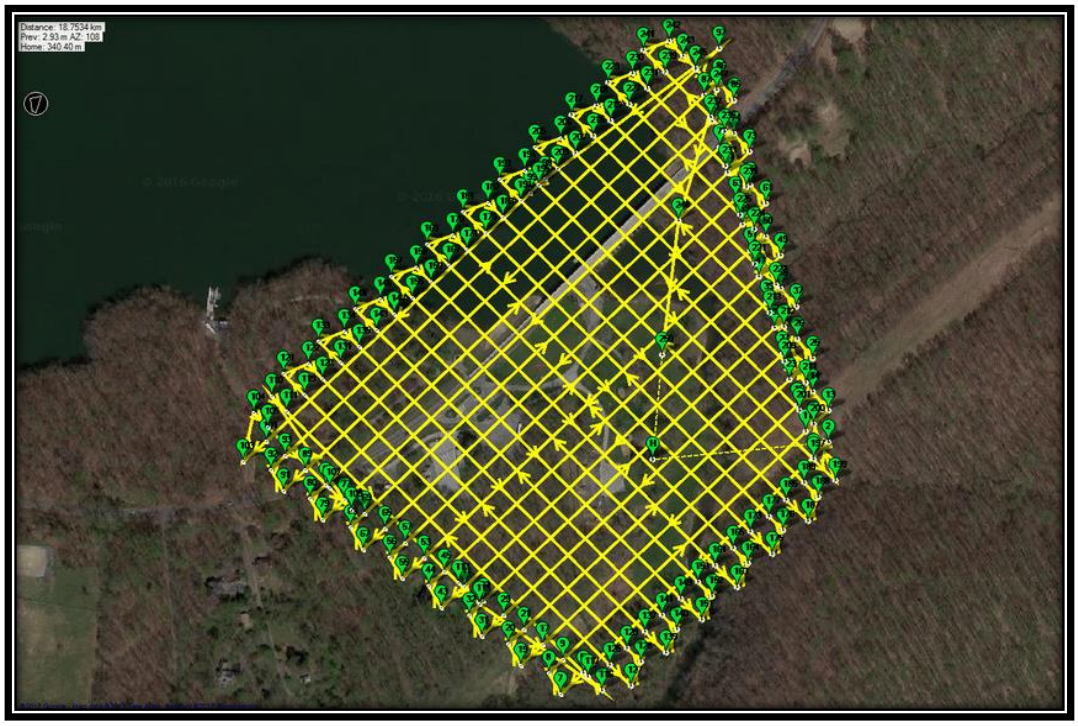

Figure 13. Diagrammatic representation of airborne geophysical survey from [10]

On the other hand, airborne data can be affected by meteorological conditions, the topography of the survey site, cosmic rays, and the height of detector above surface and the speed of the aircraft. Any material that is situated in between a radioactive source and a detector could also cause reduction in measured radiation. During aerial surveys, the increase of height is a major effect on the amount of gamma rays due to the attenuation of atmosphere with suspended elements and the inverse square law (ISL), and this needs to account for it (Schmarz et al. 1995, Sanderson et al., 1995; MacFarlane et al. 2014) in Figure 14. Specifically, ISL means that the intensity is proportional to the inverse of the square of the distance from the source.

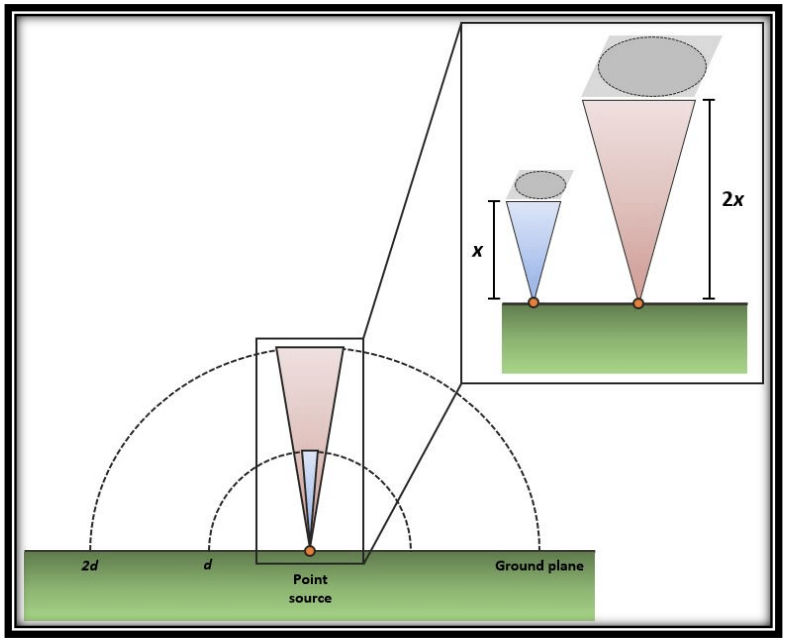

Figure 14. Inverse Square Law from [11]

Moreover, overburden also influences the attenuation of gamma rays; dense vegetation can decrease gamma rays by 35% whilst snow cover of 10 cm will have the same effect as 10 meters of air. Changes on temperature will also affect gamma rays. Lower temperatures increase the density of air, causing higher numbers of interactions, while higher temperatures will reduce air density, causing less interactions. Soil moisture can cause major alterations in gamma ray surveying. When soil moisture increases by 10% the number of gamma rays leaving the soil will decrease by 10%. Therefore, it is recommended that surveys should be done at least 3 hours after it has rained so that abnormal surface activity can decay (Erdi-Krausz & Nicolet, 2003).

Another important point of radioactive material detection is the changes in background radiation. Gamma radiation can change based on the formations as well as difference in the signal from man-made structures. For instance, soils are less radioactive than many rock formations in naturally occurring radioactive material (NORM) so a positive signal can be measured as a result of a rock outcropping surrounded by soil. Moreover, high radioactive signal can be relatively defined because of certain man-made structures. Stone or concrete structures may have significantly more NORM than steel or wooden structures.

5.2. Current Aerial Radiometric Survey Mapping

As previously stated in Section 5.1, D. Connor explained that "radiation mapping is the recording of the radiation intensity level at several points throughout a survey area and displaying the data based on coordinates and an intensity measurement (gross count, activity, or dose rate) in a graphical form" (Connor et al, 2016, pp. 5965). General framework of a radiation mapping survey can be separated into three parts as below.

1) Defining calibration method
2) Data collection
3) Presentation

The most well-known calibration method is a 'hover survey' (Furutani et al. 2015; Sanada and Torii, 2015; Schwarz et al. 1995). A hover survey is the measurement of intensity at several different altitudes via a specific datum on the earth's surface by UAV or big helicopters. The final intensity maps are commonly normalized at one meter above ground level (AGL) (Furutani et al., 2015; Martin et al. 2015; Sanada and Torii 2015; Schwarz et al. 1995 by using calibration curve. This normalization (altitude correction) must be done carefully because of rapid changes in surface topography (which itself is often derived from digital elevation models (DEM) at a metre to millimetre scale (Furutani et al., 2015; Sanada and Torii 2015; Martin, 2015.). Counts per second (cps), the respond of the gamma spectrometer, is used in these mapping applications.

After these calibrations and calculated parameters, there are several ways to determine radioactive source localization, including using statistical algorithms such as non-linear least squares optimization, recursive bayesian estimation (RBE), multi linear estimation (MLE) (Howse, Ticknor, and Muske, 2001; Brennan, Mielke, and Torney, 2005; Knoll, 2010; Muske and Howse, 2001; Towler, Krawiec, and Kochersberger, 2012; Gunatilaka, Ristic, and Gailis, 2007; Morelande, Ristic, and Gunatilaka, 2007).

Moreover, the contour mapping localization algorithm provided by Towler et al. for areas where the prior information from the survey area is not available, is the most common technique, to show hotspots and regions of low intensity by using Inverse Distance Weighted (IDW) deterministic algorithm suggested by IAEA in 2003. Moreover, these

radiation intensity maps related to concentration and spatial distribution of radioelements could be seen in Figure 15.

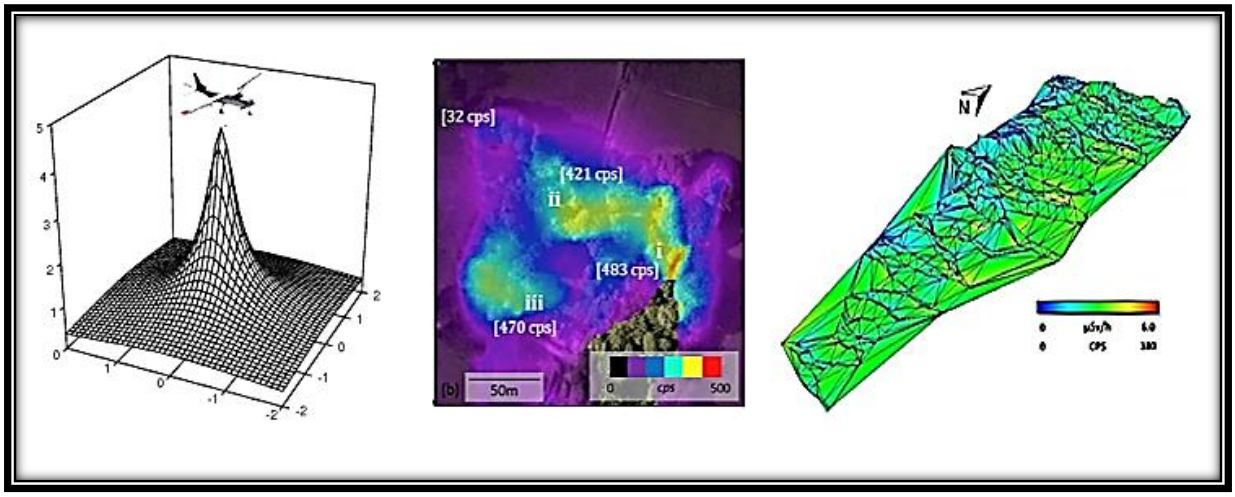

Figure 15. Maps of radiation intensity a) 1D b) 2D c) 3D from [12, 13, 14]

Inverse Distance Weighting (IDW) is a common geostatistical interpolation technique for airborne data (IAEA, 2003). It predicts a value for an unmeasured point, and it uses the specified measured values around the estimation point (Gotway et al., 1996). The actual values nearest to the prediction location have more effect on the estimated value than those farther away. Meanwhile, this effect is a function of distance, hence the name inverse distance weighted.

Table 2. Advantages and Disadvantages of IDW Methodology

Advantages of IDW	Continuous values on contoured levels
	Easily understandable
	Not produce estimated values outside values
	Deriving results from unsampled locations
Disadvantages of IDW	No assessment of prediction errors
	Need huge data sets for more accurate estimation

According to the advantages of the IDW algorithm in Table 2, we assumed that an IDW radioactive intensity raster would have been more accurate than other basic interpolation techniques due to the research problem. Therefore, radiometric data sets derived from Chernobyl survey sites were interpolated by using inverse distance weighting (IDW) method to define location of radioactive sources quickly. On the other hand, Connor (2016) explained that "the interpolated map by using this technique present a little concern over its ability to upscale to larger areas, making it more suitable for larger-scale operations such as rapidly identifying areas of risk following a large radionuclide release" (Connor, 2016). However, when there is a hotspot near to low intensity sources, this technique appears to make the lower radioactive sources invisible, whilst ghost sources can appear and are not enough for specific determination of radioactive sources locations that is why the research question is selected and pruposes to demonstrate the improvement of radiation intensity map derived from HSGI technique via IDW method.

5.3. Image Reconstruction of Aerial Radiometric Survey Mapping

Recorded total count is a summation of all emitters of the ground, moderated by the height of the UAVs (ISL) and the attenuation of gamma photons in the air previously described in section 5.1. Any recording can be explained as a simple summation which is a linear equation, is consistent and has a solution. Having different recordings gives a set of linear equations; i.e., a linear inversion problem that can be solved via iterative inversion methods in order to model the actual underlying radiation field.

In this section current inversion methods, a description of a linear problem and how to solve it by using algebraic reconstruction technique (ART), is used for the research problem. A numeric demonstration of its implementation is demonstrated (Figure 17, 18). Survey sites demonstrations will be shown later in the results section (from Figure 41 to Figure 54).

5.3.1. Current Inversion Methods

The theoretical and practical issues of geophysical information processing or geophysical inversion have been increasingly addressed in the scientific literature (Zhdanov, 2015). Geophysical linear inversion is the term for a set of mathematical methods that can be used to produce geophysical maps based on physical properties (density, magnetic susceptibility, gamma-ray levels etc) from measured geophysical data (such as total counts derived). These approaches use optimization methods based upon the localized geophysical readings and removes topography effects (ISL problem indicated in section 2 and 5.1). Furthermore, it also helps compensate for the energy attenuation in the air (section 2 and 5) in the recorded data. The satisfaction of system is the amount of relative error between measured and predicted model in the system (Figure 16).

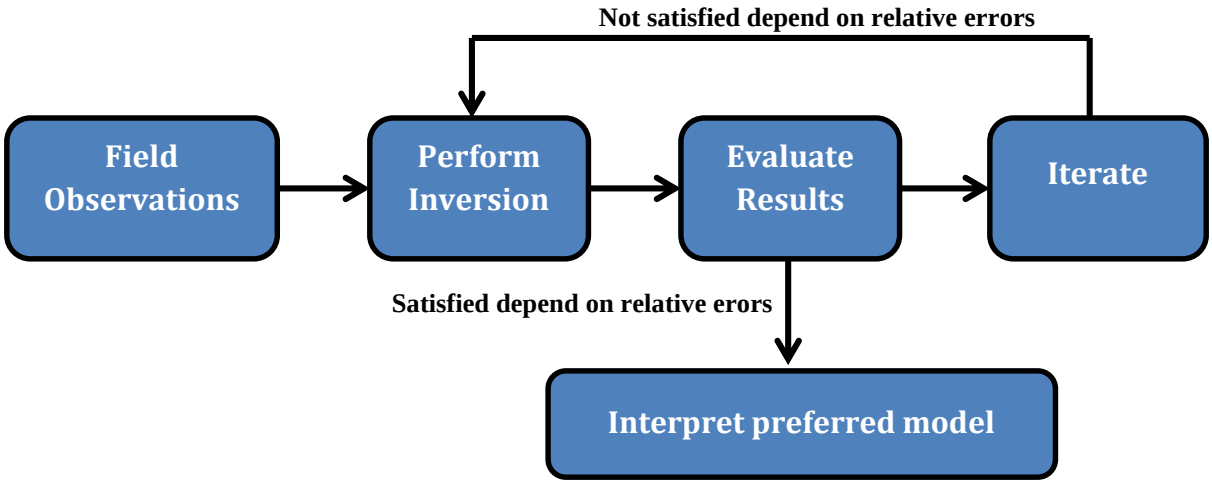

Figure 16. Methodology of Inversion

To conduct radiation mapping, the raw map (field observation) that is produced outlines the distribution of radioactivity within the survey area as detected by the detector in space (and not necessarily a true reflection of the position of the source within the ground). For extremely low altitude surveys, this may be enough to indicate the location of the sources involved in producing the radioactivity. However, this will not always be the case. In the presence of differing activity sources, stronger sources may mask weaker

sources that may be nearby to them. Additionally, as the survey altitude increases, the certainty with which a source can be localised decreases (Martin et al., 2016).

To overcome some of these error sources, the current work has investigated the use of an inversion algorithm (randomized Kaczmarz) by using HSGI to process the raw radiometric data and improve the on-the-ground spatial resolution of the arising radiation map will be explained later.

5.3.2 A General Linear Problem

The general linear problem is shown as below.

$$Ax = b, A \in \mathbb{R}^{m*m} \quad (7)$$

x, b $\in \mathbb{R}^m$ are column vectors. The spatial dependent response functions are described by matrix "A" (i.e., calculations of ISL and energy attenuation depend on each drone and ground positions). Unknown parameters are described by "x" (i.e., the true radiation distribution). "b" holds the Q corresponding, recorded signals such that,

$$A=\begin{bmatrix} a_{11} & \dots & a_m \\ . & . & . \\ a_{Qm} & \dots & a_{Qm} \end{bmatrix}, x=\begin{bmatrix} x_1 \\ . \\ x_m \end{bmatrix}, b=\begin{bmatrix} b_1 \\ . \\ b_m \end{bmatrix} \quad (8)$$

Linear problems are usually solved by matrix inversion, least squares regression and genetic algorithms in the literature. For instance matrix inversion method of D. Smith (2015) explained that "one could force matrix A to be made square by simply selecting M of the possible Q identities and discarding m − Q of them. This is an undesirable approach, however, as one should not discard information if avoidable" (Smith, 2015, pp. 53). However, algebraic reconstruction techniques (ART), suitable for the solution of real problems on the earth such as the research problem mentioned in section 2 and 5.1, helps to solve extremely large matrixes and linear systems such as radiometric data sets mentioned in 4.3 without data information loses.

5.3.3 Algebraic Reconstruction Techniques (ART)

ART is a well-known method suitable for large scale problems (i.e., airborne surveys) having short processing time, low iteration cost and low memory usage. It is easy to implement and analyse, has relatively low complexity and often fits in parallel/distributed architectures. The key advantage of the method is that operations can be done with one row of the matrix.

ART is to solve large linear systems of the form

$$Ax \sim b, \quad A \in \mathbb{R}^{m*m} \tag{9}$$

The ART method was discovered by the Polish mathematician Stefan Kaczmarz in 1937 (Karcmarz, 1937). The first CT scanners used this method for obtaining slice images of a 3D body via X-rays (Hounsfield, 1993). Meanwhile, it is also an important computing tool for signal and image processing recovery in tomography (Sezan and Stark (1987); Cenker et al. (1992)).

Prior knowledge of the problem is an important consideration to write equations. For example, it is known that adding radiation to a scene will only ever increase recorded counts. Therefore, the elements of A must not be negative; more radiation can never result in lower readings. Similarly, gamma count rates can only be positive, it follows that x is positive.

5.3.3.1. Kaczmarz Algorithm

ART methods treat the linear equations one at a time. If the system is consistent, χ_k converges to the minimum-norm solution, provided that the iterations start with the zero vector and each iterative update is given by:

$$x^{k+1} = x^k + \lambda^k \frac{b_i - \langle a_i, x^k \rangle}{\|a_i\|^2} \overline{a_i} \tag{10}$$

"λ" is a relaxation parameter which satisfies between 0.0 and 2.0 values (Dai and and Schön ,2015). "k" is a number of iteration. These determine the extent to which corrections are applied in a single iteration. This iteration includes a purely geometric

interpretation: the algorithm successively projects the current iterate onto the hyperplane defined by the next equation. The iteration procedure is continued until a stop criterion is met such as time, maximum number of iterations, the optimal number of iterations is chosen related to Normalized Cumulative Periodogram etc. Selecting a sufficient number of iterations and a suitable relation parameter affects the rate of convergences for any given datasets (Galantai, 2004). If insufficient iterations are selected, then the inversion will finish quickly but inaccurately. Similarly, if the relaxation parameter is set too high then the system will quickly converge upon a solution, but it will not be stable (Strohmer and Vershynin, 2009). The input and out parameters for this algorithm applied for the current study will be determined in section 6. The estimated model obtained in the last iteration step is accepted as the approximate solution of the inverse problem.

The simple illustration of Karcmarz algorithm process can be seen mathematically in Figure 17. The first step describes true values of the problem and this is what we would ideally want to reconstruct from readings of measurements. The second step is to divide into a grid of two by two pixels and the values outside of the gridded box are measurements. The third and fourth step utilises the Karcmarz algorithm, which needs an initial guess (zero values matrix) for starting the inversion and the example is scanned horizontally and vertically for each row and column of pixels so the first iteration (n=1) uses the horizontal readings only. The absorptivity value of each pixel is corrected by the path length weighted absorption of its row. The second iteration (n=2) defined in the fifth step improves the image by using the vertical readings which means the summation of matrixes and then splitting errors for the next step. This cycle will be repeated due to iteration parameters such as relaxation number and number of iteration (the sixth step). The seventh step presents your estimated values for the real solution of the system.

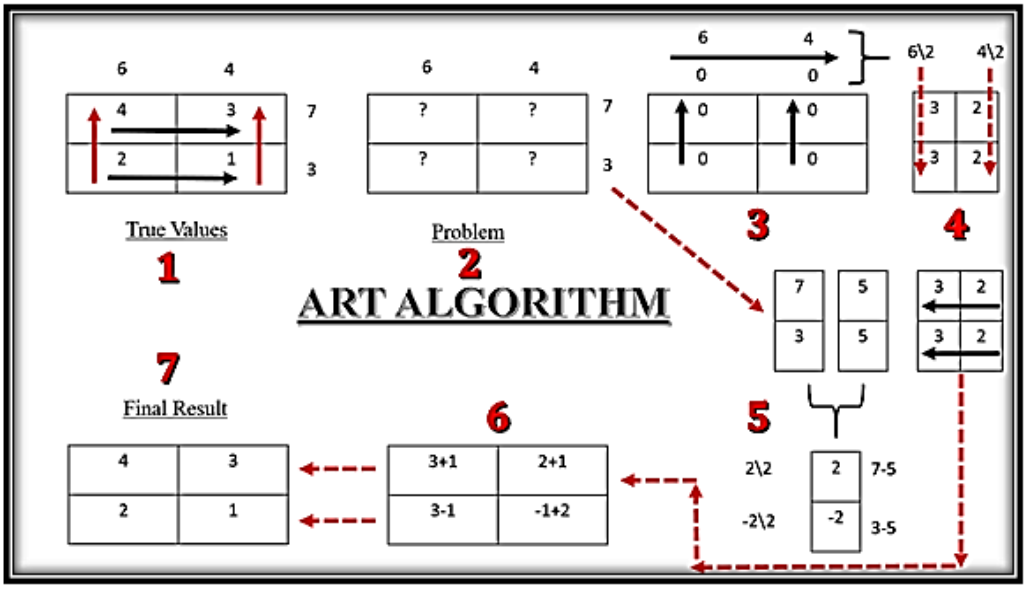

Figure 17. Numeric example of ART algorithm

Figure 18 describes results how the algorithm solves a problem with two linear equations and two unknown parameters considering of stopping criteria (iteration numbers: 10, relaxation parameter: 0.1, 0.2, 0.3, and 0.4). The problem can be written as: A matrix [2 -5; 1 -2], b matrix [1; 1] that have to be given as input parameters after that the system will be iterated according to Equation 10. The real solution of problem is [3;1] and the system can converge this solution 0.030 seconds but if you have huge numbers of parameters such as UAV data sets, it will take a long time to find the solution of problem.

RESULTS	ITERATION	TIME	RELAX. PARAMETER
1.04\0.78	10	0.032 SC	0.1
1.78\0.92	10	0.032 SC	0.2
2.28\0.94	10	0.031 SC	0.3
2.61\0.96	10	0.033 SC	0.4
3.0\1.0	10	0.030	1.1

TO START 10 ITERATIONS

TO START 15 ITERATIONS

RESULTS	ITERATION	TIME	RELAX. PARAMETER
1.41\0.89	15	0.031 SC	0.1
2.22\0.96	15	0.032 SC	0.2
2.64\0.97	15	0.032 SC	0.3
2.85\0.98	15	0.031 SC	0.4
3.0\1.0	15	0.033	0.9

Figure 18. Demonstration of ART algorithm

The projections are generally cyclical due to the given order in the linear system. However, Cenker (1992) and Herman (2009) demonstrated that random selection in linear systems can actually produce better solutions than cyclic order. This is considered later as a part of my research question. The selection of the equation order is an important step of any ART algorithm. Strohmer and Vershynin (2009) developed a randomized version of the Karcmarz algorithm which is used to sometimes define normalizing equations. In this, the i index in Equation 11 is selected randomly with probability proportional to $\|a_i\|^2$. This method converges at an exponential rate by estimating the error after k iterations depending on the scaled condition number of A. Strohmer and Vershynin (2009) showed that randomized selection achieves a fast convergence rate that depends on quantities that are more-closely related to the singular values of the matrix A. In this study, the performance of the research problem (x matrix) was done by and can also be checked using this method as per this study.

The processing of research problem requires a powerful computer because of enormous data sets so the Blue Crystal in University of Bristol was used for running inversion algorithm. The processing for Kobachi weighbridge survey site took one night to get solution which we expected.

5.4. Current and Proposed Methodology of Hyperspectral Imaging (HSI)

Standard colour imaging utilizes three broad spectral channels; Red, Green and Blue. It is often referred to as RGB imaging. Although RGB images are easily understood by humans they lack sufficient spectral information to be useful scientifically. To be useful scientifically, more data points and spectral resolution is required. This could, for example help in the identification of materials (Shippert, 2004), geological mapping (Kokaly et al., 2011) and plant health assessments (Anderson et al., 2018). These high spectral imaging techniques are normally referred to as hyperspectral imaging.

Specifically, Schelkanova (2015) defined that "hyperspectral imaging (HSI) is a spectral imaging acquisition where each pixel of the image was employed to acquire a set of images within certain spectral bands". (Schelkanova, 2015; Chein-I, 2003;Grahn et al. 2007). Typically, hyperspectral imaging is undertaken in the UV-VIS-NIR region of the

electromagnetic spectrum. A spectrum is recorded at each pixel in the image, so it produces a continuous image at many wavelengths broken down into tens or hundreds of spectral windows.

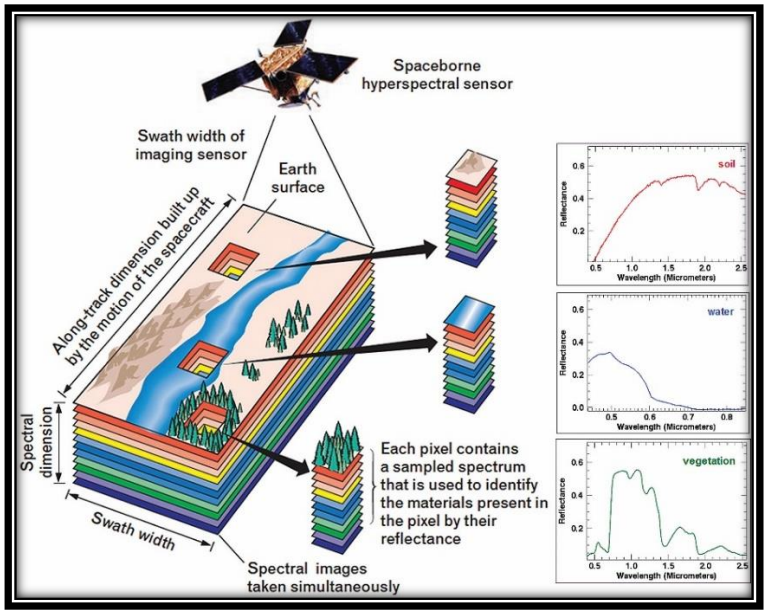

Figure 19. Current methodology for hyperspectral imaging from [15]

However, with UAV deployed gamma spectrometers it should also be possible to conduct HSI in the gamma regime. Instead of merely calculating total counts, the gamma spectral values can be used to produce a hyperspectral gamma image (HSGI).

Hyperspectral gamma imaging is a novel approach for interpreting of gamma spectral data and appears to be the first time that this has been done for radiometric data processing. There is no previous mention of HSGI in any published literature.

As with conventionally HSI, HSGI consists of both spatial information (i.e. images or maps) and spectral information (i.e. gamma spectra). Therefore with HSGI it is possible to visualize the distribution of different radioisotopes, which is not possible from currently utilized radioactive intensity maps which are simplistically derived from total counts data. The relevant data processing code and associated results pertaining to HSGI can found in Appendix I and the results section of this report.

6. THE IMAGE RECONSTRUCTION OF THE RESEARCH QUESTION

Writing a linear equation as discussed in section 5.3.2. and calculation of geometry and energy calibration for reconstructing the images are the most important parts of the image reconstruction process. In this study, the 'A' matrix (Eq. 9) explained in section 6.1. was defined as the "Efficiency matrix" , whilst the x matrix was developed as expected to solve real total counts and b was derived from total gamma ray counts taken from the UAV`s spectrometer (Eq. 9). The computation of required parameters for image processing were described as follows. The newly developed inversion method for pin-point radioactive sources on the ground from UAVs was programmed by MATLAB 2018a software (Hansen et al., 2004; Prol et al. 2017) and ran these codes with Blue Crystal in University of Bristol. The Matlab scripts and all data sets are shown in Appendix I.

6.1. A Matrix Calculation of Research Problem

Mathematically, calculation of the efficiency matrix (A) can be described for a homogeneous absorber as follows:

$$A = r * \exp(-\mu\rho d) \tag{11}$$

"d" is the calculation of the distance of drone from ground coordinates (m) , "r" is the calculation of ISL parameter depend on "d" parameter (m), "μ" is the coefficient of attenuation depend on material/ energy levels of radiation (cm^{-1}) and "ρ" is the air density (gr/cm^3) which will be explained in Section 6.1.1 and 6.1.2 , respectively. Calculation of A matrix covers ISL and energy attenuation for the research problem.

6.1.1. The Calculation of Inverse Square Law for A Matrix

The inverse square law (ISL) is the main problem for total counts readings derived from UAVs which was mentioned in section 2 and 5.2. To solve this affect, firstly, distance has to be calculate based on drone and ground coordinates with "d" formula in Figure 20 and then ISL formula has to be implied for each data points.

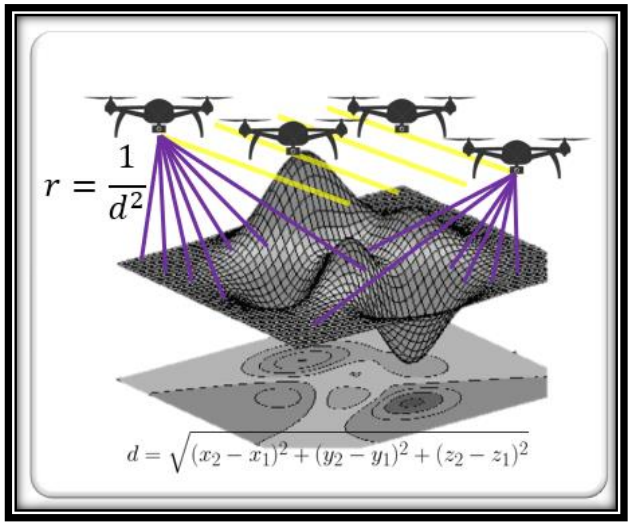

Figure 20. Inverse Square Law for A matrix

6.1.2. The Calculation of Energy Attenuation for A Matrix

The calculation of energy attenuation in the air of gamma photons is the second important parameter to add into the "A" matrix to define the research problem in detail. The gamma radiation absorption coefficient of air varies in the energy range 0.01 to 3 MeV. This coefficient is a product of Compton scattering, photoelectric emission and pair production interactions. Grodstein (1957) calculated and presented values of the total absorption coefficient over the range 0.01 to 100 MeV for a number of materials, including air. Their method to calculate the absorption coefficient curve proved inaccurate at energies below 50 keV but accurate to within 1% for all other energies. For low energies, Grodstein employed a revised value of 1.02.* However, even at 0.1022 MeV, photoelectric absorption is only about 2.5% of the total, so that the resulting discrepancy in the latter is not more than 0.5%. Due to these inaccuracies at lower energies the assumed absorption coefficients used in this report were based upon the empirical formula developed by J. W. Allison in 1958. This equation is accurate at all relevant energies to within 5% of actual values.

$$log_{10}\frac{\mu}{\rho} = \sum_{n=0}^{4} a_n \left(-log_{10}E\right)^n \qquad (12)$$

where a_0=-1.1945, a_1=+0.49234, a_2=-0.12414, a_3=-0.056958 and a_4=+0.061026. ρ is air density in g/cm^3 (Allison, 1958) . Air temperature, air humidity and air pressure at the

Chernobyl site were used to estimate the applicable air density. From 21st April 2019 to 23rd April 2019 in the air temperature in Chernobyl varied between 17 °C and 24 °C whilst the air humidity varied between 30% and 31% and air pressure changed 1027mbar. According to these values, the relevant air density was calculated as 0.0012341 g/cm^3.

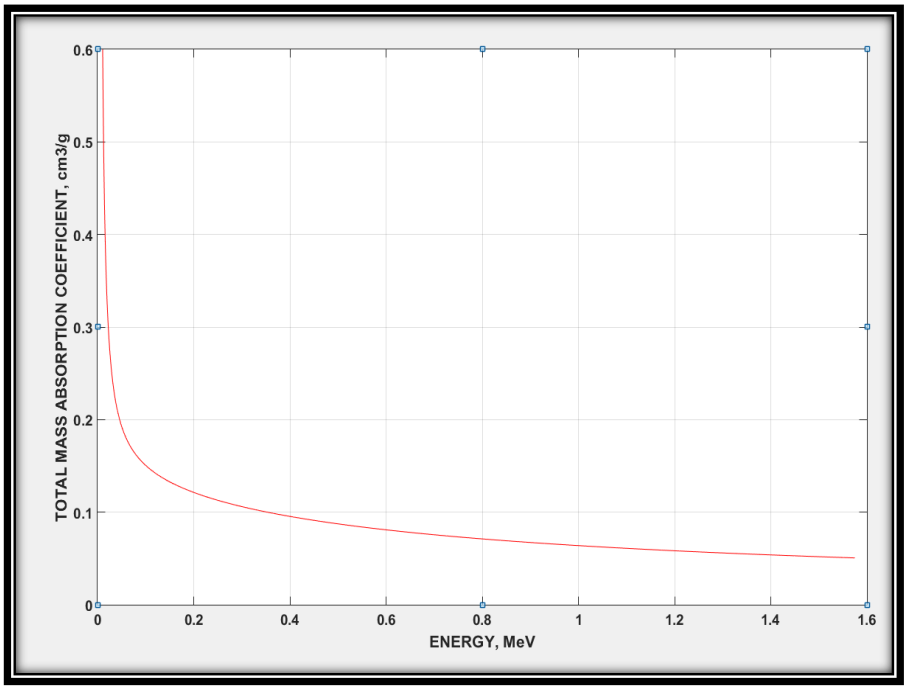

Figure 21. Total mass absorption coefficients of air for the energy range 0.0 - 1.6 MeV

The figure 21 shows the attenuation coefficients as a function of energy in the range 0 to 1.6 MeV as calculated with Allison's empirical equation (Allison, 1958).

6.1.3. The Calculation of Relative Error

The relative error is a measurement of precision of the recovered radiation map based upon the difference of the measured values (recorded total counts derived from UAVs) and estimated values (real total counts after inversion process). The Relative error formula is given below:

$$\delta x = \frac{\Delta x}{x} = \frac{x_0 - x}{x} = \frac{x_0}{x} - 1 \qquad (13)$$

Where Δx is the absolute error value. Relative error varies between zero and one. As the relative error approaches zero then the accuracy of the prediction in greater. The percentage error is equal to 100 times the relative error.

6.2. The Proposed Workflow of Full Inversion Process

The proposed workflow of full inversion process can be divided into 5 parts: (i) preparing high spatial DEM data for ground coordinates derived from photogrammetry, (ii) preparing inversion input parameters and the running of the inversion algorithm coded by ART algorithm (the randomized Karcmarz) (iii) storing the data by using HSGI technique (iv) calculating relative errors and (v) checking results.

These steps are summarized as below.

1. Prepare a Digital Elevation Model (DEM) of ground level for the survey area. The resolution of the DEMs may be down sampled to speed up the inversion algorithm processing.
2. Convert the survey coordinates system into the same coordinate system as the DEM.
3. Select a suitable iteration number and relaxation parameter.
4. Calculate the efficiency matrix (A) by using formula on section 6.1.1. and 6.1.2.
5. Estimate the radiation distribution using a randomized Karcmarz method.
6. Store the inverted total counts by using HSGI technique on section 5.3.4.
7. Check relative errors for inverted total counts by using formula on section 6.1.3.
8. Analyse energy spectrum via radiometric isotopes.

All demonstrations of full inversion process and its codes will be shared in results section and Appendix I, respectively.

7. Field Sites and Data Acquisition

7.1. Kobachi Weighbridge (Chernobyl, Ukraine)

The Chernobyl Nuclear Power Plant (CNPP) is located near to the Ukrainian city of Pripyat, at 51°23′21″N 30°05′58″E 14.5 kilometres northwest of the city of Chernobyl, 16 kilometres far from the Belarus–Ukraine border, and approximately 110 kilometres north of the Ukrainian capital, Kiev (Figure 22). At the time of the incident, it contained four active RMBK-1000 reactors each producing 1,000 megawatts capacity of power. This equalled to generating of about ten percent of Ukraine`s domestic electricity demand until the incident. The first reactor construction began in 1970 but the construction of Reactors No: 5 and 6 were never completed due to the disaster.

Figure 22. An aerial photograph of the CNPP and the Red Forest (April 2019) and the height of the CNPP is around 100 m.

The nuclear accident (itself rated at Level 7 on the INES scale (IAEA, 1990)) occurred on the 26 April 1986 at the No. 4 nuclear reactor in the CNPP. According to the World Nuclear Association in 1986, "two CNPP employee died on the night of the disaster, and a further twenty-eight people died within a few weeks because of acute radiation poisoning" (WNA, 1986). The Chernobyl accident in 1986 was caused the largest

radioactive releases into the atmosphere in the 10 years of its energy production. After the accident, the citizens and animals were evacuated from an area of approximately 3500 km^2 around the CNPP; this area was increased as 4760 km^2. Approximately 2600 km^2 of this restricted region was defined as the Chernobyl Exclusion Zone (CEZ) by Ukrainian government (Dyker, 1987). This zone can be seen in Figure 19 and it is still highly contaminated by radioisotopes of ^{137}Cs, ^{90}Sr, ^{241}Am and Pu; but many shorter-lived radionuclides have already decayed (Kashparov et al., 2018). The Quaternary geology of the region consists of 30-40 m of Late Pleistocene – Holocene alluvium and sandy deposits which possess as yet undefined aquifers (Matzko et al. 1994)

It is known that the Ukrainian government buried highly radioactive waste in some villages of CEZ after the accident and they wants to build up big solar power plants within 10 years in these areas that's why the presence of surface water, a shallow water table and porous aquifers will cause changes in distribution of radioactivity levels throughout the sediments so environmental radiation mapping surveys have to be done over these areas during years.

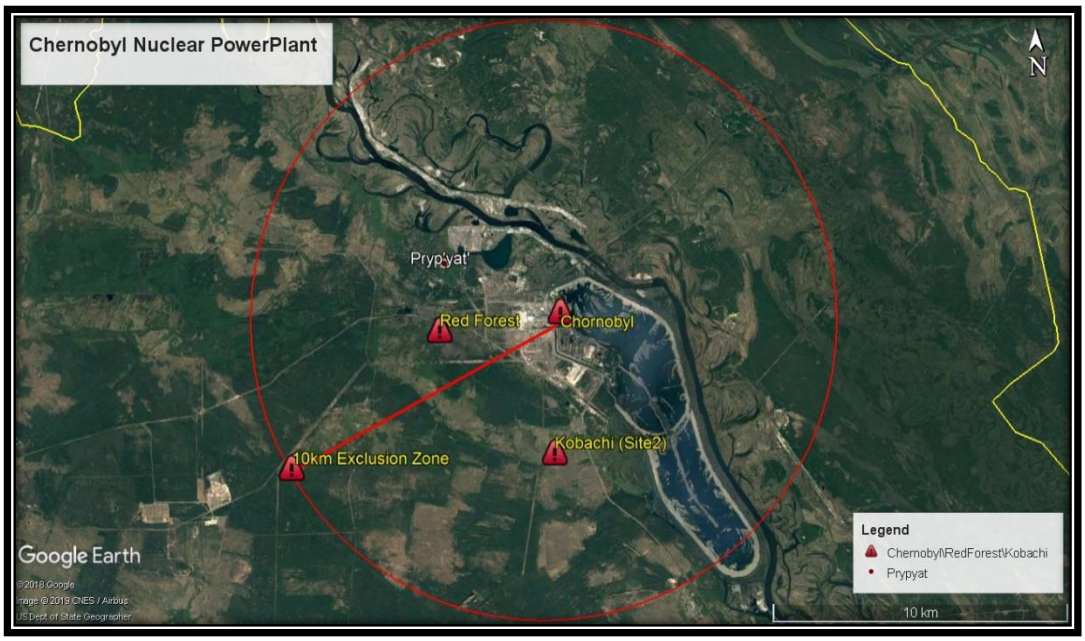

Figure 23. The Chernobyl Nuclear Power Plant Exclusion Zone and Kobachi weigh bridge (Chernobyl, Ukraine). The big red circle was defined 10 km CNPP Exclusion Zone

With the need for detailed monitoring in mind, a radiation mapping project was undertaken at CNPP. Data collection completed within 10 days from 15th April 2019 to 26th April 2019 even the last day of survey crossed the anniversary of CNPP incident. It was done by the author of this research, Prof. T. B. Scott, Dr. K. Wood and D. Connor as a team.

Data acquisition compromised two main surveys. The weather on the first day of survey was quite rainy, and then it was constant until the end of survey duration. The first survey was intended to start measuring radioactive levels in the Red Forest area, the most affected region of the accident, with the newly developed fixed-wing aircraft system built by the University of Bristol's Aerospace Engineering Laboratory. The second survey aimed to use backpack-based radiation detectors. After the analyses of raw data derived from the fixed-wing aircraft, a further survey was undertaken to explore the impact of the new inversion algorithm for using multi-rotor system in this site (latitude /longitude = 51.34°N / 30.11°E defined as Kobachi weighbridge (Chernobyl, Ukraine)) conducted around the site of Kobachi (Figure 23 and Figure 24). The dimensions of this survey location are 180 m x 130 m.

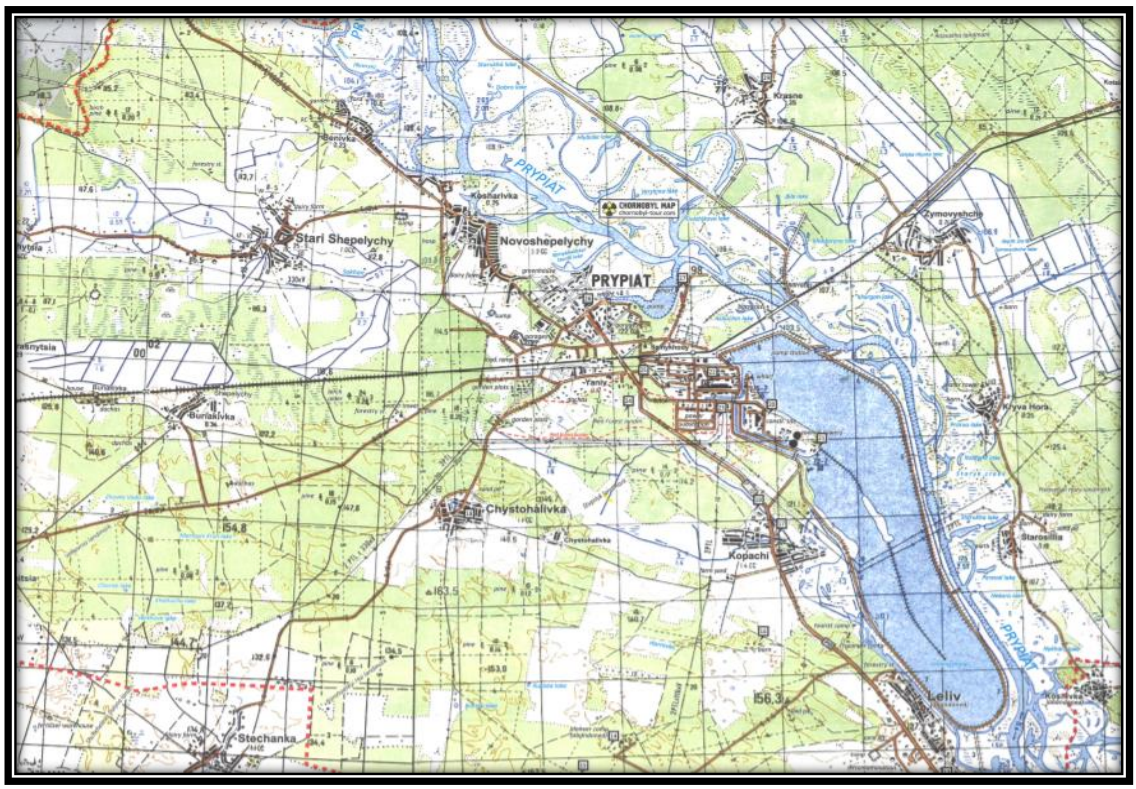

Figure 24. The detailed location map of CNPP

After that, the Kobachi weighbridge (Chernobyl, Ukraine) study area was extended to encompass a wider area termed the Kobachi mechanical yard study area (Chernobyl, Ukraine) (Latitude = 51.3417-51.3480 / Longitude = 30.1064-30.1133) to test the accuracy of the inversion algorithm (Figure 25). This survey site was used for farming operations before the disaster and the highly radioactive dumps, tractors and small hotspots were mapped by Geiger Muller and backpack-based radiation detectors to provide data for ground truthing on the survey site. Aerial mapping was done by the multi-rotor (M600 as mentioned in section 7.2.1) and fixed-wing (Titan as given in section 7.2.2) system. Unfortunately, data collected by backpack system only covered half of the Kobachi mechanical yard study area (Chernobyl, Ukraine) because of the permission restrictions.

Radiation levels in Kobachi weighbridge study area (Chernobyl, Ukraine) and Kobachi mechanical yard study area (Chernobyl, Ukraine) have never been mapped in the literature.

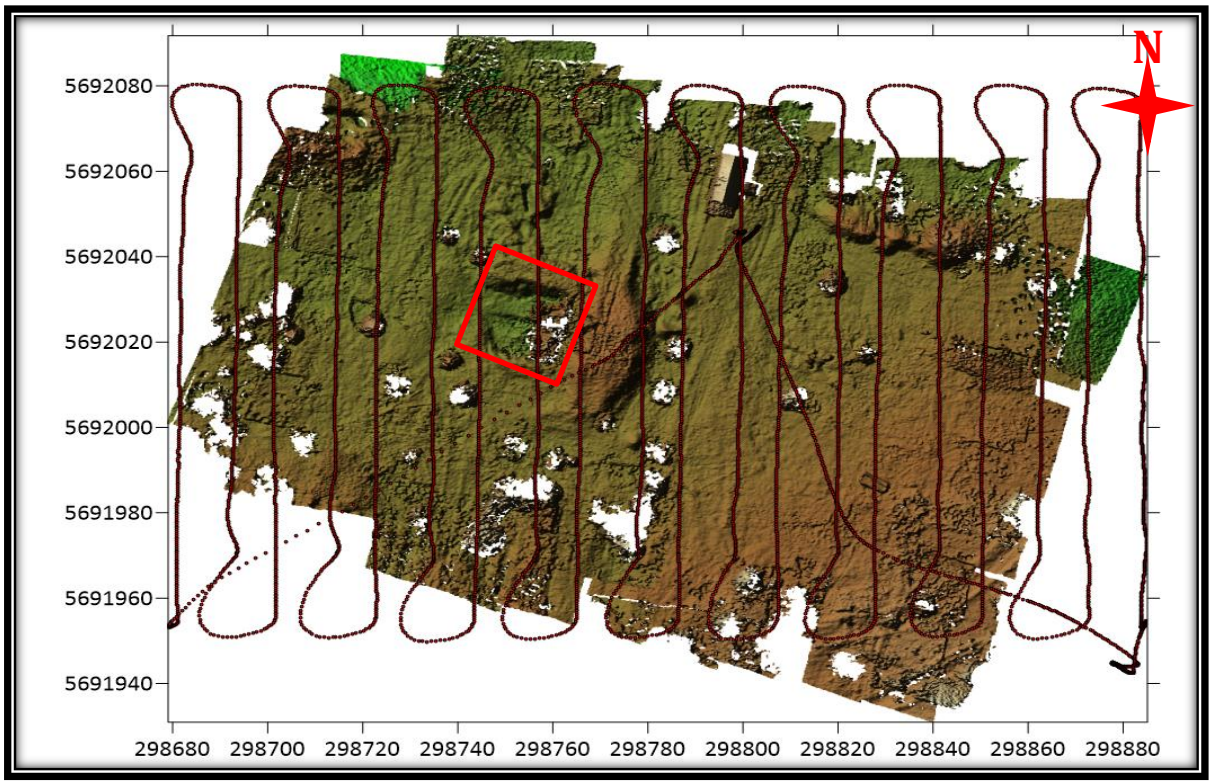

Figure 25. The location of Kobachi weighbridge (Chernobyl, Ukraine) and the red dark points were utilized the multi-rotor flight path

All coordinates recorded by the detectors and other instruments were in WGS 84 coordinate system (degrees, minutes and seconds). For simplicity during the data processing stage, all these measurements converted to the metric Universal Transverse Mercator (UTM). This is because UTM's unit of measurement is in meters rather than degrees. All data was processed and presented using a combination of Google Earth Pro, Surfer 16 and ArcGIS, respectively. The Kobachi weighbridge (Chernobyl, Ukraine) and Kobachi mechanical yard (Chernobyl, Ukraine) study sites are illustrated in detail in Figure 26.

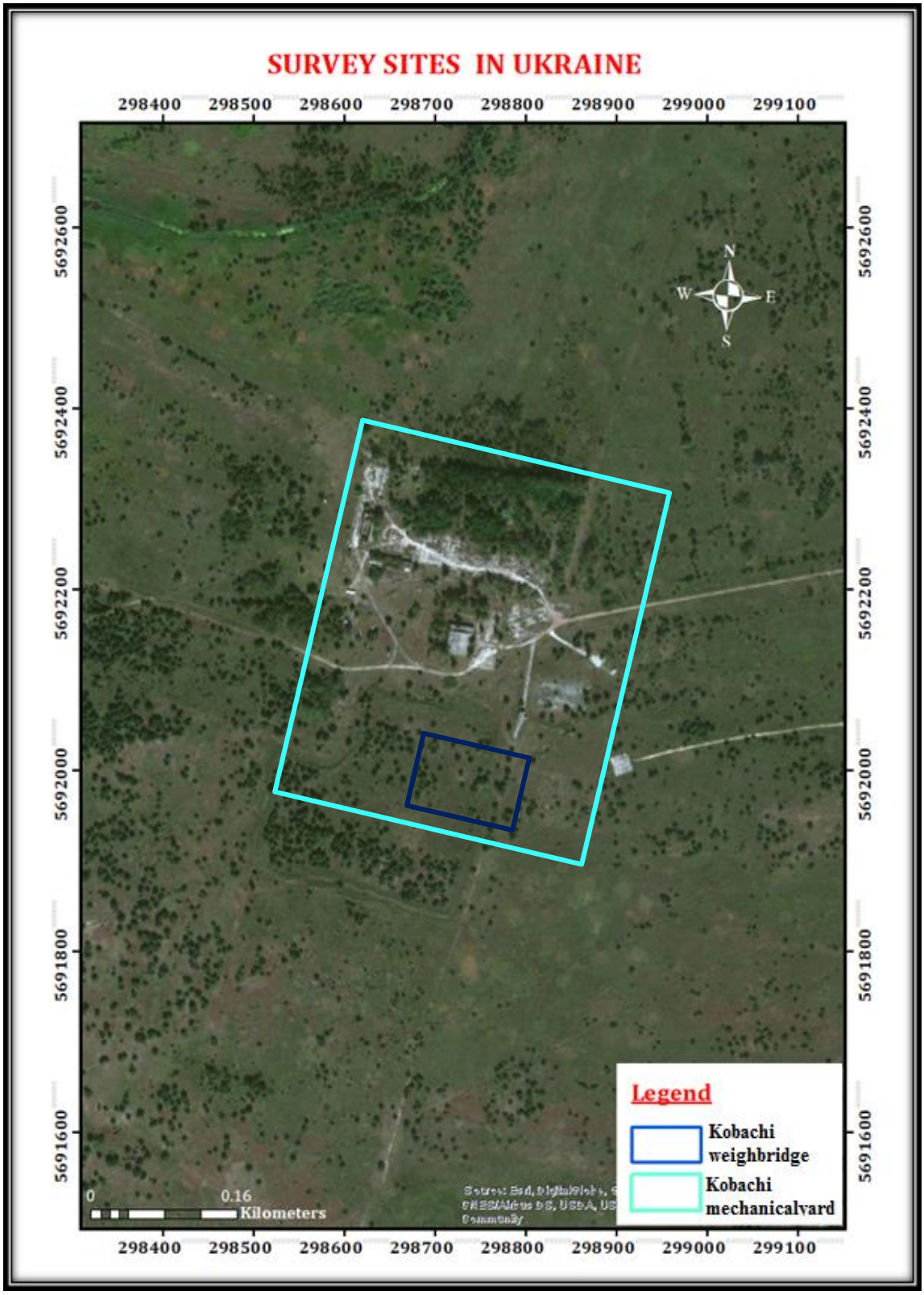

Figure 26. Kobachi weighbridge (Chernobyl, Ukraine) and Kobachi mechanical yard (Chernobyl, Ukraine)

7.2. Unmanned Aerial Vehicle Systems and Detectors Used in This Study

The selection of the UAV systems and detectors which have an appropriate energy resolution, high detection efficiency and are portable are important for environmental radioactivity surveys. Two systems, which have the same core design (Connor et al. (2018) and Connor, Martin, Pullin et al. (2018)), were chosen. The general system uses CsI(Tl) gamma-spectrometer package (from Kromek Ltd.), which has an 50 keV – 2 MeV energy, with an energy resolution of < 7.2 % @ 662 keV. This is coupled to a barometer, a GPS unit and a single-point laser rangefinder for measuring height above ground levels (AGL) (Figure 27). This detector was mounted on all of the UAV systems used for these studies.

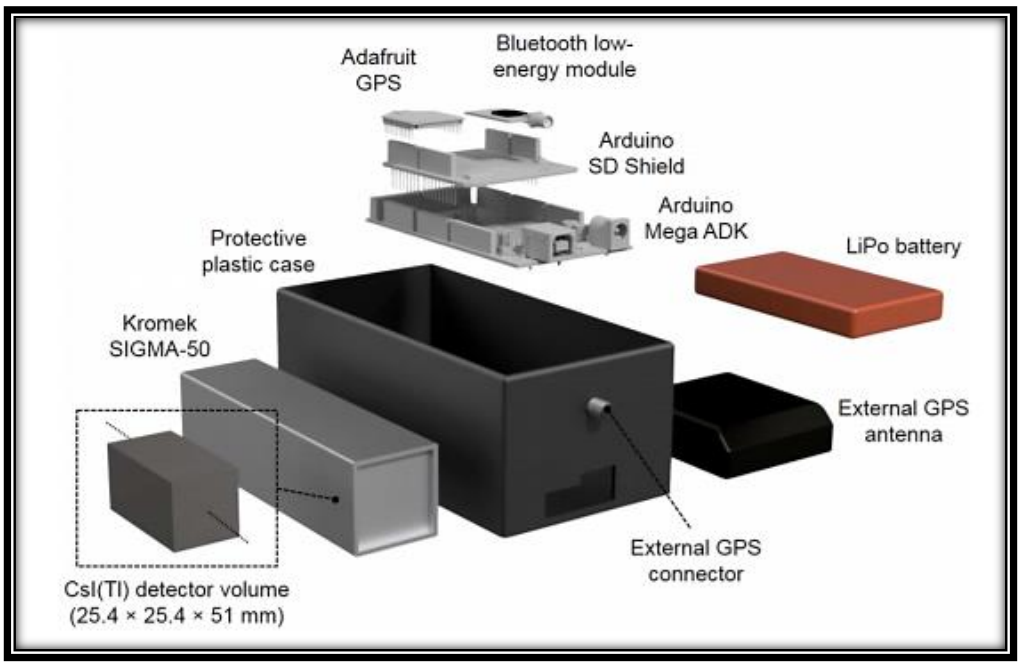

Figure 27. SIGMA-50 (CsI(Tl) Scintillator detector from [19]

7.2.1. Fixed-wing UAV System

A Titan Skywalker fixed-wing UAV, with a maximum take-off weight of six kilograms and a 2.1 m wingspan, was the preferred vehicle for radiation mapping in Ukraine (Figure 28). This system is capable of around 45 - 70 minutes flight duration by using Lithium Polymer (LiPo) batteries. The survey site in Ukraine scanned in parallel patterns with 40-60 meters of grid spacing and 40-60 m of flight altitude for a full ground coverage in Kobachi mechanical yard (Chernobyl, Ukraine). This is the first time a dual system has been used in Red Forest area.

Figure 28. The Titan Skywalker fixed-wing UAV

7.2.2 Multi-rotor UAV System

A DJI Matrice M600 multi-rotor UAV systems was used for this work in the Ukraine for high resolution surveys (Figure 29). The combined systems (UAV and detector box) are around 15 kg and is able to fly around 20 minutes for M600. Target altitudes in Ukraine were between 5 and 40 m. The survey site dimensions varied approximately 150 x 150 m respectively. The flight line spacing for all surveys is equal to the altitude of flight.

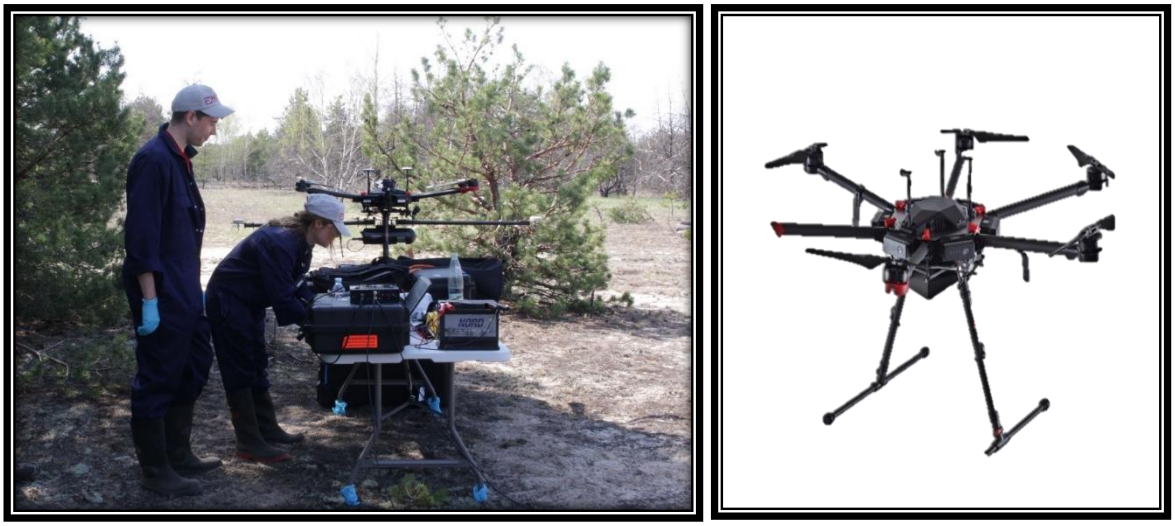

Figure 29. The multi-rotor UAV and system modified from [16]

7.3. 3D Surface Reconstruction of Survey Sites

7.3.1. Photogrammetry

Photogrammetry produces 3d scenes from a set of images. Each picture is compared to all other pictures and merged by using correlated focal points and image matching algorithms to assemble 3D model of a scene (Stefanik et al. 2013). This procedure for obtaining 3D reconstructions can achieve ~10 cm resolution both horizontally and vertically.

One system was used record photogrammetric input data for the survey sites:

- A DJI Mavic Pro camera was used with the following specification: (Figure 26b). Its sensor and lens properties are 1/2.3" CMOS and FOV: about 83° (24 mm); about 48° (48 mm format equivalent) f/2.8 24 mm)-f/3.8 (48 mm). Focal range =0.5 m to ∞. These images also includes 3D coordinates captured view from the survey. 101 images, recorded in JPG format, were captured in Kobachi weighbridge (Chernobyl, Ukraine).

The images derived from Mavic Pro were processed with Agisoft PhotoScan which is an advanced 3D modelling software for producing 3D point clouds. To start data analysing, Agisoft Photoscan needs at least two images from users. Both alignment of image and reconstructions of 3D model were fully automated.

Figure 30. DJI Mavic Pro from [16]

7.3.2. 3D Scanning Light Detection and Ranging (LIDAR)

LIDAR use laser pulses to create 3D models and maps of objects, features and environments. These systems measure the time-of-flight between laser beam transmission and receipt of the reflected light pulse to calculate distances. The LIDAR mapping system used in this study included an integrated Inertial Measurement Unit (IMU) and Global Navigation Satellite System (GNSS) receiver which allowed each measurement or point to be georeferenced. Each point merges to create a 3D visualization of the target object or site.

For this project, a Routescene LidarPod, consisting of a survey grade LiDAR sensor, RTK GNSS\INS, data storage, radio telemetry (Figure 27), was used to reconstruct nearly half of the northern part of Kobachi weighbridge survey site. LidarViewer software was used to analyse raw data consisting of 3D coordinates of survey sites derived from the LidarPod for 3D point cloud. This software will construct a 3D point cloud in real time. The first frame is displayed in relative mode relative to the scanner. The user is also able to colour the points in different ways such as colour by height, intensity, distance. Moreover, this software has an extra filter tool to create a bare earth model in one-step, which users may need to give a number describing the highest obstacle of the survey site.

Figure 31. Routescene LidarPod [17]

The set-up time for the Mavic Pro is shorter than the Routescene LidarPod but the data analyses in LidarViewer are more practical and efficient than those of Agisoft PhotoScan. This is because the 3D scene is a direct product of the LIDAR scanning whereas the 3D model from photogrammetry requires computationally intensive post-processing.

7.4. Processing of Photogrammetry derived from Mavic Pro on Survey Sites

In Agisoft, processing steps are separated into two parts. Firstly, Photoscan creates a textured 3D model using pictures taken by a UAV mounted camera mentioned in section 7.3.1 across the survey site and then the second part is the creation of point clouds. Using the automated processing procedure described below and in Figure 32. The following was obtained from [18].

a) The first stage is camera alignment, during which PhotoScan searches for common points on photographs and matches them due to position of the camera for each image and clarified parameters of camera calibration. Finally, it creates a sparse point cloud and a set of camera positions.

b) The second stage is to produce a dense point cloud based on the determined camera positions and images themselves. This uses a network bundle adjustment (NBA) algorithm to form a series of dense points between the spare point clouds

c) The third stage is to produce a 3D polygonal surface mesh based on the dense or sparse point cloud. Generally, 3D mesh creation uses two algorithmic methods: Height Field - for planar type surfaces (2.5D), Arbitrary – for a fully 3D reconstruction. Some changes, for instance mesh decimation, removing some segments, covering holes in the mesh, making a smooth mesh can be performed by the software. External 3D editor tools are convenient for complex editing outside of the Photoscan. The software allows for the exporting of the mesh in many different file formats.

d) After the reconstruction of the surface geometry (i.e. the mesh) the user is able to create 3D Digital Elevation Model (DEM). A DEM is a 2.5-dimensional description of the geographic surface. It can be exported with specific pixel resolutions and defined boundaries of the survey site in *.tiff, *.xyz or *.kml formats.

As previously highlighted, the LidarViewer software requires fewer processing steps to produce a 3D model. The raw data from the Lidar pod was imported and clipped to include just the survey area data. A series of automated filter algorithms are available for clearing and exporting data into bare earth models.

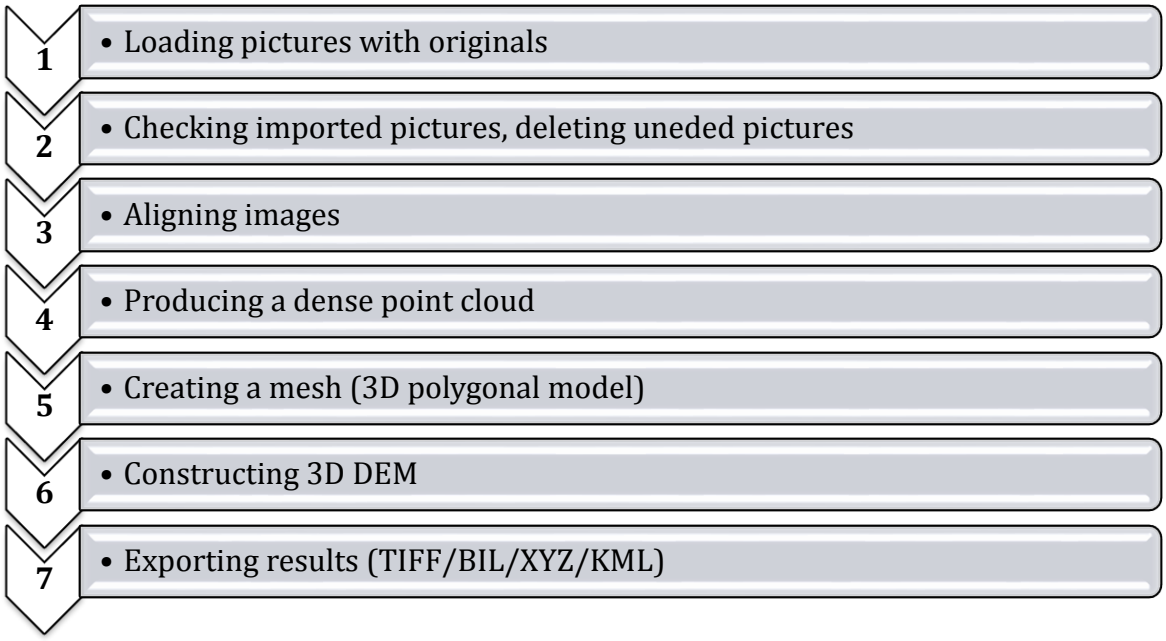

Figure 32. General workflow modified from [18]

7.5. Processing of Photogrammetry derived from LidarPod on Survey Sites

The LidarViewer software was used to build a 3D model using a LiDAR processing workflow. The only required user interaction was to import the raw data and select some parameters. The UAV flight paths can be tracked step by step. The software allowed the user to render raw data with different colours quickly. It was also possible to apply different post processing procedures such as laser or topography reduction to improve data quality.

8. RESULTS AND DISCUSSION

8.1. DEMs of Survey Sites

The DEMs derived from photogrammetry methods for the small Chernobyl site (Figure 25) had a spatial resolution of 1.02 cm/pixel. The prepared 3D dense point cloud contains 228609783 points (Figure 33). The DEM was cleared of trees, buildings and vegetation effects automatically to show just the digital terrain model (DTM) with process of classification of dense cloud points, in order to divide them in at least two classes: ground points and the rest, in the Agisoft PhotoScan software (Agisoft PhotoScan, 2010). This automatic procedure is that the dense cloud is divided into cells of a certain size. The lowest point is detected in each cell and triangulation of these points gives the approximation of the terrain model.

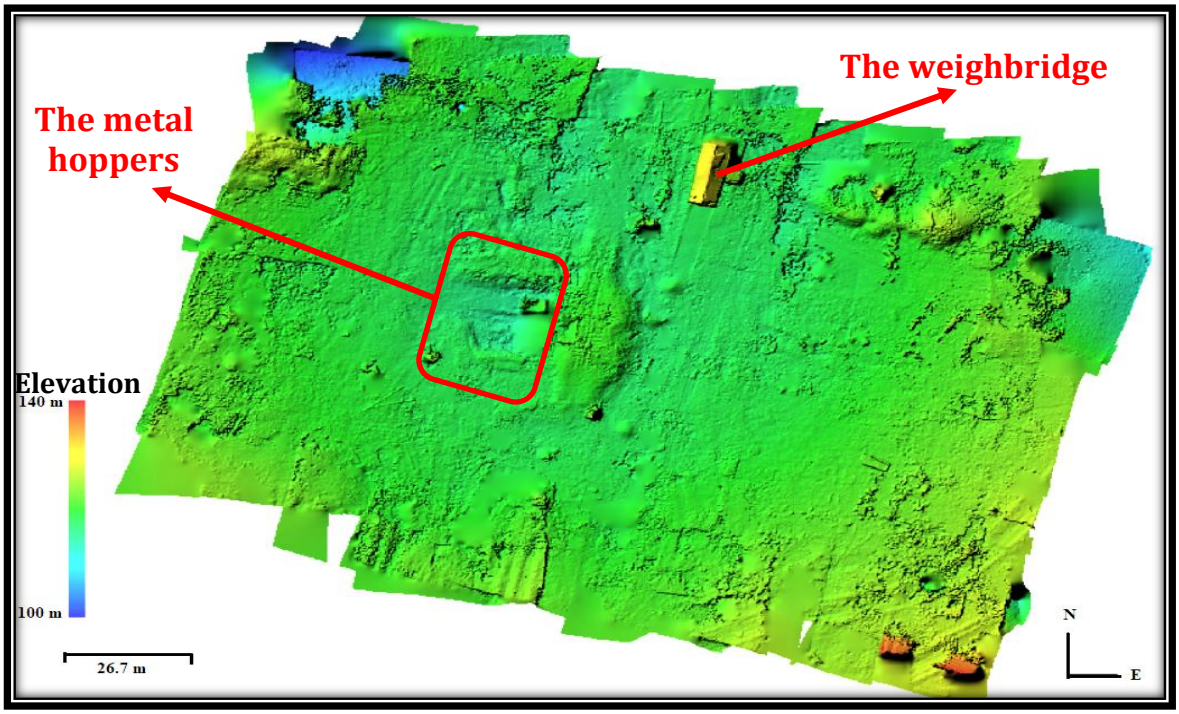

Figure 33. DEM of the small Chernobyl site

Figure 34 shows relative heights (as a metric units) in the northern part of a similar survey site including vegetation. As can be seen, most of the trees and buildings are approximately at the same height. The number of points in point clouds for this survey is over 30 million. The metal hoppers and the weigh-bridge coordinates can be seen in Figure 25.

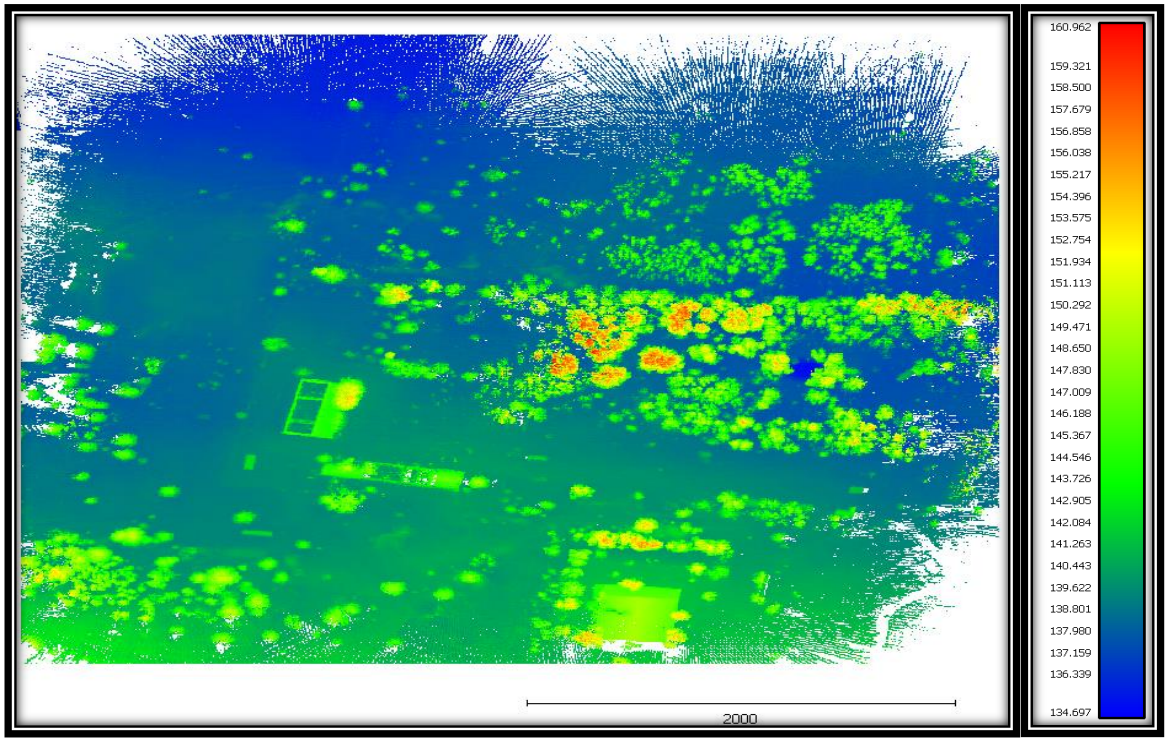

Figure 34. DEM for the northern part of larger Chernobyl survey site

Figure 35 shows the Lidar derived point cloud for the northern part of Kobachi weighbridge, derived by the LidarPod, prepared in RouteScene. Red colour signifies point clouds at lower elevation whereas blue indicates point clouds at higher elevations. As can be seen, the land is generally flat. White lines in the air shows the UAV tracks in Figure 35. Data collection was split into two flights, due to battery considerations. The length of flight lines and intervals are 237 m and 10 m, respectively.

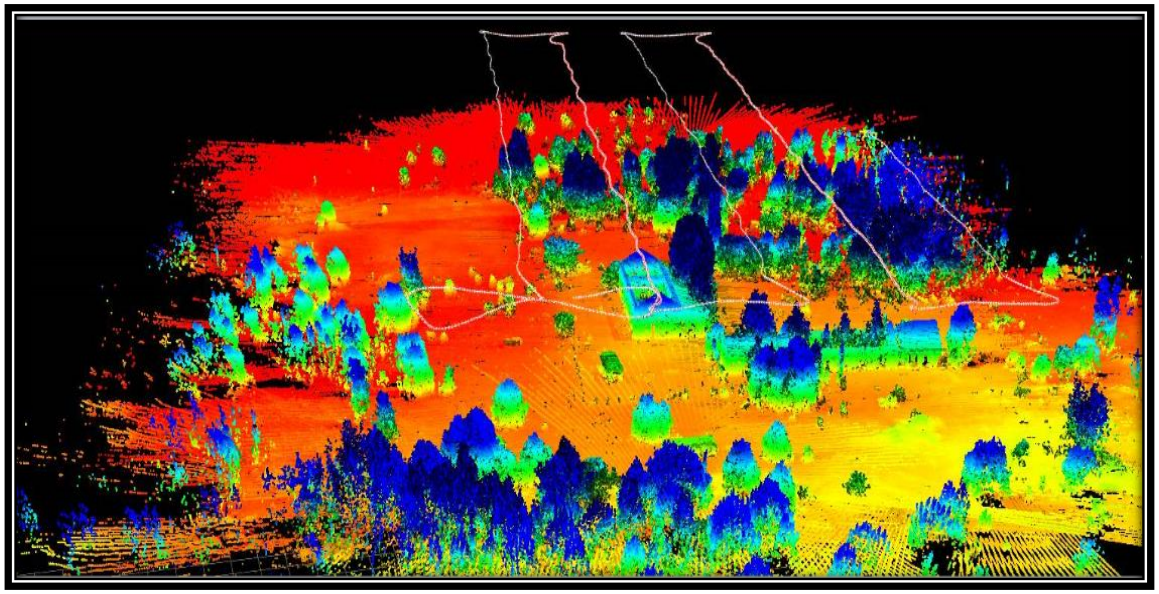

Figure 35. Digital elevation model for the northern part of Kobachi mechanical yard (Chernobyl, Ukraine) from [21]

8.2. Radiation Mapping of Survey Sites

Chernobyl sites were used as the sole location for radiation mapping studies. A wide area fixed-wing radiation mapping flights were conducted over the Red Forest, which covered both the smaller and larger survey sites near the former village of Kobachi. The total dataset recorded by fixed-wing system covered more than 15 km^2 of the area west and south of CNPP. Following the processing of raw data on the survey site as a team, a highly radioactive hotspot was discovered which is shown with the white circle in Figure 36. After the surprising discovery, the multi-rotor UAV was deployed to scan this area (Kobachi weighbridge (Chernobyl, Ukraine)) at a series of reduced altitudes of 15 – 40 m. Unfortunately, radiometric data was not collected at 50 m altitude with this system. Whilst this data would have been useful to collect to validate the results of the fixed-wing system, this was not possible. Two-dimensional radiation maps based on multi-rotor UAV flight altitudes were prepared by using the open-source IDW function for MATLAB (Figure 37). Though linear, cubic and nearest neighbour interpolation techniques were tested on data sets, IDW interpolation method gave the most accurate results compared to classical interpolation techniques for radiation intensity maps as it interpolates the intensity well, whilst veering the actual measurements values as true values.

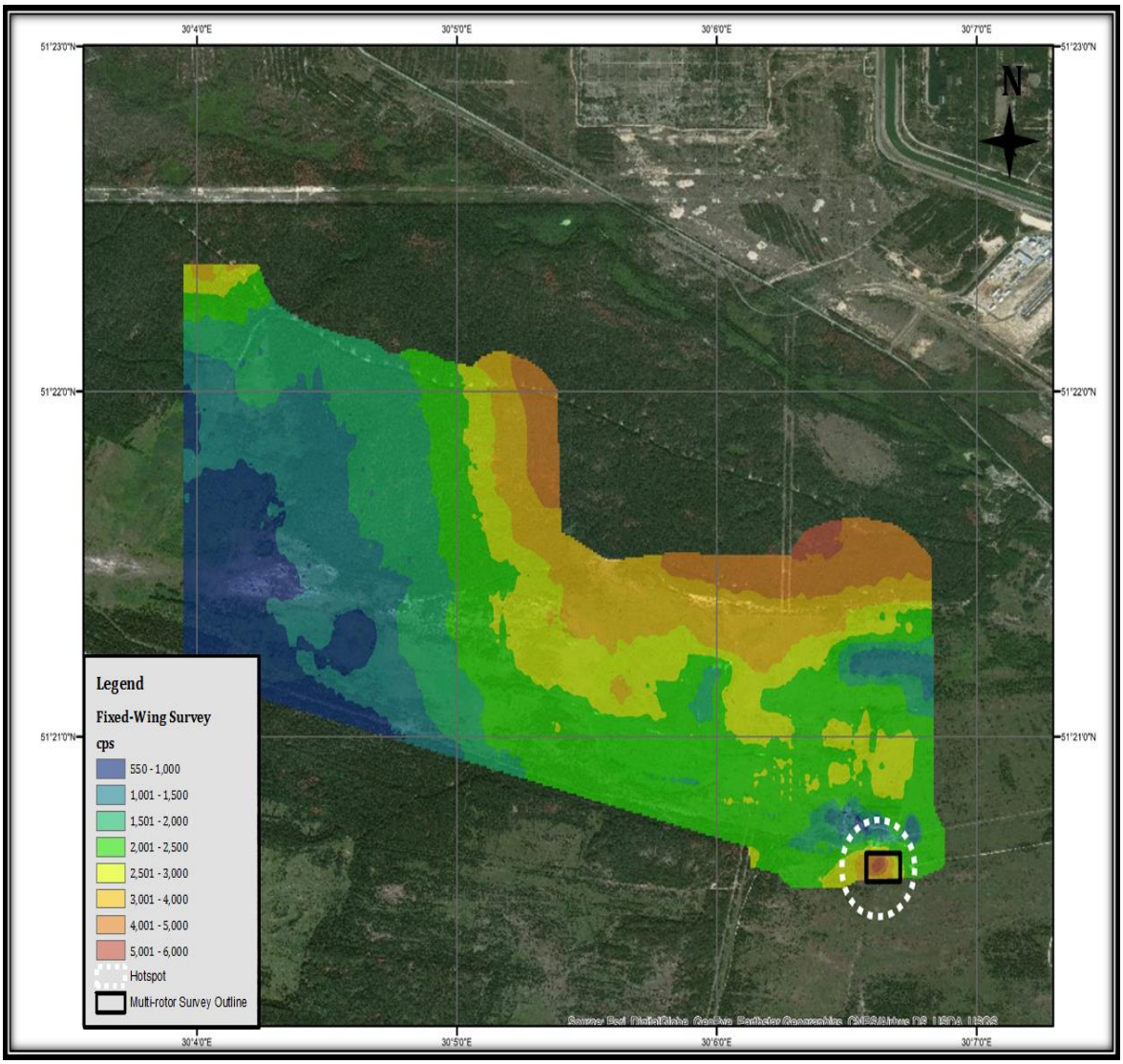

Figure 36. Radiation levels map of fixed- wing survey in CEZ (Connor, 2018)

The hotspot identified from the fixed-wing survey is presented multi-rotor measurements at 30 m altitude within Figure 37. This hotspot displayed persisting intensity values of between 300 and 600 cps. The detailed location of this anomaly is seen in Figure 25, drawn as a red square. According to recorded videos from UAVs, it is understood that it caused by a highly contaminated steel structure (Figure 38).

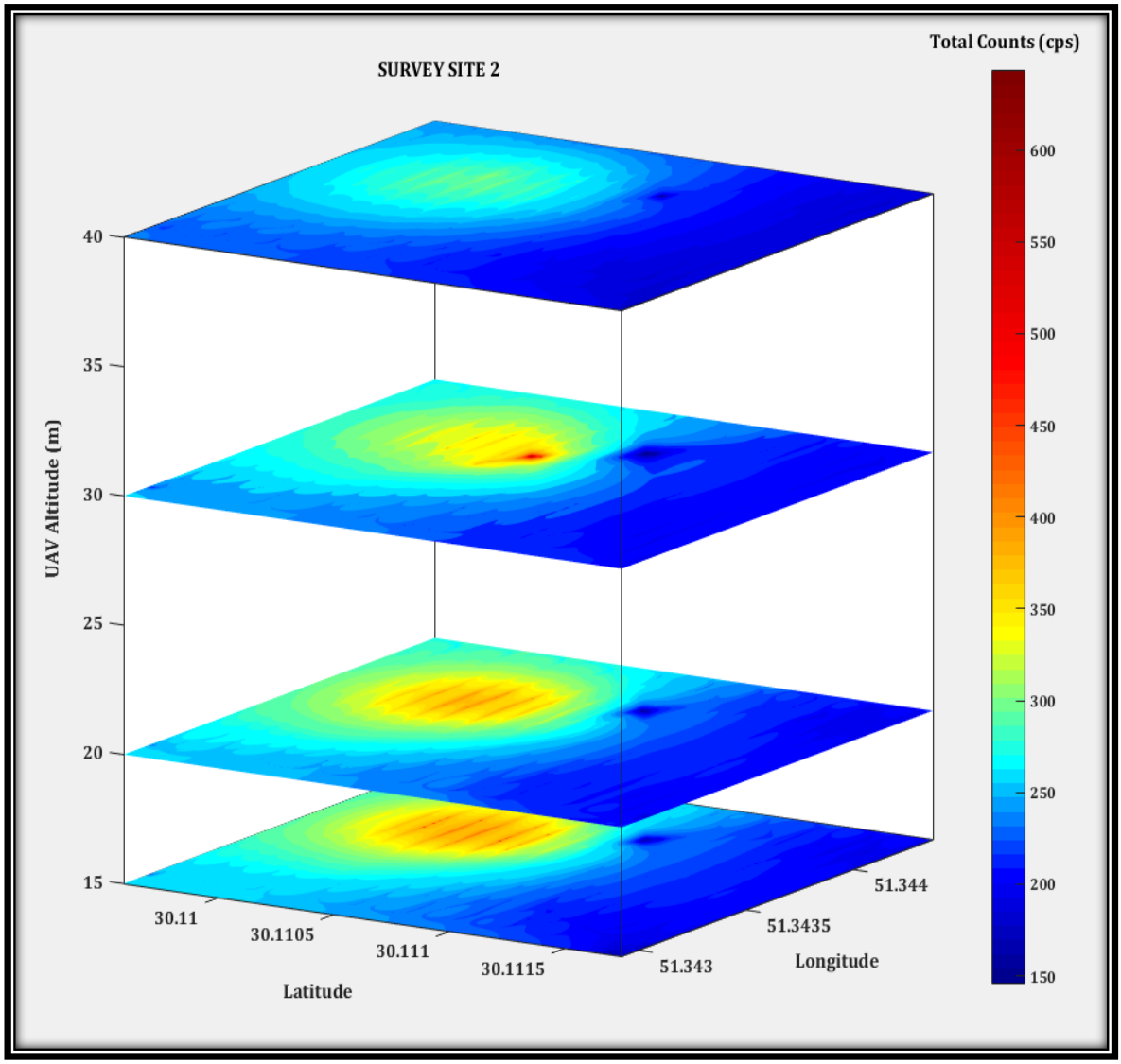

Figure 37. Radiation map for Kobachi weighbridge (Chernobyl, Ukraine) [22]

Figure 38. A zoomed- in view of the hotspot in the Kobachi weighbridge study area (Chernobyl, Ukraine) and the highest tree is around 40 metres.

Based upon the findings of the Kobachi weighbridge (Chernobyl, Ukraine) radiation map surveys were focused upon the Kobachi mechanical yard (Chernobyl, Ukraine) to understand the inversion algorithm`s sensitivity. Data collected from Kobachi mechanical yard (Chernobyl, Ukraine) included ground, multi-rotor and fixed-wing measurements. Although the fixed-wing radiation intensity data in Kobachi mechanical yard (Chernobyl, Ukraine) was corrected to 1 m altitude compared with the ground data, the two datasets were not self-consistent. Therefore, the Kobachi mechanical yard (Chernobyl, Ukraine) radiation map was visualised by using ground and multi-rotor data. It was also altitude corrected to 1 m altitude in MATLAB (Figure 39). The radiation intensity map displays a range of count rates from 10 to 400 cps. The mean intensity from the site was 200 cps. Highly radioactive readings (yellow circle) comes from the contaminated area around the Kobachi weighbridge (Chernobyl, Ukraine). The lower radioactivity levels (blue coloured regions) were also surveyed on the ground. The radiation levels depicted in green in Figure 39 corroborate the fixed-wing survey in Figure 36.

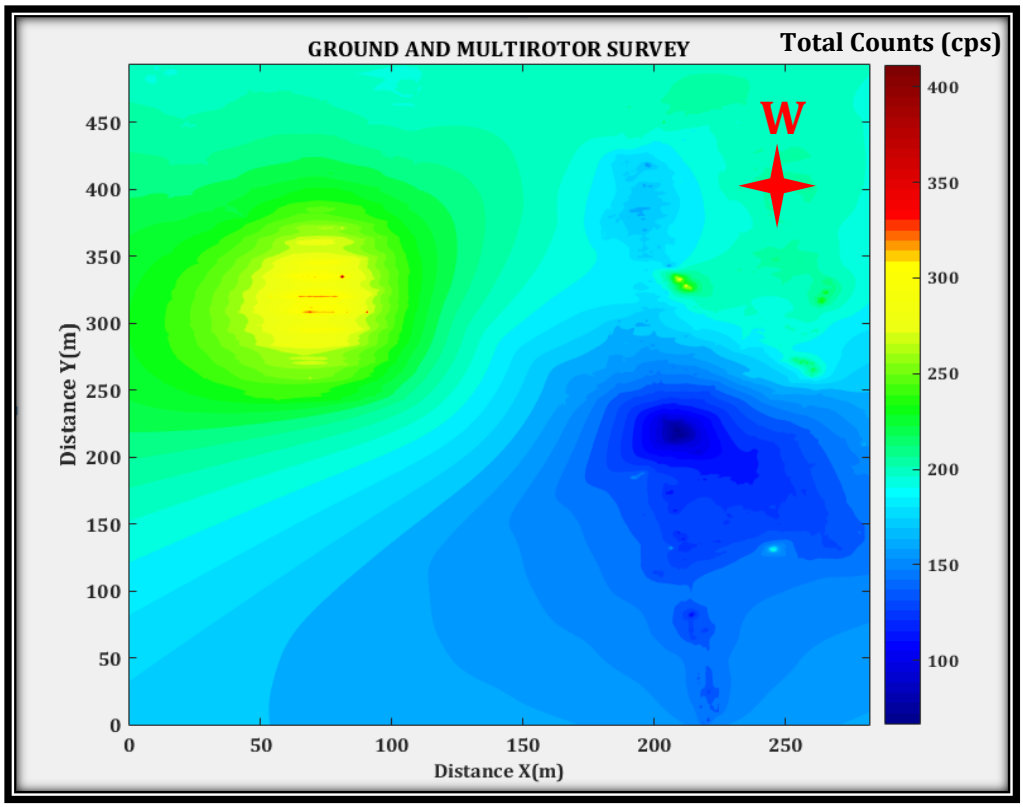

Figure 39. Radiation map for Kobachi mechanical yard (Chernobyl, Ukraine)

3D models of the Kobachi mechanical yard (Chernobyl, Ukraine) were obtained via lidar and photogrammetry. For the northern part of the site a 3D model was created using the data obtained by LidarPod, whilst for the southern part a 3D model was obtained via photogrammetry. Images were taken with the Mavic Pro UAV. There was no 3D model for the central region. The radiation intensity values (see Figure 39) are overlaid onto these 3D models to produce the image shown in Figure 40.

The northern part of area shown in Figure 40 was used for farm operations before the incident. In this area cps value ranged from between 10 to 250 cps and the buildings and trees also can be seen clearly. The southern part of the Figure 40 radiation intensity values vary from 150 to 300 cps and bare earth model was produced for that part. The highly yellow coloured shows the highly radioactive steel structure and the blue coloured sites describe safe zones for Kobachi mechanical yard (Chernobyl, Ukraine) (Figure 40).

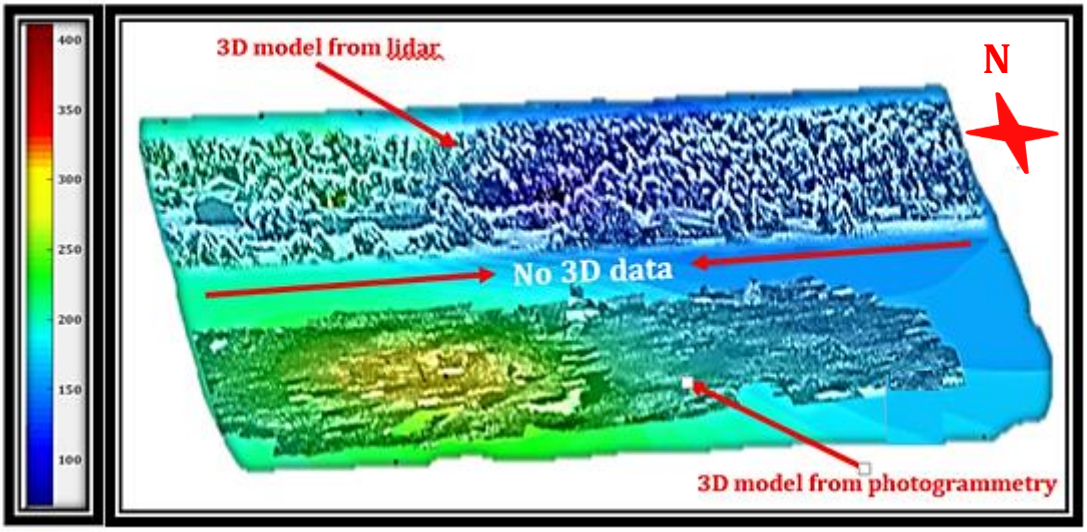

Figure 40. Detailed Kobachi mechanical yard (Chernobyl, Ukraine) radiation intensity map for tourism activities

The Kobachi mechanical yard (Chernobyl, Ukraine), is within the CEZ but is routinely used for tourism activities. As part of this work the image shown in Figure 40, was provided to the Ukrainian government authority to clarify the location of hotspots in Kobachi mechanical yard (Chernobyl, Ukraine) site. Consequently, access restrictions have now be put in place for these locations.

8.3. Derivation of Survey Radiation Maps by using Karczmarz Algorithm for Data Processing

The input and output parameters for the Karczmarz algorithm applied for the current study were determined in section 7. The newly modified Karczmarz inversion algorithm coded in MATLAB considers both the ISL and energy attenuation problems. The step-by-step process that was conducted to optimize the algorithm is now discussed. Supporting graphics can be found in figures 41 to 60. Initially, this focused on Kobachi weighbridge site (Chernobyl, Ukraine) to investigate the challenges detailed at the start of this chapter. The data recorded for this specific site included multi-rotor UAV surveys conducted at altitude of 15 m, 20 m, 30 m, 40 m. The exact details of data acquisition are provided in section 7.

As a first aim, considering just the Inverse Square Law (without any airborne attenuation) the iteration number (100000 or 150000) and relaxation parameter (0.03, 0.05 or 0.08) were tested. This study used data obtained from the flight conducted at 15 m multi-rotor data because of the close proximity to the ground. Relative errors associated with various iteration number and damping factor combinations were calculated. Some representative relative error plots are shown in Figure 41.

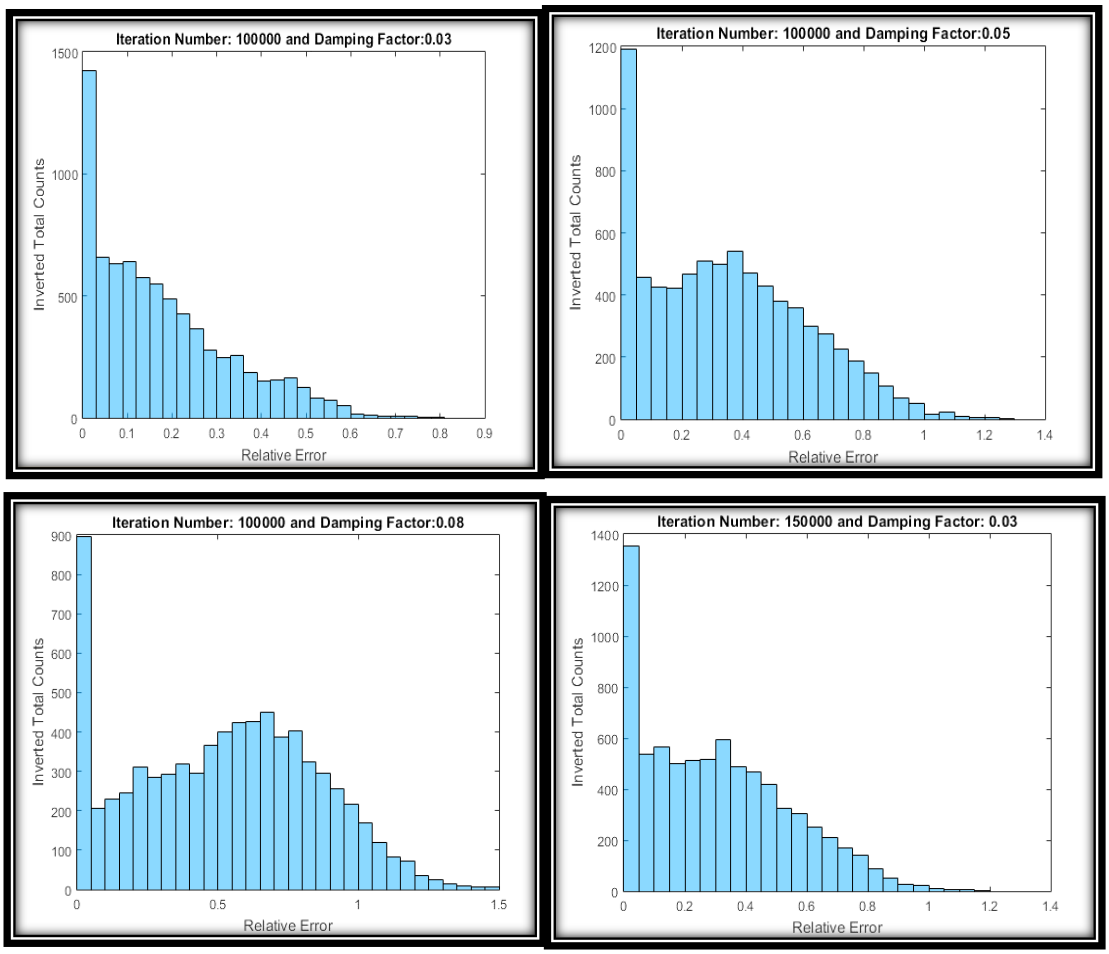

Figure 41. Histogram plots of relative errors for assessing optimum number of iterations and damping factor by using inversion algorithm based on ISL

According to the histogram plots of relative errors displayed in Figure 41, 100000 iterations and 0.03 relaxation parameter yielded the most accurate inverted total counts. These parameters were then applied for processing data obtained from each of the four altitudes at the Kobachi weighbridge site (Chernobyl, Ukraine).

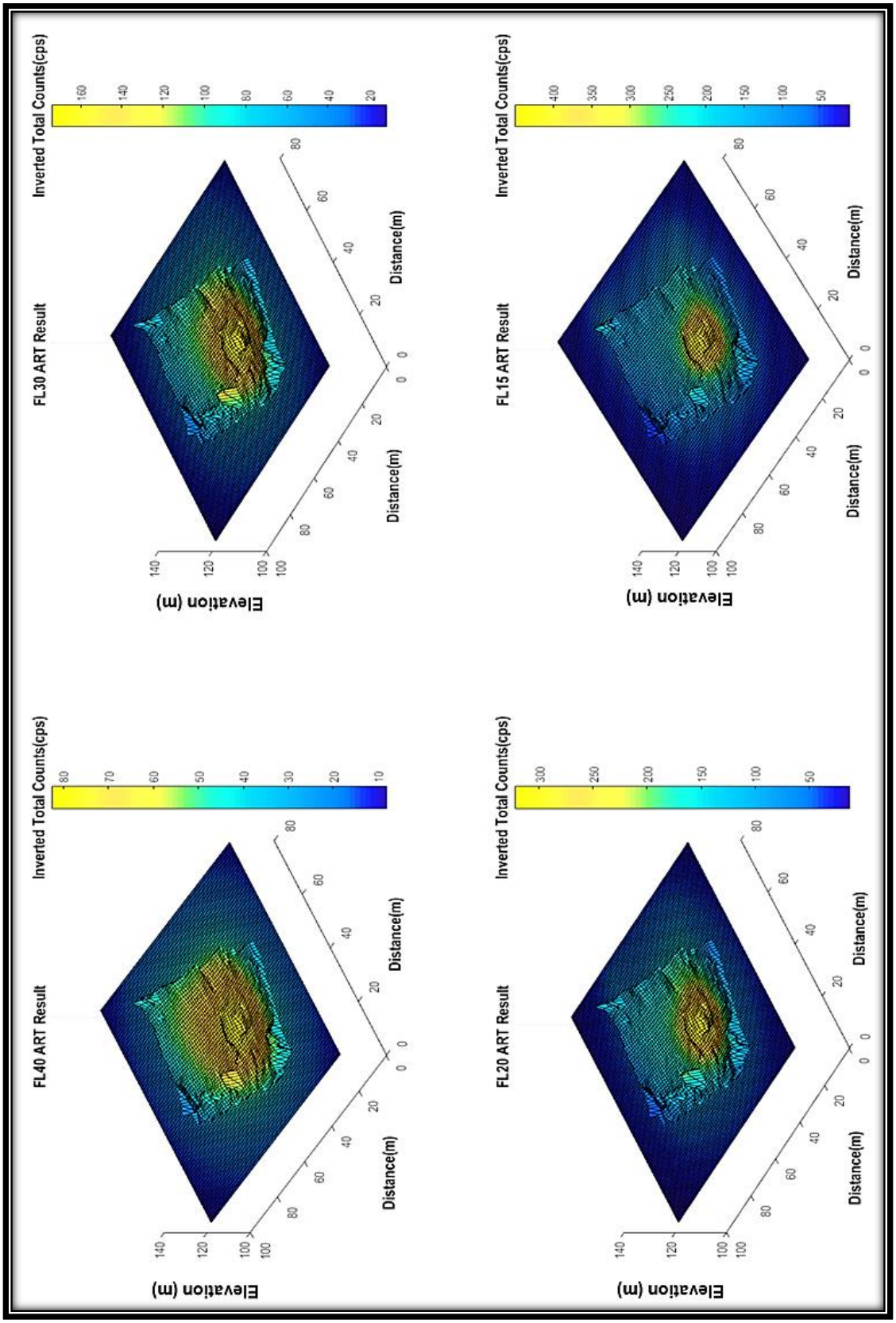

Figure 42. Inverted radiation intensity maps based on just ISL for each flight altitude

Figure 42 illustrates inverted radiation intensity maps by using ISL for 100000 iterations and relaxation parameter as 0.03. The ART result for the flight conducted at 15 m provides the best localization of the hotspot region found at the Kobachi weighbridge site (Chernobyl, Ukraine) area with peak counts of around 400 - 500 cps. It should be noted that each pixel on the radiation intensity maps is approximately ~ 3x3 metres.

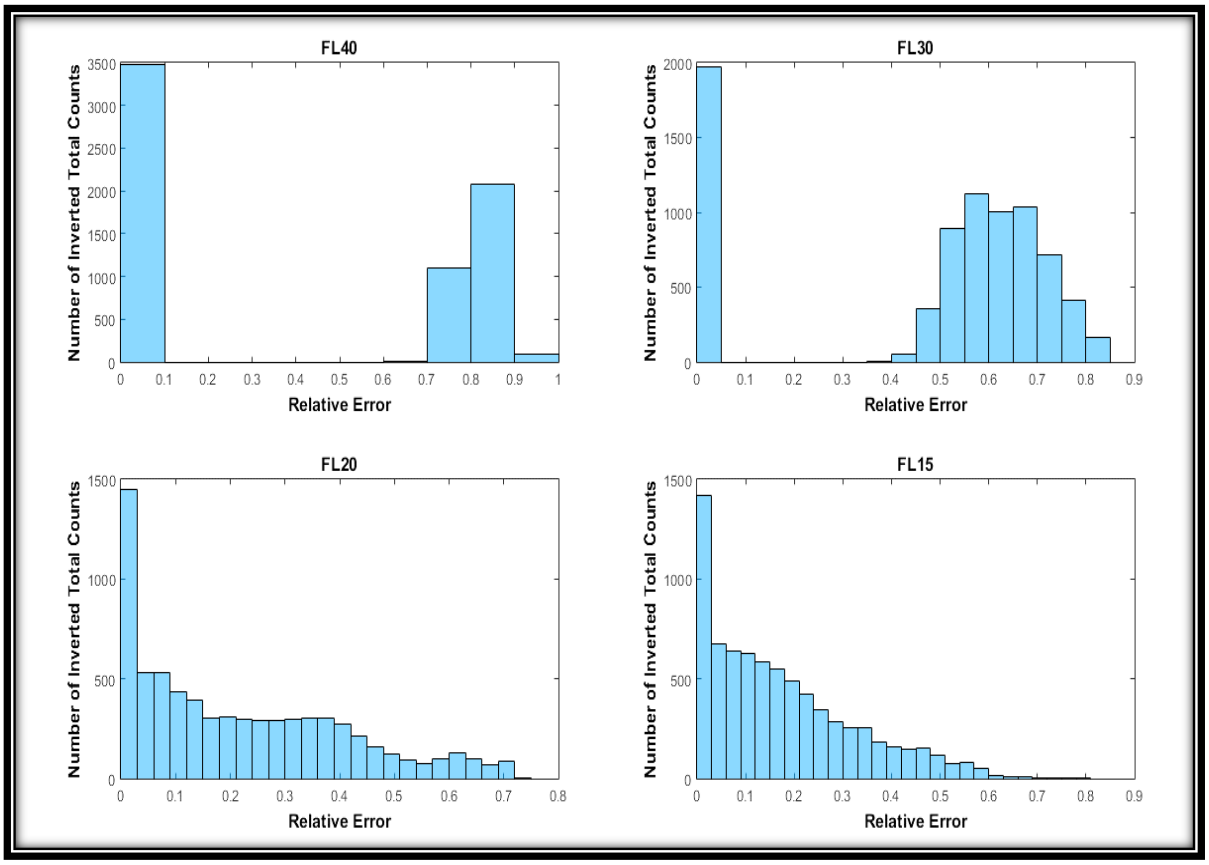

Figure 43. Histogram plots of relative errors considering just the ISL for each altitude. Top left: 40m altitude. Top right: 30m altitude. Bottom Left: 20m altitude. Bottom right: 15m altitude

When plotting the relative error values for each of the data sets from 15m to 40m altitude, it was clear that the data recorded at the highest altitude was the most unreliable as it had the biggest error. This is as expected; and equally the lowest error was recorded for the data captured at 15 m i.e. 15 m altitude survey (Figure 43). However, even for the conducted at 15 m flight altitude data set, the inversion algorithm still needs an improvement for total counts derived from UAV system.

The next step was to combine data sets from the different heights, one at a time, to see if further improvements in spatial resolution could be achieved to better localise the hot spot. Combining such data sets should increase the overall body of data whilst also providing an additional (vertical) dimension compared to single-altitude surveys (Figure 44, 45). Currently, single-altitude surveys are the international standard practice.

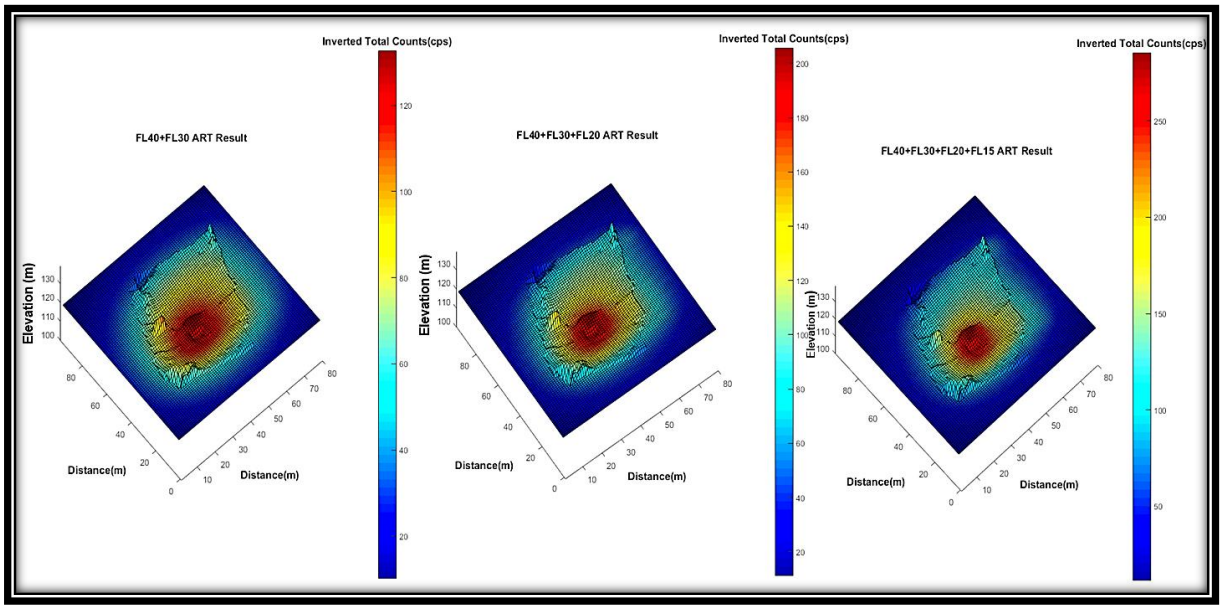

Figure 44. ART Results by using combined data sets (Flight Altitudes: 15m, 20m, 30m, 40m) considering of ISL. Top left: 40m altitude. Left: 40m altitude, 30m altitude. Middle: 40m altitude, 30m altitude, 20m altitude. Bottom right: 40m altitude, 30m altitude, 20 m, 15m altitude

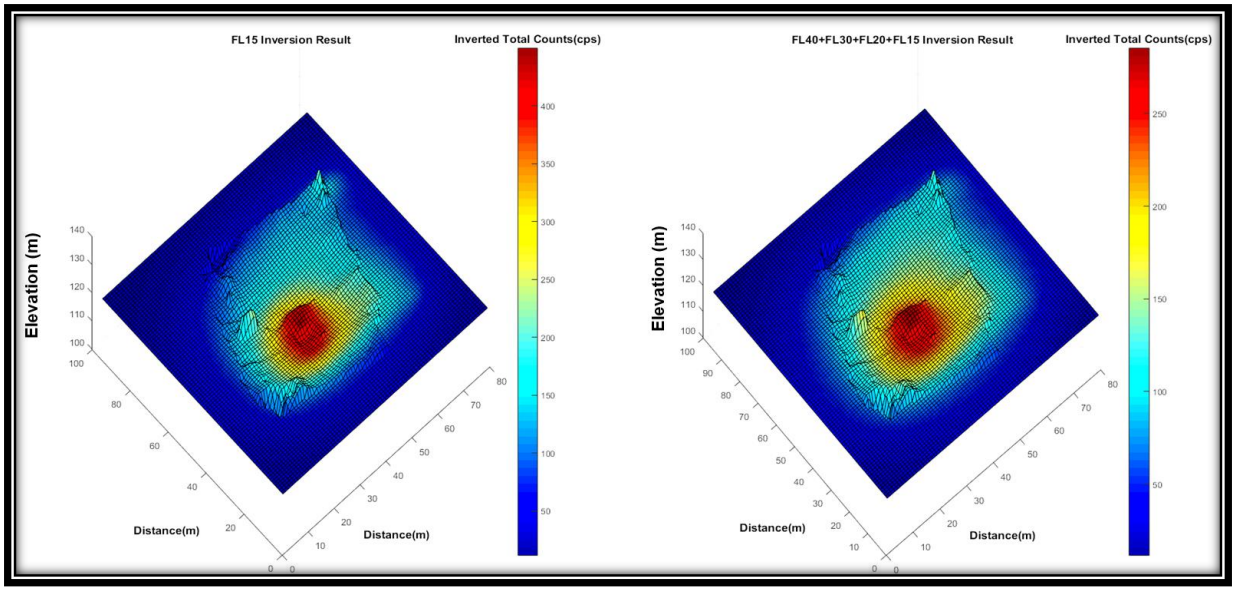

Figure 45. Comparison of inversion results (15m altitude survey versus the full compound datasets (Flight Altitudes: 15m, 20, 30 and 40m)

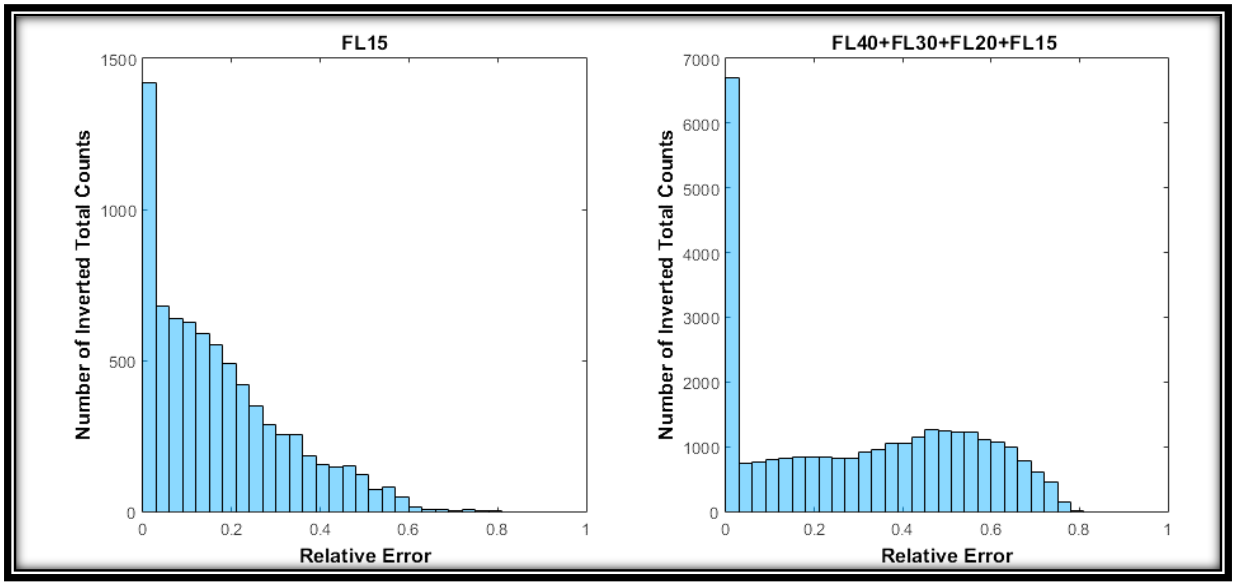

Figure 46. Histogram plots of relative errors of inverted total counts (15m altitude survey versus the full compound dataset)

Unfortunately, relative errors for the combined datasets were greater than for 15 m altitude survey but were less than for the higher altitude data sets. The total count values derived for the compound dataset did not yield the improvement in inverted total count values that was expected versus 15 m altitude survey on its own (Figure 46). We ascribe this finding, to a post-mortem discovery that the Sigma detector was experiencing signal saturation due to high local radiation levels during the survey, when passing over the

hotspot and hence these offsets the reliability of the conducted at 15 m flight altitude dataset.

The observation that the relative errors were more accurate at lower altitudes and became less accurate at higher altitudes was intriguing. It suggested that a simple ISL model was insufficient and that a second process should also be incorporated. The fact that the relative errors were larger at greater distances from the ground implied that an additional process became more pronounced with distance from the source. The attenuation of gamma photons in air (e.g. atmospheric attenuation) is such a process.

As such the second aim is to see the combined effect of ISL and atmospheric attenuation. The half-distance of Cesium photons at 662 keV, the distance over which half the initial gamma rays have survived without interacting, due to atmospheric attenuation is 72 m. This was assumed to be a suitable attenuation co-efficient. As before, the 15 m altitude data set was selected to optimize the iteration number and relaxation parameter by considering the relative errors. These results are shown in Figure 47.

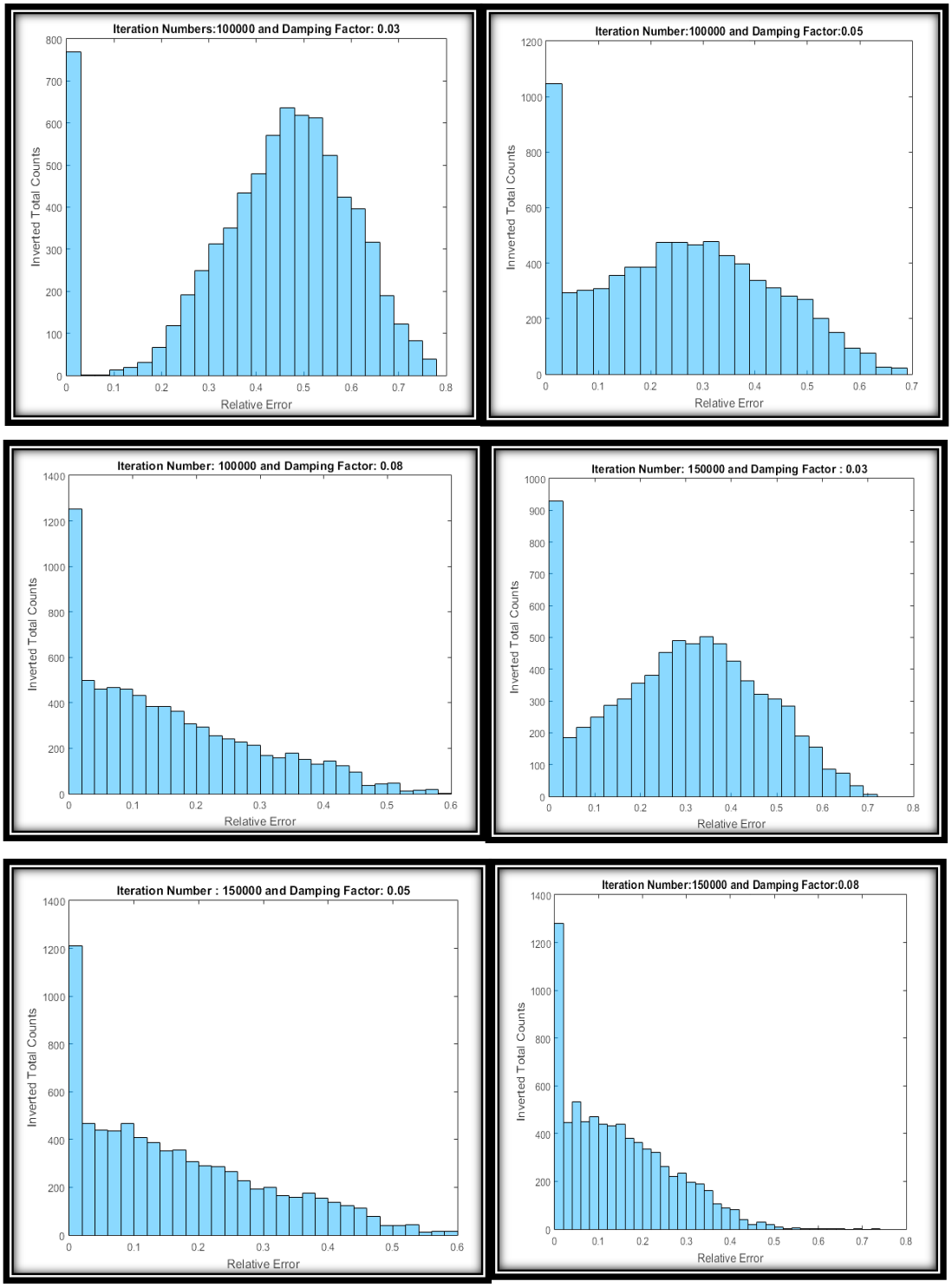

Figure 47. Histogram plots of relative errors for assessing optimum number of iterations and relaxation parameter by using inversion algorithm based on ISL and atmospheric attenuation

Allowing for atmospheric attenuation in the inversion algorithm gave more sensitive inverted total counts (Figure 49) and it converged to the solution easily. Inverted radiation intensity maps based on ISL and atmospheric attenuation for each survey altitude can be seen in Figure 48. As shown in Figure 49, the maximum relative error decreased from 0.8 to 0.6 compared to the first inversion algorithm application.

The relative errors were the lowest using 150000 iterations and a 0.05 relaxation parameter. However, the relative error obtained using 100000 iterations with a 0.08 relaxation parameter was approximately the same, but the calculation time was much shorter. Therefore, all the subsequent data from the Kobachi weighbridge site (Chernobyl, Ukraine) was processed with 100000 iterations with a 0.08 relaxation parameter.

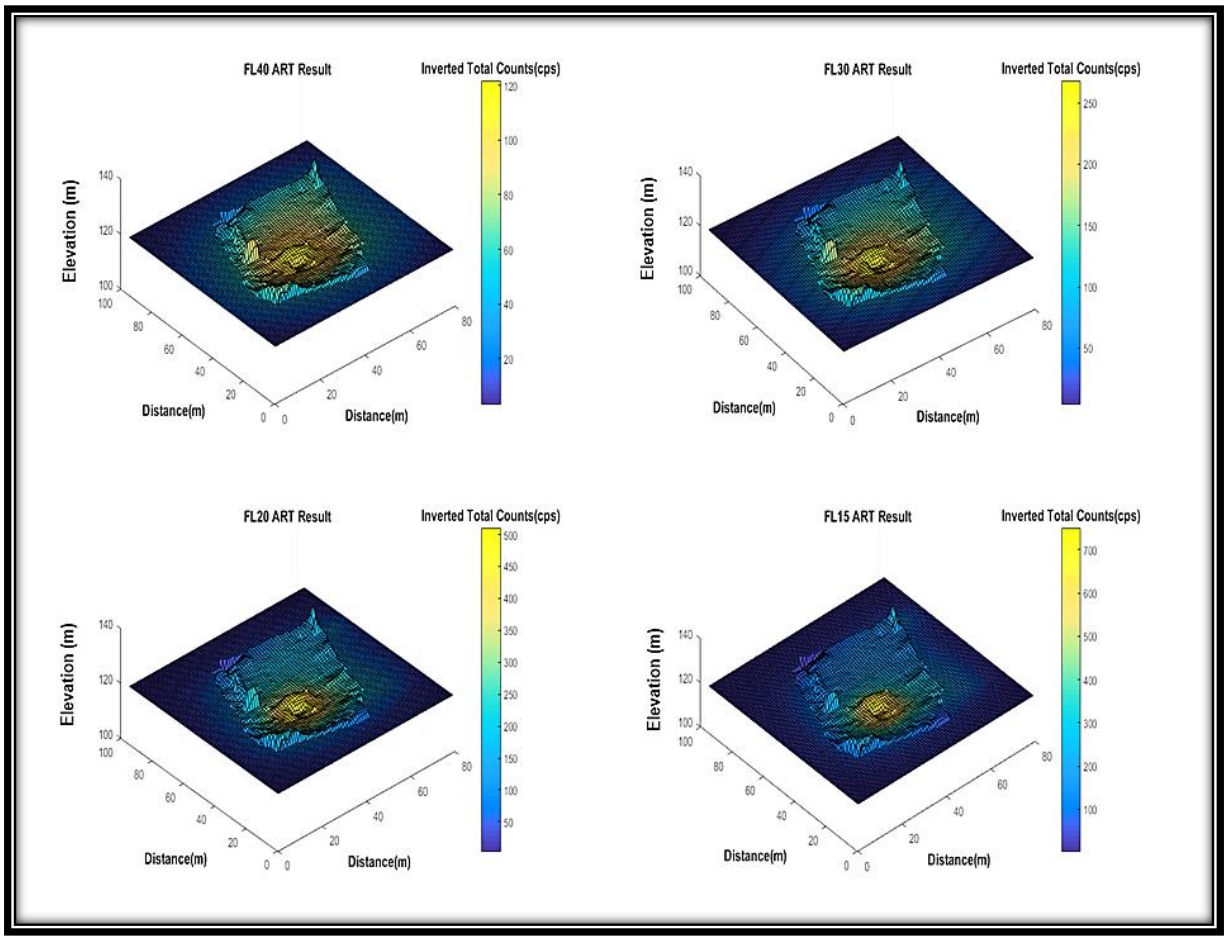

Figure 48. Inverted radiation intensity maps based on ISL and atmospheric attenuation for each survey altitude

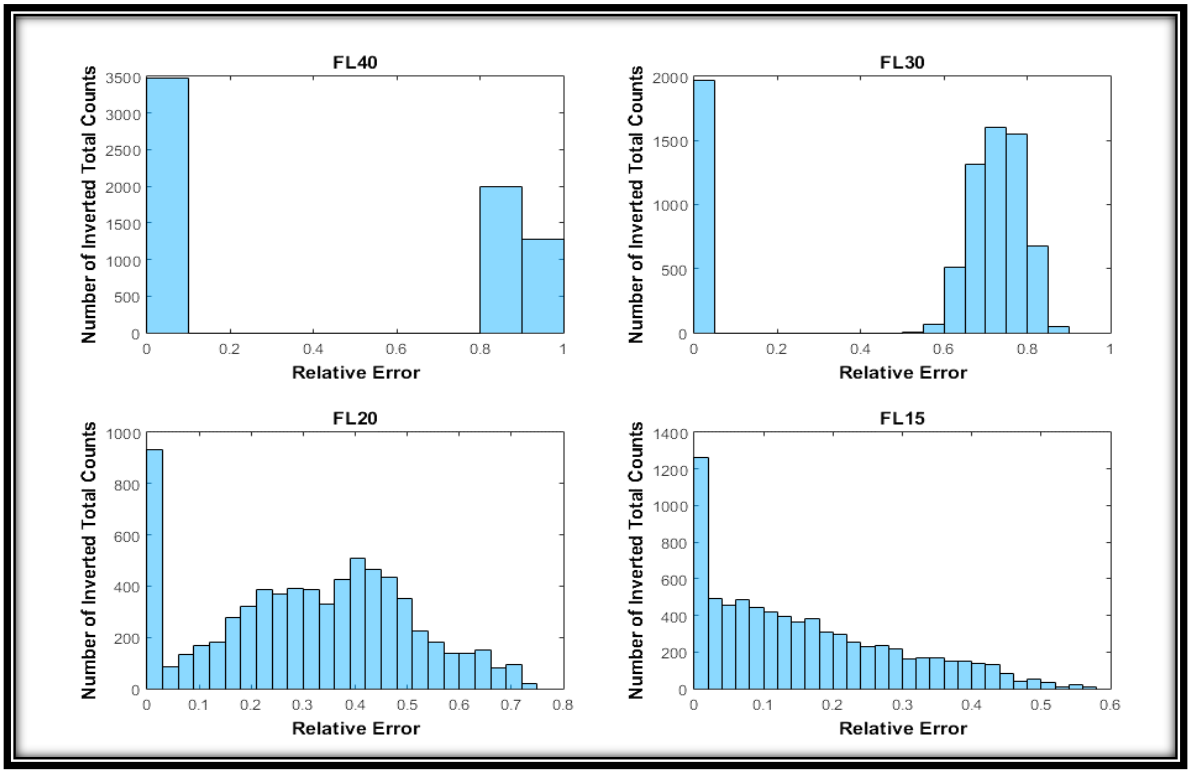

Figure 49. Histogram plots of relative errors based on ISL and atmospheric attenuation of Cesium in the air for each altitude. Top left: 40m altitude. Top right: 30m altitude. Bottom Left: 20m altitude. Bottom right: 15m altitude

ART image results obtained from combined data sets considering ISL and atmospheric attenuation of Cesium can be seen in Figure 50 and Figure 51 shows the relative errors of 15m altitude survey versus the full compound datasets.

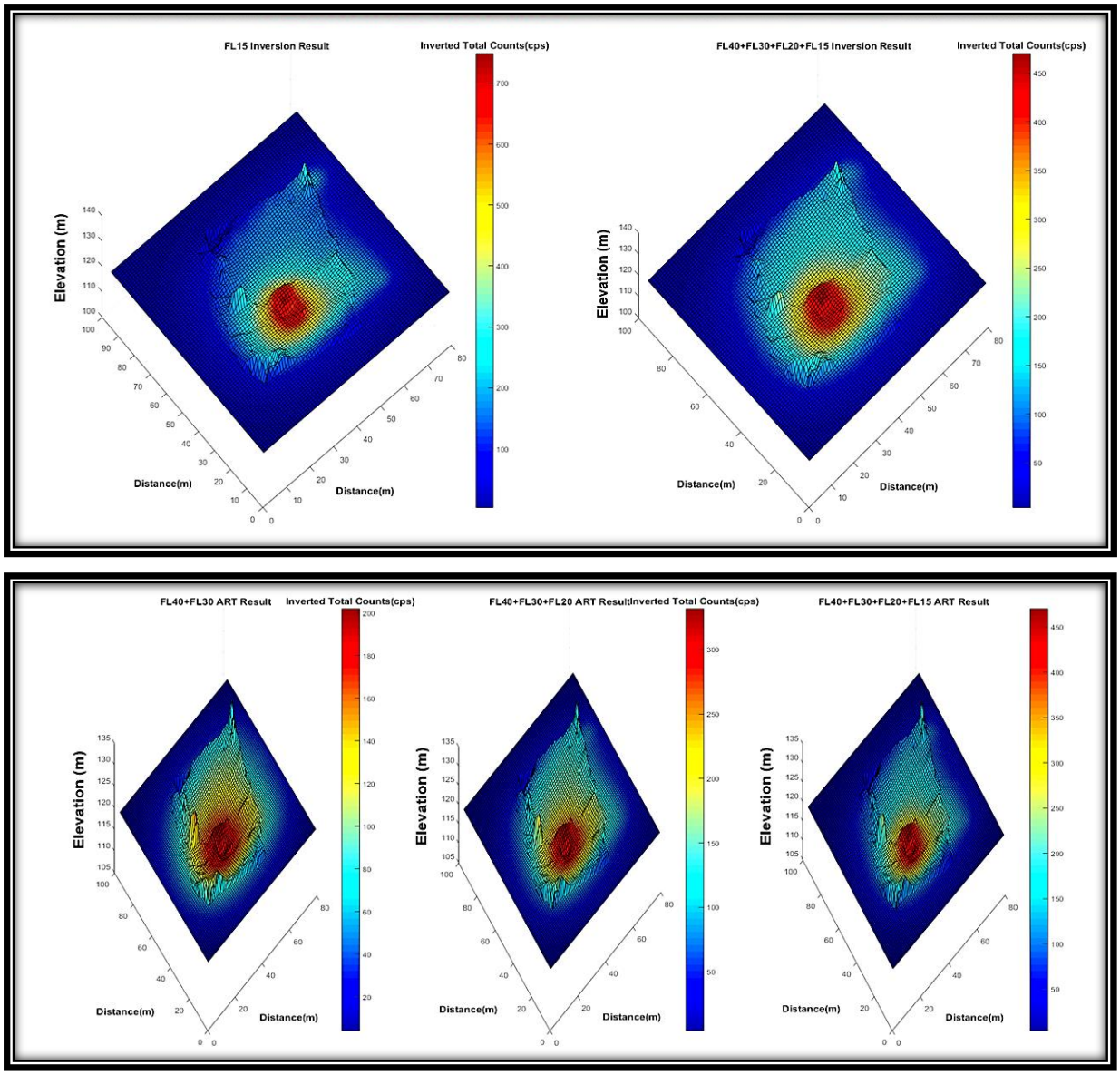

Figure 50. ART image results obtained from combined data sets considering ISL and atmospheric attenuation of Cesium. Top - Left 15m altitude, Right - 40m, 30m 20m and 15m altitude: Bottom -Left: 40m & 30m altitude. Middle: 40m, 30m & 20m altitude. Right: 40m, 30m, 20m & 15m altitude

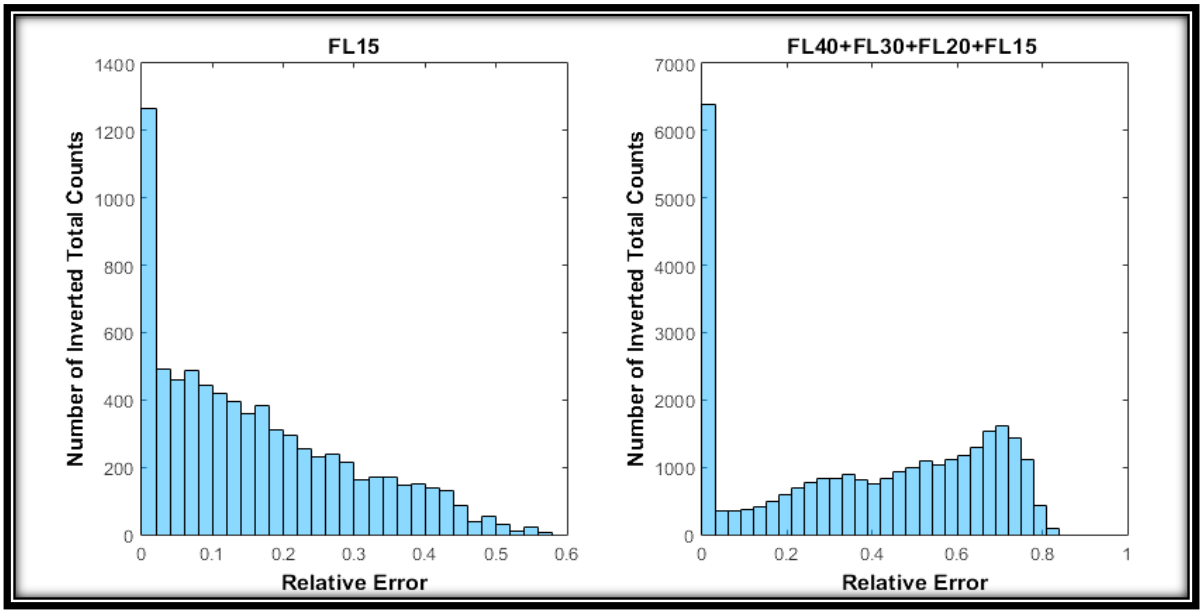

Figure 51. Comparison of inversion results (15m altitude survey versus the full compound datasets (Flight Altitudes: 15m, 20, 30 and 40m) and Histogram plots of relative errors of inverted total counts (15m altitude survey versus the full compound dataset)

In the consideration of atmospheric attenuation outlined in section 2 the attenuation coefficient was chosen based upon the cesium decay emission peak at 662keV. However, attenuation is a function of photon energy and so for any energies not 662keV the selected attenuation coefficient was incorrect. As the detector returned spectroscopic counts in the range 0.0 to 1.6 MeV, we then investigated adapting the modelled attenuation coefficient to the associated photon energy of each spectroscopic channel.

As such the model for calculating efficiency matrix (A) was adapted to consider attenuations coefficients of air for each energy. This was based upon the air density which in turn depended upon the air temperature and air pressure on the measurement day which is explained in section 6.1.2. Consequently, a new hyperspectral gamma imaging technique (HSGI) was developed. To the best of our knowledge, this is the first reported demonstration of HSGI for airborne surveys. The hyperspectral gamma imaging technique uses pixels of DTM images

HSGI was used to process results obtain the Kobachi mechanical yard (Chernobyl, Ukraine). This survey site did not have a full 3d model for the HSGI processing, so an appropriate sloped flat plane was used to approximate the 3D model. The HSGI processing requirements were too great for the laptop previously used. And so the task was conducted using a parallel processing methodology on the Bluecrystal supercomputer at the University of Bristol.

According to full inversion results, the newly developed algorithm managed to separate low energy levels from high energy levels. The interested energy levels for our research problem are between 0.61 MeV and 0.71 MeV. There is a small dark point on every energy window in Figure 52 since 15 m altitude survey data hits detector saturation which causes photo peaks to appear at lower energies which are just issue of the detector posting photon hits lower channel numbers due to signal saturation, on the other hand, the received signals are so high and out of scale in the detector.

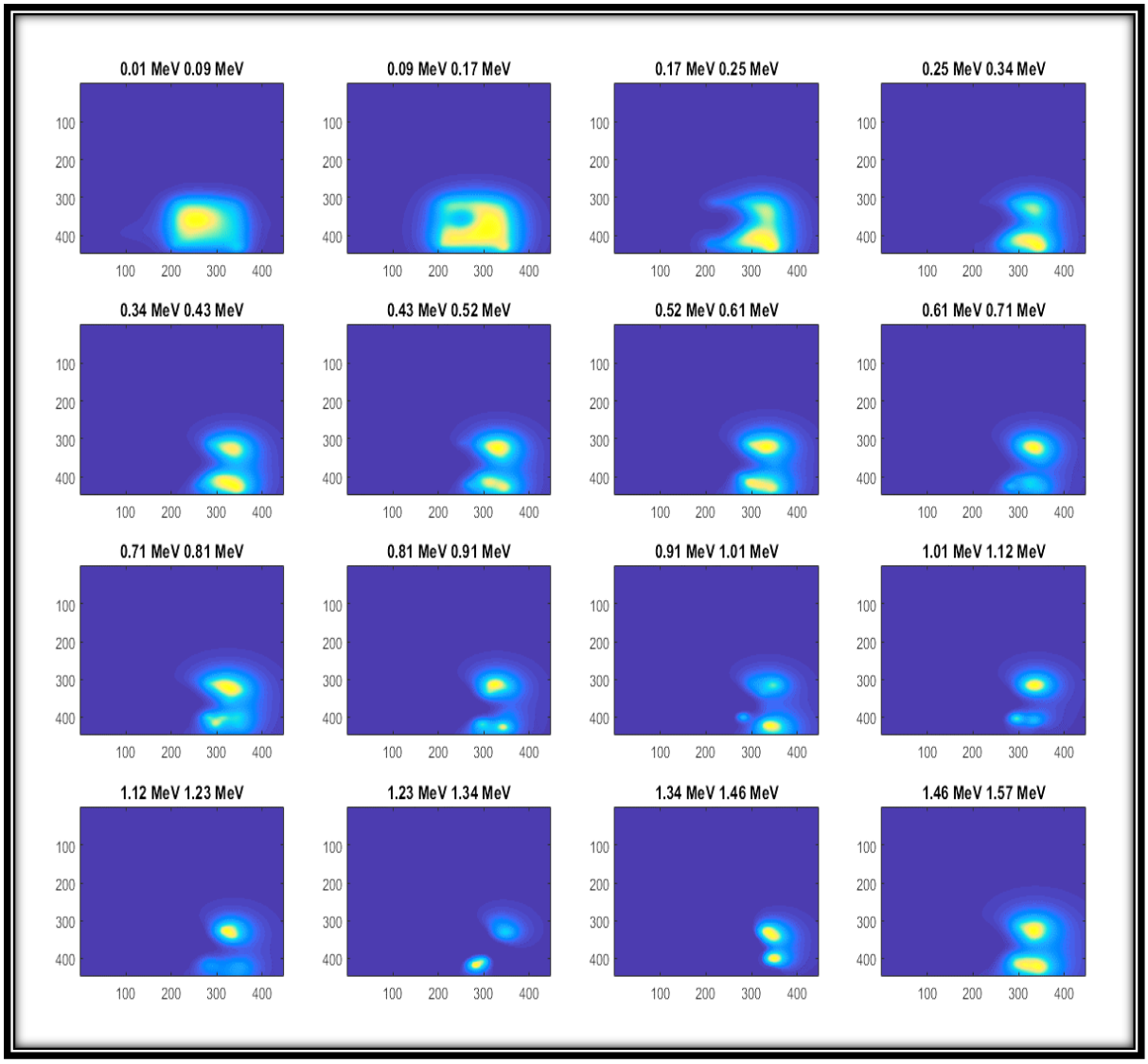

Figure 52. Full inversion results by using section 6.2 for Kobachi mechanical yard (Chernobyl, Ukraine) with the combination of multi-rotor survey and fixed-wing survey

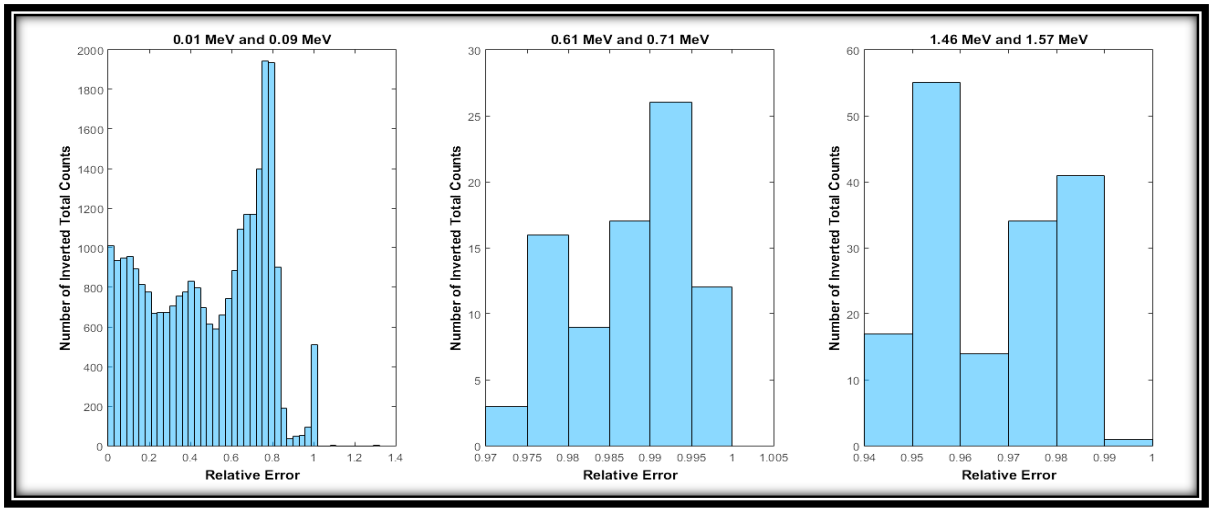

Figure 53. Histogram plots of relative errors for Kobachi mechanical yard (Chernobyl, Ukraine)

This process was repeated without 15 m data and just for fixed-wing data on Kobachi mechanical yard (Chernobyl, Ukraine) to see the changes in energies. The detector saturation effect on windows has been lost with this step (Figure 54).

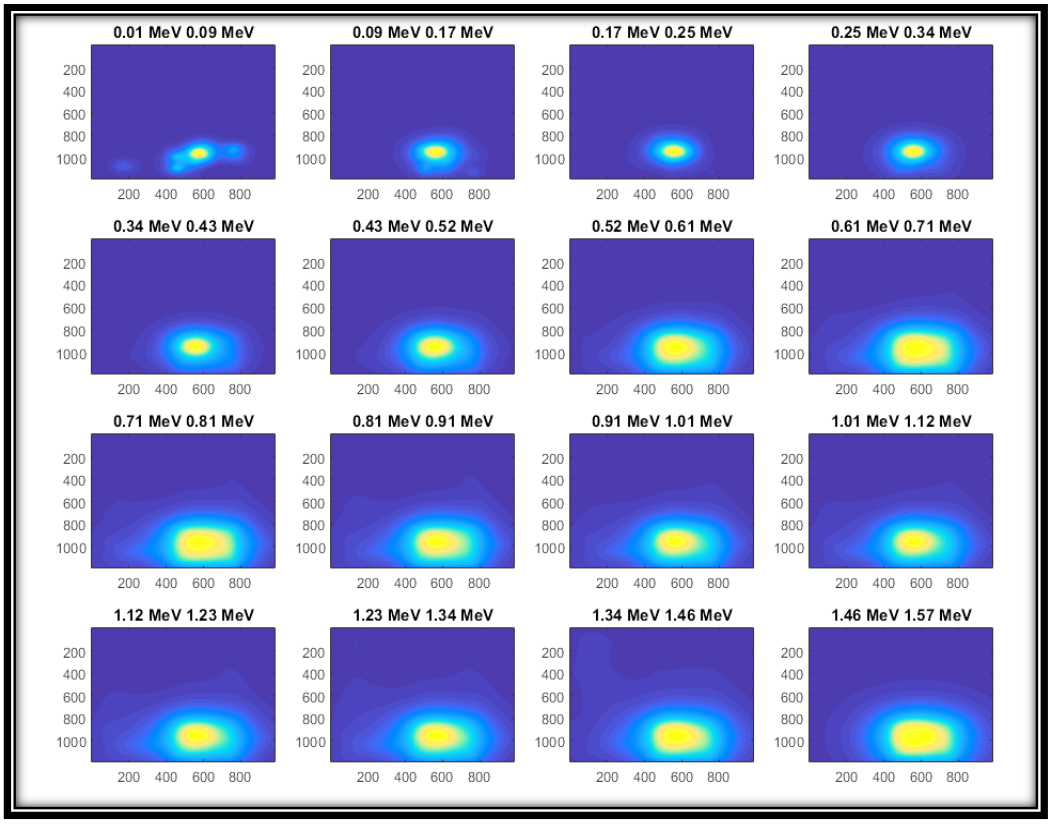

Figure 54. Full inversion results by using Section 6.2 for Kobachi mechanical yard (Chernobyl, Ukraine) without 15 m altitude survey data

Notice how at lower energies (0.01-0.09 MeV and 0.09 to 0.17 MeV) individual sources can be identified but this is not possible at higher energies. This demonstrates one of the benefits and capabilities of our newly developed HSGI approach.

9. DISCUSSION, CONCLUSIONS AND FUTURE WORK

9.1. Statistical Methodology – The Inversion Methodology (HSGI)

This work has developed a new 'inversion method' approach, with associated algorithms, for processing the raw 3D radiometric data collected during aerial surveys to generate a radiation map for 1m above the ground, which is the international standard for air dose-rate maps. The inversion algorithm was developed to provide an improved capability for localizing on-the-ground radiation sources (hot spots), thereby enhancing the spatial resolution of the arising radiation map for any combined survey dataset.

Initially a simple ISL model was implemented. However, it was apparent from studying the relative errors that this model was overly simplistic. Consequently, the model was adapted to also consider atmospheric attenuation. Initially, the atmospheric attenuation model assumed that all radiation was at 662 MeV but ultimately the atmospheric attenuation coefficients were corrected and the novel HSGI method (the inversion method) was demonstrated. An empirical formula for the calculation of energy attenuation of gamma photons in the air based upon atmospheric conditions was used to calculate the attenuation coefficients. The computationally intensive HSGI processing was conducted using the Bluecrystal supercomputer at the University of Bristol. The recovered radiation maps in this HSGI survey allowed us to identify radioactive anomalies in the recovered maps that would otherwise not have been apparent.

It is important to note, that this arising HSGI processing methodology is equally applicable to any 3D radiometric dataset, for example data that could be recorded from (I) a radiation scanning robotic arm used for waste package inspection or (II) from a radiation mapping unit attached to a ILW store gantry crane to map between waste stillages. In each example, the inversion method could be used to pin-point with good accuracy (sub-metre to 10's of centimetres), specific hot spot locations that could

represent areas of safety concern. Hence, this novel technical processing approach can be applicable in many use-case scenarios across the nuclear industry.

What is specifically very useful about the algorithm developed herein is that it can self-validate its own results, by testing the consistency of the data. To improve upon a standard interpolation algorithm for converting aerial data to a 1m radiation map, there is a need for the raw dataset to be self-consistent. Even if the dataset is not consistent; as for the Chernobyl Kobachi dataset, the output maps of the inversion processing are demonstrably still as good as the best classical interpolation methods used currently – this is an excellent default fall-back.

The sad fact is that the data recorded over Chernobyl, was proven not to be fully consistent due to detector saturation issues over the hotspots mapped. This is highlighted by the error checking capability of the algorithm and was subsequently verified when examining the raw data in detail. In most other applications scenarios, detector saturation is not considered so likely, because Chernobyl is an exceptional case in terms of the very high (mSv) levels of radioactivity.

9.2 Future Work

For the benefit of the inversion algorithm to be fully realised, it is necessary to change the way in which aerial radiometric data is collected from single-survey to multi-survey. The current international standard, as has existed for decades, is to collect a single pass grid survey in which parallel survey lines are flown at the same altitude. Data from such a single pass approach could be successfully processed using the inversion algorithm but would produce an output comparable to any standard interpolation method that accounts for air attenuation and the Inverse Square Law (geometric dilution). What is required to fully utilise the capability of the algorithm is to record radiometric data over the survey area at multiple heights. This could be the same flight lines automatically repeated over the survey area at different altitudes e.g. 5 m, 10 m and 15 m or it could be a deliberately more heterogeneous multi-height flight path, perhaps via manual piloting (Figure 55).

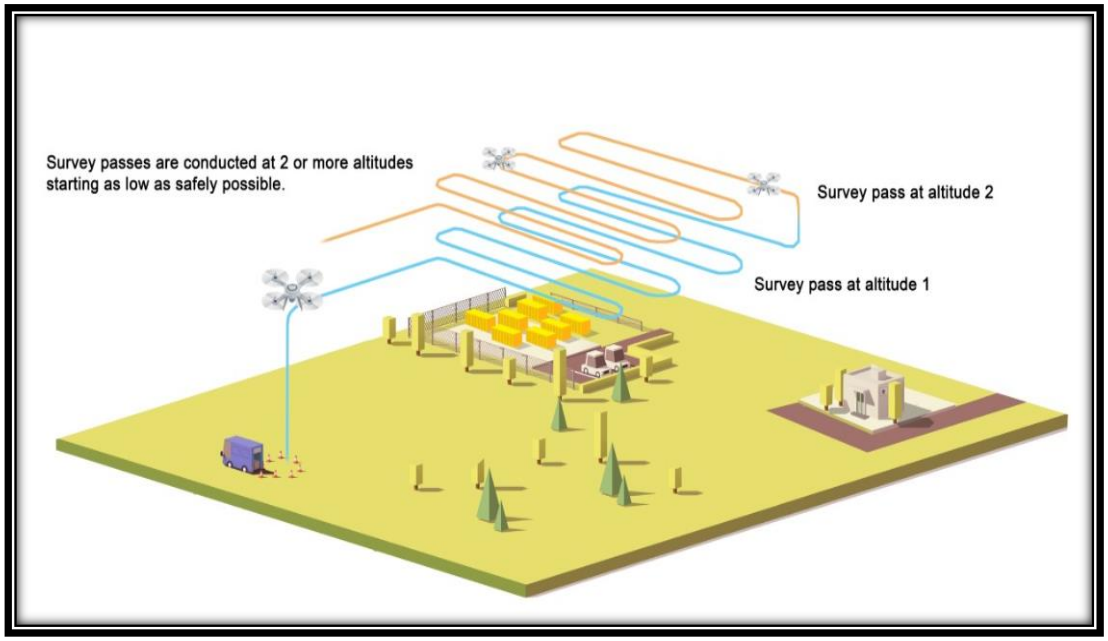

Figure 55. A depiction of the suggested multi-pass aerial radiometric survey methodology for inversion processing

A key consideration is that in all cases, the aerial data should still be collected from as close to the ground as operationally possible to minimise errors related to the ISL. For example, if a site geometry permitted survey flights as low as 5 m altitude, then it would be recommended to record a multi-pass radiometric survey at 5 m, 7 m and 10 m rather than a survey at 5 m, 15 m and 30 m. This would, from an operational perspective, reduce the amount of error in the dataset. Conversely, if the on-the-ground radiation sources were very strong, it would be advisable to fly at an altitude corresponding to the height at which the radiation detectors are not signal saturated. This was a major issue for the Chernobyl surveys which was only spotted post-survey.

The multi-pass survey methodology would also be applicable to surveys of nuclear plant and building infrastructure where radioactive sources would be located differentially within the confines of the facility (Figure 56). The proposed method for surveying buildings requires that new scan paths and directional detectors to be effective. By flying multiple passes around the building and over the building at different heights then the inversion algorithm could be used to identify any localised radiation emitters.

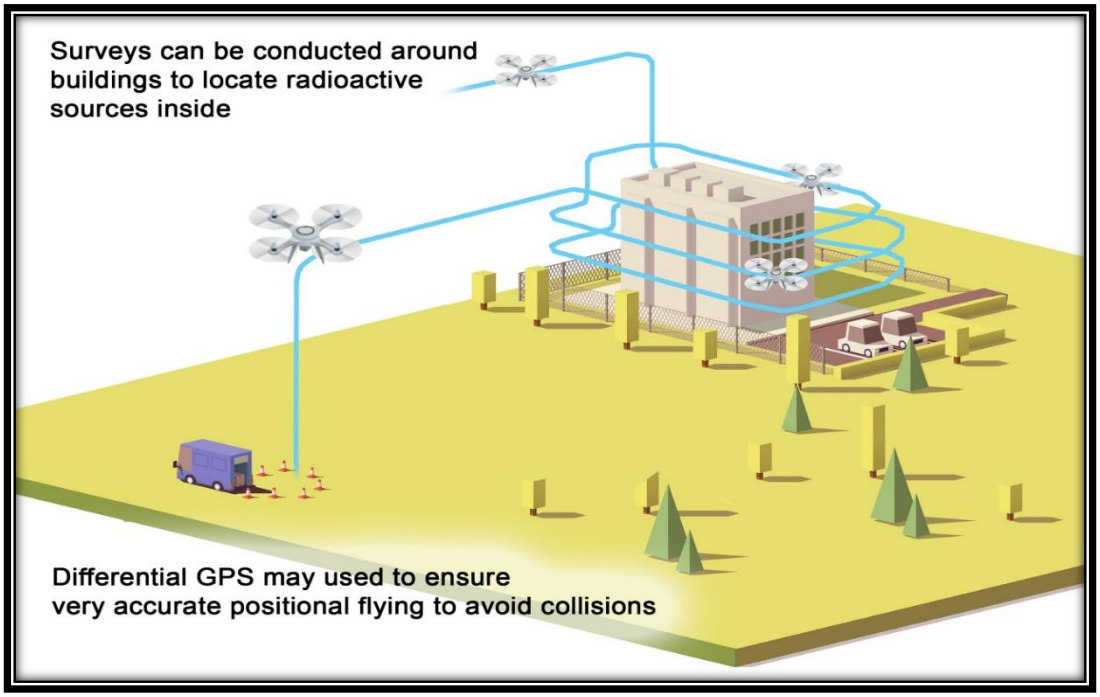

Figure 56. Multi-pass survey methodology applied to building/plant surveys

This multi-pass approach applied to buildings would require an accurate 3D model of the site area being surveyed e.g. a DEM which includes the building structures. This would be identical to the data recorded for this thesis but for one issue. The 3D model or algorithm would have to be modified to account for windows and doors (or any physical opening or substantial change in material type) which offer significantly less attenuation of the radiation attempting to escape from the inside of the building. 'Openings' would offer shine-paths for the preferential escape of gamma rays and if correctly accounted for enhancing the ability of the inversion algorithm to localise radiation emitters. This is certainly an area for future research and development.

Based on the arguments presented above, the obvious evolution of this research is to move towards inferring the location of partially shielded radiation sources. Conceptually, the inversion algorithm should be able to differentiate a strong source at depth e.g. shallow buried waste, versus a weak source over a larger area e.g. radioactive fallout. This must be experimentally verified but would have two significant applications:

1) The first is for the differentiation of surface contamination versus buried waste in the Chernobyl and Fukushima fall-out zones. This is potentially very important for the Chernobyl exclusion zone where the Ukrainian authorities are looking to repurpose areas of the zone to become solar farms. Before this can occur, the target areas need to be verified as sufficiently low radiation hazard for workers to install the solar infrastructure. This may include levelling areas of ground where there is partially buried waste - which could prove problematic without prior radiometric surveys to identify high-risk areas.

2) The second is for the translation of the UAV radiation mapping technology for the prospecting of valuable ore bodies (as per the introduction to this thesis). The ability to localise radiometric anomalies and distinguish surficial occurrences versus shallow-buried deposits would be very useful for mining companies. Understanding the 'run' of ore bodies as they move from the surface to greater subsurface depth is very important for understanding the directions in which any deposit might be mined.

A further area for improvement of this research is in making a full conversion from count intensity data (cps) maps to dose maps (μSv/hr). This requires full calibration of the gamma detectors over an applicably wide gamma energy range. Once this is achieved, including the 3D response function of the detector (directionality) the efficiency matrix (A) can be substantially enhanced, thereby enabling a more advanced application of the inversion algorithm. This could be conducted by surveying a strong, localised and well characterised source at many altitudes. This calibration could then be used to conduct real-time HSGI processing in any subsequent surveys. Specifically, the Burikivka village in the CEZ, contains radioactive waste deposits that were buried after the Chernobyl accident in unrecorded locations. The new HSGI inversion algorithm could be deployed on UAVs for real-time spatial-spectral radiological characterisation.

9.3. Final Summary and Conclusions

In summary, the current project has developed a novel statistical methodology (HSGI) for processing aerial radiometric data for site characterisation of radiation anomalies. The development of this HSGI method necessitates a change in the way future aerial gamma surveys are conducted if enhanced spatial resolution for on-the-ground radiation sources is to be achieved.

This study had the unique opportunity to record and then work with radiometric survey data collected from the Chernobyl exclusion zone, one of the most highly contaminated locations on the planet. Survey data was collected by multi-rotor, fixed-wing and backpack with a gamma ray spectrometer detector system in Ukraine.

The dual UAV approach, which is the use of newly developed fixed-wing and multirotor UAVs, never previously used around the Red Forest area for radiation scanning, managed to produce on-the-ground radiometric maps comparable with and arguably, spatially more accurate, than any previous surveys derived from manned helicopters in 1990s. Moreover, radiation anomaly maps of the Kobachi weighbridge (Chernobyl, Ukraine) and Kobachi mechanical yard (Chernobyl, Ukraine) were prepared for the first time with this survey. The most significant discovery of this research is the hotspot in Kobachi weighbridge survey site, which has never identified. This is caused by a highly contaminated steel structure with count levels. Moreover, there is a significant localised variation in radioactivity, ascribed primarily to partial and inconsistently distributed burial of mixed radioactive wastes. Finally, the greatest innovation in this research project is the novel HSGI technique that can be adopted in real-time measurements and will help the identification of radioisotopes in future fallouts spreads.

Future work will seek to further develop the HSGI algorithm and record strong new datasets, which can more substantially prove the benefits of using this advanced methodology for radiation mapping. Not only is such an approach more accurate but it also can prove results in near-real time. This would be immensely desirable to first responders to any future nuclear incidents worldwide.

10. References

Allison J.W., 1958, Gamma-Radiation Absorption Coefficients of Air in the Energy Range 0.01 to 100 MeV, Journal of Applied Physics, 29, 1175.

Amara M., Bendaoud A., Tsunogae T., Moahmed A., Dufrechou G., Jessell M., Hamoudi M. and Boubekri H., 2018, Structural Behaviour of the Tefedest terrane (Central Hoggar, Algeria) insight from airborne magnetic data and 3D magnetic inversion, The 13th SEGJ International Symposium.

Ameglio L., 2018, Review of Developments in Airborne Geophysics and Geomatics to Map Variability of Soil Properties, 14. International Conference on Precision Agriculture, Canada.

Anderson D., Craven M. J., Dzur R., Briggs T.; Lee D. J, Miller E., Schultz E., Vigil S., 2018, Using Unmanned Aerial Systems to Collect Hyperspectral Imagery and Digital Elevation Models at A Legacy Underground Nuclear Explosion Test Site, Image Sensing Technologies: Materials, Devices and Applications, 1065605 .

Aydin I., Aydoğan M. S., Oksum E., Koçak *A.,* An attempt to use aerial gamma-ray spectrometry results in petrochemical assessments of the volcanic and plutonic associations of Central Anatolia (Turkey), 2006, Geophysical Journal International, Volume 167, Issue 2, November 2006, Pages 1044–1052.

Barzilov A., Hartman J., Novikov I., 2016, Remote Sensing of Neutron and Gamma Radiation using Aerial Unmanned Autonomous Sytems, , Graduate & Professional Student Association University of Nevada, Las Vegas.

Bayes T., Price M.,1763, An Essay towards Solving a Problem in the Doctrine of Chance, Philosophical Transcations of the Royal Socety of London, 53, pp. 370-418.

Beresford N.A, Fesenko S.Konoplev A., Skuterud L. , Smith J.T.,Voig G., 2016, Thirty Years After the Chernobyl Accident: What Lessons Have We Learnt?, Journal of Environmental Radioactivity, 157, pp. 77-89.

Bierwirth, P. N., P. E. Gessler, and D. McKane, 1996, Empirical Investigation of Airborne Gamma-ray Images as an Indicator of Soil Properties - Wagga Wagga, NSW, In 8th Australasian Remote Sensing Conference Proceedings, Canberra, pp. 81-89.

Bierwirth P. N., Aspin S. J. Ryan P. J., and McKenzie N. J., 1997, Gamma-ray Remote Sensing of Soil Properties in a Forested Area near Batlow, NSW, Proceedings of the Third International Airborne Remote Sensing Conference and Exhibition, Copenhagen, Denmark.

Beamish D., 2014, Environmental Radioactivity İn The UK: Airborne Geophysical View of Dose Rate Estimates, Journal of Environmental Radioacitivity, 138, pp. 249-263.

Beckett K. A., 2003, Airborne Geophysics Applied to Groundwater Modelling, Advances in Regolith, pp. 8-10.

Brennan S. M., Mielke A. M., and Torney D. C., 2005, Radioactive Source Detection by Sensor Networks, IEEE Transactions on Nuclear Science, 52 (3), pp. 813–819.

Broome, H.J., Carson, J.M., Grant, J.A., Ford, K.L., 1987, A Modified Ternary Radioelement Mapping Technique and Its Application to the South Coast Of Newfoundland, Geological Survey of Canada, Paper 87-14, pp. 31-45.

Bogatov S., Manzy N., Pugachec A., Tkachenko S., Shvedov A., 2013, Emergency Radiation Survey Device on Board the UAV, International Archives of the Photogrammetry, Remote Sensing and Spatial Information Sciences, XL-1/W2.

Bollhöfer A.F. , Pfitzner K., Ryan B., Martin P., 2008, Airborne Gamma Survey of the Historic Sleisbeck Mine Area In The Northern Territory, Australia, and its use for site rehabilitation planning, Journal of Environmental Radioactivity, 99 (11), pp. 1770-4

Burtniak V., Zabulonov Y., M. Stokolos M., Bulavin L., 2017, The Remote Radiation Monitoring of Highly Radioactive Sports in the Chernobyl Exclusion Zone, Journal of Intelligent and Robotic Systems, 90 (6).

Burns P. and Finch R., 1999, Uranium: Mineralogy, Geochemistry, and the Environment, Mineral Society of America, Volume 38, ISBN 0-939950-50-2; ISBN13 78-0-939950-50-8.

Briechle S., Sizov A., Tretyak O., Antropov V., Molitor N., Krzystek P., 2018, UAV-Based Detection of Unknown Radioactive Biomass Deposits In Chernobyl's Exclusion Zone, ISPRS - International Archives of the Photogrammetry, Remote Sensing and Spatial Information Sciences, XLII-2, pp. 163-169.

Cenker, C., Feichtinger, H.G., Mayer, M., Steier, H., Strohmer, T., 1992, New variants of the POCS method using affine subspaces of finite codimension, with applications to irregular sampling, In: Proc. SPIE: Visual Communications and Image Processing, pp. 299–310 .

Censor Y., Herman G.T., Jiang M., 2009, A Note on the Behaviour of the Randomized Kaczmarz Algorithm of Strohmer and Vershynin, J Fourier Anal Appl. , 15(4), pp. 431-436.

Cerrito L., 2017, Radiation and Detectors, Introduction to the Physics of Radiation and Detection Devices, Springer.

Chein-I Chang, 2013, Hyperspectral Imaging: Techniques for Spectral Detection and Classification, 1, Springer Science & Business Media

Cinar H., Altundas S., Celik N. and Maden N., 2017, In-situ Gamma Measurements for Deciphering Radioactivity Level in Sarihan Pluton Area of Northeastern Turkey, Arabian Journal of Geosciences, 10, 435.

Cresswell, A.J., and Sanderson, D.C.W., 2012, Evaluating Airborne And Ground Based Gamma Spectrometry Methods for Detecting Particulate Radioactivity In The Environment: A Case Study Of Irish Sea Beaches, Science of the Total Environment, 437, pp. 285-296.

Connor D.T., Martin P.G., Smith N.T., Payne L., Hutson C., Payton O.D., 2017, Yamashiki Y., Scott T.B., Application of Airborne Photogrammetry for the Visualisation and Assessment of Contamination Migration Arising from A Fukushima Waste Storage Facility, Environmental Pollution, 234 , pp. 610-619.

Connor, D., Martin, P.G., Smith, N.T., Payne, L., Hutson, C., Payton, O.D., Yamashiki Y. and Scott, T.B., 2018, Application Of Airborne Photogrammetry for the Visualisation and Assessment of Contamination Migration Arising from A Fukushima Waste Storage Facility, Environmental Pollution, 234, pp. 610-619.

Connor, D., Martin P.G., W. Keiran, Verbelen Y., Goren S., Smith N. T., Scott T.B., 2019, A Multi-Scale Unmanned Aerial Vehicle (UAV) Approach For Rapid Response To Radiological Emissions from Nuclear Incidents, Proceedings of FDR2019, Fukushima, Japan.

Connor D., 2016, There dimensional radiation mapping using photogrammetry as a tool for the characterization of low-level radiation anomalies associated with legacy industrial sites, Earth Science Research Project, University of Bristol.

Connor, D. T., Martin, P. G., & Scott, T. B., 2016, Airborne radiation mapping: overview and application of current and future aerial systems. International Journal of Remote Sensing, 37(24), pp. 5953-5987.

Dai L., Schon T., 2015, On the Exponential Convergence of the Kaczmarz Algorithm, IEEE Signal Processing Letters, 22(10) .

Dayker A., 1987, 2013, The Soviet Union under Gorbachev Prospects for Reform, Routledge Revials, NewYork.

Dess B. W., Kroutil R. T., Small G. W., 2019, Background Correction Method for improving the Automated Detection of Radioisotopes from Airborne Gamma-Ray Surveys, Journal of Environmental Radioactivity, 198, pp. 104-116.

Dickson B.L., and Scott K. M., 1997, Interpretation of Aerial Gamma-ray Surveys - Adding the Geochemical Factors, AGSO Journal of Australian Geology and Geophysics, 17 (2), pp. 187 - 200.

Dong J. Xiao X., Sheldon S., Biradar C., Zhang G., Duong N.D., Hazarika M., Wikantika K., Takeuhci W., Moore B, 2014, A 50-M Forest Cover Map in Southeast Asia From ALOS/PALSAR and Its Application on Forest Fragmentation Assessment, PLoS ONE, 9.

Druker E., 2017, Airborne gamma-ray spectrometry data processing using 1.5D inversion, Journal of Environmental Radioactivity, 177, pp. 13-23.

Duda, R. O. and P. E. Hart, 1972, Use of the Hough Transformation to Detect Lines and Curves in Pictures, Comm. ACM, 15, pp. 11–15 .

D'Auria S., 2018, Introduction to Nuclear and Particle Physics, Springer.

Egmond F.M. V., Veeke S. V. D., Knotters M., Koomans R.L., Walvoort D.J.J. and Limburg J., 2018, Mapping Soil Texture with A Gamma-Ray Spectrometer: Comparison Between UAV and Proximal Measurements and Traditional Sampling, Research Project.

Erdi K. G. , Matolin M. , Minty B. , Nicolet J., Redford W.S. , Schetselaar E.M, 2003, Guidelines for Radioelement Mapping Using Gamma Ray Spectrometry Data, International Atomic Energy Agency.

Falciglia P.P. , Biondi L. , Catalano R. , Immè G. , Romano S. , VAGLiasindi F.G. , 2017, Preliminary Investigation for Quali-Quantitative Characterization of Soils Contaminated with ^{241}Am and ^{152}Eu by Low-Altitude Unmanned Aerial Vehicles (UAVs) Equipped with Small Size Γ-Ray Spectrometer: Detection Efficiency And Minimum Detectable Activity (MDA) Concentration Assessment, Journal of Soils Sediments, pp. 1-11.

Fortin R., Hovgaard J., M.Bates, 2017, Airborne Gamma Spectrometry in 2017: Solid Ground for New Development, Proceeding: Sixth Decennial International Conference on Mineral Exploration, pp. 129-138.

Furutani, T., K. Uehara, K. Tanji, M. Usami, and T. Asano.,2015, A Study on Micro-Scale Airborne Radiation Moni-toring by Unmanned Aerial Vehicle for Rural Area Reform Contaminated by Radiation, 1, pp. 1–9.

Gabrlik P., Lazna T. ,2018, Simulation of Gamma Radiation Mapping Using an Unmanned Aerial System, IFAC PapersOnLine, 51 (6), pp. 256–262.

Galántai A.,2004, Projectors and Projection Methods, Advances in Mathematics, Kluwer Academic, London, UK.

Gatis N., Luscombe D.J., Carless D., Parry L.E., Fyfe R.M. Harrod T.R., Brazier R.E., Anderson K., 2019, Mapping Upland Peat Depth Using Airborne Radiometric and Lidar Survey Data, Geoderma, 335, pp. 78-87.

Grahn H., Geladi P., 2007, Techniques and Applications of Hyperspectral Image Analysis, John Wiley & Sons.

Gordon R., Bender R., Herman G., 1970, Algebraic Reconstruction Techniques (ART) for Three Dimensional Electron Microscopy and X-Ray Photography, Journal of Theoretical Biology, 29 (3), pp. 471–481.

Gordon R., 2011, Stop Breast Cancer Now! Imagining Imaging Pathways towards Search, Destroy, Cure and Watchful Waiting Of Premetastasis Breast Cancer, In: Breast Cancer - A Lobar Disease, Springer, pp. 167–203.

Grasty, R.L., and Minty, B.R.S., 1995, A Guide To the Technical Specifications for Airborne Gamma-ray Surveys, Australian Geological Survey Organisation, 60, pp. 89.

Geiger H. M., Muller W., 1928, Electron Counting Tube for Measurement of Weakest Radioactivities, Die Naturwissenschaften (in German), **16** (31), pp. 617–618.

Grasty, R.L., Mellander, H., and Parker M., 1991, Airborne Gamma-Ray Spectrometer Surveying: International Atomic Energy Agency, Technical Report Series 323, Vienna, pp. 97.

Grimes R. W. and Nuttall W. J., 2010, Generating the Option of a Two-Stage Nuclear Renaissance, Science, 329, pp. 799-803.

Grodstein, G., 1957a, X-Ray Attenuation Coefficients from 10 Kev to 100 Mev, NBS Circular, 583.

Grodstein, G. W., 1957b, X-Ray Attenuation Coefficients from 100 Kev to 100 Mev, National Bureau of Standards Circular, 583 (583), pp. 1–58.

Gotway C.A., Ferguson R.B., Hergert G.W. and Peterson T.A., 1996, Comparisons of kriging and inversedistance methods for mapping soil parameters, Soil Science Society of America Journal, 60, pp. 1237-1247.

Gunatilaka, A., B. Ristic, and R. Gailis, 2007, On Localisation of a Radiological Point Source in 2007 Information, Decision and Control, IEEE, pp. 236–241.

Guss P., McCall K., Malchow R., Fischer R., Lukens M., Adan M., Park K., Abbott R., Howard M., Wagner E., Trainham C. P., Luke T., Mukhopadhyay S., Oh P., Brahmbhatt P., Henderson E., Han J., Huang J., Huang C., Daniels Jon, 2017, Small Unmanned Aircraft System For

Remote Contouring Mapping of A Nuclear Radiation Field, Proc. of SPIE, Radiation Detectors in Medicine, Industry, and National Security XVIII, 10393.

Haldar S., 2013, Mineral Exploration: Principles and Applications, Second Edition, Elsiever, Amsterdam, Netherlands.

Hanson G., Langmuir H. C. ,1977, Modelling of major elements in mantle-melt systems using trace element approaches, Geochimica et Cosmochimica Acta, 42, pp. 725-741.

Hatch M., 2016, Environmental Geophysics: Using Drones to Create Base Maps, 185, pp. 31-32.

Hatch M., 2017, Environmental Geophysics: Developments in Miniaturisation Technology, 189, pp. 32-33.

Herman G., 2009, Fundamentals of Computerized Tomography: Image Reconstruction from Projection, Second Edition, Springer.

Hofsetter K. J., 1994, Environmental Radiation Monitoring Technology: Capabilities and Needs, Nuclear Instruments and Methods in Physics Research, 353, pp. 472-476.

Howse J. W., L. O. Ticknor and Muske K. R., 2001, Least Squares Estimation Techniques for Position Tracking of Radioactive Sources, Automatica, 37 (11), pp. 1727–1737.

Hounsfield G.N,1973, Computerized Transverse Axıal Scannıng (tomography) , Journal of Radiology,46, pp. 1016-1022.

Hultquist C., Cervone G., 2018, Citizens Monitoring During Hazards: Validation of Fukushima Radiation Measurements, , GeoJournal, 83, pp. 189-206.

IAEA, 1979, Technical Report Series: 186, Gamma Ray Surveys.

IAEA, 1991, Chapter 2, Atoms and Radiation.

IAEA, 1995, Atomic and Molecular Data for Radiotherapy and Radiation Research.

IAEA, 2003, Guidelines for Radioelement Mapping Using Gamma Ray Spectrometry Data.

IAEA, 2015, Incident and Tracking Database (IDTB)

IAEA, 1980, Significance of Mineralogy in the Development of Flowsheet for processing Uranium Ores, Technical Reports Series, 92-0145080X, 196.

Kaczmarz S., 1937, Angenäherte Auflösung von Systemen Linearer, Gleichungen, Bulletin International de l'Académie Polonaise des Sciences et des Lettres. Classe des Sciences Mathématiques et Naturelles. Série A, Sciences Mathématiques, 35, pp. 355–357.

Kaiser M., Aziz A., Ghieth M. B., 2014, Environmental Hazards and Distribution of Radioactive Black Sand Along the Rosetta Coastal Zone in Egypt Using Airborne Spectrometric and Remote sensing data, Journal of Environmental Radioactivity, 137, pp. 71-78.

Karlsson, S., Mellander, H., Lindgren, J., Finck, R., Lauritzen, B., 2000, RESUME 99, Rapid Environmental Surveying Using Mobile Equipment, Report from the NKS/BOK-1.2 Project Group Mobile Measurements and Measurement Strategies, NKS-15, Nordic Nuclear Safety Research Secretariat, pp. 78.

Kashparov V., Levchuk S., Zhurba M., Protsak V., Khomutinin Y., Beresford N. and Chaplow J.S., 2018, Spatial datasets of radionuclide contamination in the Ukrainian Chernobyl Exclusion Zone, Earth Syst. Sci. Data, 10, pp. 339–353.

Keatley, A.C., Martin, P.G., Hallam, K.R., Payton, O.D., Awbery, R., Scott, T.B., Carvalho, F., Oliveira, J. M. & Malta, M., 2018, Source Identification of Uranium-Containing Materials at Mine Legacy Sites in Portugal, Journal of Environmental Radioactivity, 183, pp. 102-111.

Killeen P.G., Mwenifumbo C. J. and Ford K.L., 2015, Tools and Techniques: Radiometric Methods, Treatise on Geophysics, pp. 447-524.

Kinoshita N., Sueki K., Sasa K., Kitagawa J., Ikarashi S., Nishimura T., Ying-Shee W., Satou Y., Handa K., Takahashi T., Sato Masanori., Yamagata T., 2011, Assessment of Individual Radionuclide Distributions from the Fukushima Nuclear Accident Covering Central-East Japan, PNAS , 108 (49), pp. 19526-19529.

Klooster V. D., Egmond V., Sonneveld F.M., 2011, Mapping Soil Clay Contents in Dutch Marine Districts Using Gamma-Ray Spectroscopy, European Journal of Soil Science 62, pp. 743- 753.

Knoll, G. F., 2010, Radiation Detection and Measurement. John Wiley & Sons.

Koch L., 2000, Transuranium Elements, in Ullmann's Encyclopedia of Industrial Chemistry, Wiley

Konoplev, A.V., Bulgakov, A.A., Popov, V.E., Popov, O.F., Scherbak, A.V., Shveikin, Yu.V., and Hoffman, F.O., 1996, Model Testing using Chernobyl Data: I. Wash-Off Of ^{90}Sr and ^{137}Cs from Two Experimental Plots Established in The Vicinity of Chernobyl Reactor, Health Physics, 70(1), pp. 8-12.

Konoplev, A.V., Bulgakov, A.A., Hoffman, F.O., Kanyár, B., Lyashenko, G., Nair, S.K., Popov, A., Raskob, W., Thiessen, K.M., Watkins, B., and Zheleznyak, M, 1999, Validation of Models of Radionuclide Wash-Off from Contaminated Watersheds using Chernobyl Data, J. Environ. Radioactivity, 42(2-3), pp. 131-141.

Kurvinen K., Smolander O., Pollanen R., Kukankorpi S., 2005, Design of a radiation surveillance unit for an unmanned aerial vehicle, Journal of Environmental Radioactivity, 81 (1), pp. 1-10.

Lo, B.H. and Pitcher, D.H., 1996, A Case History on the use of Regional Aeromagnetic and Radiometric Data Sets for Lode Gold Exploration in Ghana, Annual Meeting Expanded Abstracts, Society of Exploration Geophysicists, pp. 592-595.

Lucas G., Jozsef S., Hadmernok, 2015, Preliminary Study on the Detection of Radioactivity with Airborne Remote Sensing Systems, 8, pp. 137-155.

MacFarlane, J. W., Payton O. D., Keatley A. C., Scott G. P. T., Pullin H., Crane R. A., Smilion M., Popescu I., Curlea V., and Scott, 2014, Lightweight Aerial Vehicles for Monitoring, Assessment and Mapping of Radiation Anomalies, Journal of Environmental Radioactivity, pp. 136.

Malins A., Okumura M., Machida M. and Saito K., 2018, Topographic Efects on Ambient Dose Equivalent Rates from Radiocesium Fallout, Japan Atomic Energy.

Malley M. C., 2011, Radioactivity: A History of a Mysterious Science, First edition, Oxford University Press.

Marques M. R. M. , Carapau R. S., Rodriques A. V., Lobo V., Carvalho J., Antunes W. D., Goncalves T., Duarte F.S., Verissimo B., 2017, GammaEx Project: A Solution for CBRN Remote Sensing Using Unmanned Aerial Vehicles in Maritime Environments, Oceans Anchorage.

Marcus G.H. and Levin A. E, 2002, New Designs for Nuclear Renaissance, Physics Today, 55 (4), pp. 55.

Martin, P.G., Louvel, M., Cipiccia, S., Jones, C.P., Batey, D.J., Hallam, K.R., Yang, I.A.X., Satou, Y., Rau, C., Mosselmans, J.F.W., Richards, D.A. & Scott, T.B.,2014, Distribution, State and Composition of Uranium Contained Within FDNPP Unit 1 Particulate, Awaiting Publication, ACS Analytical Chemistry.

Martin, P.G., Payton, O.D., Fardoulis, J.S., Richards, D.A., Scott, T.B., 2015, The use of unmanned aerial systems for the mapping of legacy uranium mines, J. Environ. Radioact. 143.

Martin, P.G., Cipiccia, S., Batey. D., Hallam. K.R., Ang Xing Yang, I., Jones, C.P., Satou, Y., Griffiths, I., Rau, C. & Scott,T.B.,..., Internal Morphology and Composition of Fukushima-Derived Particulate Revealed Through High-Resolution Synchrotron Analysis, Awaiting Publication, ACS Environmental Science and Technology.

Martin, P.G., Payton, O.D., Leal-Olloqui, M. and Scott, T.B., 2018, Development and Initial Testing of A High-Resolution Mapping Platform to Aid in Public Awareness of Radiological Hazards and Effect, Journal of Radiological Protection, 38, pp. 329-342.

Martin, P.G, Tomkinson, N.G. and Scott, T.B., 2017, The Future of Nuclear Security: Commitment and Actions-Power Generation and Stewardship in the 21st Century, Energy Policy, 110, pp. 325-330.

Martin, P.G., Satou, Y., Griffiths, I., Richards, D.A. & Scott, T.B., 2017 , Analysis of External Surface Irregularities on Fukushima-Derived Fallout Particulate, In: Frontiers in Energy Research – Nuclear Energy, 5 (25), pp. 9.

Martin, P.G., Payton, O.D., Yamashiki, Y., Richards, D.A. & Scott, T.B., 2016, High-resolution Radiation Mapping to Investigate Fukushima Daiichi Nuclear Power Plant Derived Contaminant Migration, Journal of Enviromental Radioactivity, 164, pp. 26-35.
Martin, P.G., Moore, J., Fardoulis, J.S., Payton, O.D. & Scott, T.B., 2016, Remote Sensing , Radiological Assessment on Interest Areas on the Sellafield Nuclear Site via Unmanned Aerial Vehicle, 8 (11), pp. 10.

Mattila U., Tokola T., 2019, Terrain Mobility Estimation Using TWI and Airborne Gamma-ray Data, Journal of Environmental Management, 232, pp. 531-536.

Matzko J.R., Percious D.J., Rachlin J., and Marples , 1994, Observations on the geology and geohydrology of the Chernobyl' nuclear accident site, Ukraine, International Geology Review, 36 (2), pp. 203-211.

Minty, B., Luyendyk, A., Brodie, R., 1997, Calibration and Data Processing for Airborne Gamma Ray Spectrometry, AGSO Journal of Australian Geology And Geophysics, 17(2), pp. 51-62.

Mernagh T.M., Mienitiz Y., 2008, A Review of the Geochemical Processes Controlling the Distribution of Thorium in the Earth's Crust and Australia's Thorium Resources, GeoScience Australia, pp 48.

Mochizuki S., Kataoka J., Tagawa L., Iwamoto Y., Okochi H., Katsumi N., Kinno S., Arimoto M., Maruhashi T., Fujieda K., 2017, First Demonstration of Aerial Gamma-Ray Imaging Using Drone for Prompt Radiation Survey in Fukushima, Journal of Instrumentation, 12.

Morelande, M., B. Ristic, and A. Gunatilaka, 2007, Detection and Parameter Estimation of Multiple Radioactive Sources, 10th International Conference on Information Fusion, pp. 1–7.

Muske, K. R., and Howse J. W., 2001, Comparison of Recursive Estimation Techniques for Position Tracking Radioactive Sources, In Proceedings of the 2001 American Control Conference, 2, pp. 1656–1660.

Newaz A., Sungmoon J., Hosun L., Hyejeong R., Nak Y. C, 2016, UAV-Based Multiple Source Localization and Contouring Mapping of Radiation Fields, , Robotics and Autonomous Systems, 85, pp. 12-25.

Niedzielski T., 2018, Applications of Unmanned Aerial Vehicles in Geosciences: Introduction, Pure Applied Geophysics, 175 (9).

Nuttall W., Glowacki B.A., Clarke R., 2005, A Trip to Fusion Island, The Engineer, pp. 16-18.

Nygaard D. F., 1994, World population projections-2020, International Food Policy Research Institute (IFPRI), 2020 vision briefs, 5.

Ochi K., Sasaki M., Ishida M., Hamamoto S., Nishimura T., Sanada Y., 2017, Estimation of the Vertical Distribution of Radiocesium in Soil on the Basis of the Characteristics of

Gamma Ray Spectra Obtained via Aerial Radiation Monitoring Using an Unmanned Helicopter, Journal of Environmental Research and Public Health, 14, pp. 926

Pirttijarvi M., Radai O., 2016, Radai`S UAV Based Radiometric Measurements at Rautuvaara Mine İn Kolari, Survey Report.

Pires A. And Carmelo A. C. , 2018, Statistical Enhancement of Airborne Gamma-Ray Uranium Anomalies: Minimizing The Lithological Background Contribution in Mineral Exploration, Journal of Geochemical Exploration, 198.

Pöllänen R. , Toivonen H. , Peräjärvi K. , T. Karhunen, Ilander T. , Lehtinen J. , Rintala K. , Katajainen T. , Niemelä J. , Juusela M, 2009, Radiation Surveillance Using an Unmanned Aerial Vehicle, Application Radiation. Isotopes, 67 (2), pp. 340-344

Popel, A., V.A., L., Martin, P.G., A.A., S., Lampronti, G.I., Springell, R.S., Kalmykov, S. N., Scott, T.B., Monnet, I., Grygiel, C. & Farnan, I., 2016, Structural Effects in UO_2 Thin Films Irradiated with Fission-Energy Xe Ions, Journal of Nuclear Materials, 482, pp. 210-217.

Raymond F. K., Trude V.V. K., and Livo K. E., 2008, Airborne Hyperspectral Survey of Afghanistan 2007: Flight Line Planning and HyMap Data Collection, USGS Afghanistan Project Product, No. 186.

Rutherford, E.*;* Geiger, H. ,1908, An electrical method of counting the number of α particles from radioactive substances, Proceedings of the Royal Society. Series, 81 (546), pp. 141–161.

Sanderson D.C.W., Ferguson J.M., 1997, The European capability for environmental airborne gamma ray spectrometry. Radiation Protection Dosimetry, 73, pp. 213- 218.

Sanderson D.C.W. , Cresswell A.J. and White D.C., 2008, The Effect of Flight Line Spacing on Radioactivity Inventory and Spatial Feature Characteristics of Airborne Gamma-Ray Spectrometry Data, International Journal of Remote Sensing, 29(1), pp. 31-46.

Sato Y., Ozawa S., Terasaka, Kaburagi M., Tanifuji Y., Kawabata K., Miyamura N. H., Izumi R., Torii T.& Suzuki Toshikazu, 2018, Remote Radiation Imaging System Using A Compact Gamma-ray Imager Mounted on A Multicopter Drone, Journal of Nuclear Science and Technology, 55(1), pp. 90-96.

Sanada Y., Sugita T. , Nishizawa Y. , Kondo A. , Torii T., 2014a, The Airborne Radiation Monitoring in Japan After the Fukushima Daiichi Nuclear Power Plant Accident, Prog. Nucl. Sci. Tech., 4, pp. 76-80.

Sanada Y., Kondo A. , Sugita T. , Nishizawa Y. , Yuuki Y., Ikeda K. , Shoji Y. , Torii T. , 2014, Radiation Monitoring Using an Unmanned Helicopter in The Evacuation Zone around The Fukushima Daiichi Nuclear Power Plant, Exploration Geophysics, 45 , pp. 3-7.

Sanada Y., and Torii T., 2015, Aerial Radiation Monitoring around the Fukushima Dai-Ichi Nuclear Power Plant Using an Unmanned Helicopter, Journal of Environmental Radioactivity, 139, pp. 294– 299.

Sanada Y., Orita T., Torii T., 2016, Temporal Variation of Dose Rate Distribution around Fukushima Daiichi Nuclear Power Station Using Unmanned Helicopter, Applied Radiation and Isotopes, 118, pp. 308-316.

Sezan M.I. and Stark H., 1987, Applications Of Convex Projection Theory To Image Recovery In Tomography and Related Areas, Image Recovery: Theory and Application, Ed. H. Stark, Academic Press, Orlando.

Schetselaar E., 2002, Petrogenetic Interpretation from Gamma-Ray Spectrometry and Geological Data: The Arch Lake Zoned Peraluminous Granite Intrusion, Western Canadian Shield, Exploration Geophysics.

Schwarz K. P., Colombo 0., Hein G., Knickmeyer E.T., 1992, Requirements for Airborne Vector Gravimetry, Proceedings of IAG Symposium from Mars to Greenland: Charting Gravity with Space and Airborne Instruments, pp. 273-283.

Schwarz, G. F., Rybach L., Barlocher C. K., and Klingele E. E, 1995, Development and Calibration of an Airborne Radiometric Measuring System, IAEA TECDOC-827, 8, pp. 26–35.

Schwarz, G. F., Rybach L., and Klingele E. E., 1995, Data Processing and Mapping in Airborne Radioactivity Surveys, IAEA TECDOC-827, 8, pp. 61–70.

Schelkanova I., Pandya A., Muhaseen A, Saiko G., Douplik A., 2015, Biophotonics for Medical Applications, Woodhead Publishing Series in Biomaterials, pp. 347-375.

Shives R.B.K., Ford K.L., and Charbonneau B.W., 1995, Applications of Gamma-Ray Spectrometric/Magnetic/ VLF-EM Surveys–Workshop Manual: Geological Survey of Canada, Open File 3061, pp. 82.

Shippert, P., 2004, Why Use Hyperspectral Imagery?, Photogrammetric Engineering & Remote Sensing, pp. 377 – 380.

Smith Dave-Megson, 2015, Photons: Tools at the Nanoscale, PhD Thesis, University of Bath, pp. 1-244.

Stefanik, K. V., J. C. Gassaway, K. Kochersberger, and A. L. Abbott, 2013, UAV-Based Stereo Vision for Rapid Aerial Terrain Mapping, GIScience & Remote Sensing.

Stibinger P., 2017, Localization of a Radiation Source by a Formation of Unmanned aerial Vehicles, Czech Technical University, Bachelor Thesis.

Strohmer T., Vershynin R., 2009, Comments on the Randomized Kaczmarz Method, Journal of Fourier Analysis and Applications, 15 (4), pp. 437–440.

Tang X., Meng J., Wang P., 2016, Efficiency Calibration And Minimum Detectable Activity Concentration Of A Real-Time UAV Airborne Sensor System With Two Gamma Spectrometers, Applied Radiation Isotopes, 110, pp. 100-108.

Telford, W.M., Geldart, L.P. and Keys, D.A., 1976, Applied Geophysics, Cambridge University Press, Cambridge, pp. 860.

Toivonen H., 1997, Detection of hidden sources, Prompt reports by airborne teams in Resume95, Web.

Turhan S., Arikan I. H., Oguz F., Ozdemir T., 2011, Car-Borne Survey Of Natural Background Gamma Dose Rate In Çanakkale Region, Turkey, Radiation Protection Dosimetry 148(1):45-50.

Towler J., Krawiec B. and Kochersberger K., 2012, Radiation Mapping in Post-Disaster Environments Using an Autonomous Helicopter, Remote Sensing, 4, pp. 1995-2015.

Tyler A.N., Sanderson D.C.W., Scott E.M., 1996, Estimating And Accounting for ^{137}Cs Source Burial Through in-Situ Gamma Spectrometry in Salt Marsh Environments, Journal of Environmental Radioactivity, 33 (3), pp. 195-212.

Uyanik N.A., Akkurt I and Uyanik O.., 2011, A Ground Radiometric Study Of Uranium, Throuim And Potassium in Isparta, Turkey, Annals of Geophysics, 53, pp. 5-6.

Uyanik N.A., Öncü Z. , Uyanik O. and Akkurt I., 2015, Determination of Natural Radioactivity from ^{232}Th with Gamma-Ray Spectrometer in Dereköy - Yazır (Southwestern Anatolia), Acta Physica Polonica, 128, pp 29-30.

Uzmen R., 2015, Uranium and Thorium Production Projections in Turkey, Proceedings of Global 2015, 21st International Conference & Exhibition: "Nuclear Fuel Cycle for a Low-Carbon Future, 5056.

Xu, S., Zhang, L., Freeman, S. P.H.T. , Hou, X., Shibata, Y., Sanderson, D. , Cresswell, A. , Doi, T. and Tanaka, A. (2015) Speciation of Radiocesium and Radioiodine in Aarosols from Tsukuba after the Fukushima Nuclear Accident, Environmental Science and Technology, 49(2), pp. 1017-1024.

Varley A., Tyler A., Smith L., Dalec P., Davies M., 2016, Mapping The Spatial Distribution and Activity of ^{226}Ra At Legacy Sites Through Machine Learning Interpretation of Gamma-ray Spectrometry Data, Science of the Total Environment, 545-546, pp. 654-661.

Versteeg, J.K. and Paterson, N.R., 1997, Report on Revaluation of Airborne Geophysical Anomalies, Guaniamo area, Venezuela, Paterson, Grant & Watson Limited.

Wells, P. N. T. , 2005, Sir Godfrey Newbold Hounsfield KT CBE, Biographical Memoirs of Fellows of the Royal Society, 51, pp. 221–235.

Zabulonov Y., Burtnyak V.M., Zolkin I.O, 2014, Airborne Gamma Spectrometric Survey in the Chernobyl Exclusion Zone Based on Oktokopter UAV type, Voprosy Atomnoj Nauki i Tekhniki, 99(5), pp. 163-167.

Zabulonov, Yu., Burtniak, V., Krasnoholovets, V., 2016, A Method of Rapid Testing of Radioactivity of Different Materials, Journal of Radiation Res. Appl. Sci., 9, pp. 370-375.

Zhang W., Wu J., 2014, To Explore the UAV Application in Disaster Prevention and Reduction, Applied Mechanics and Materials, 590, pp. 609-612.

Zhdanov M., 2015, Inverse Theory and Applications in Geophysics, Second Edition, Elsevier.

11. Electronic Sources

[1]http://www.tellusgb.ac.uk/

[2]https://www.researchgate.net/publication/312040305_Uranium_and_thorium_production_projections_in_Turkey

[3]https://pubs.usgs.gov/of/2004/1050/uranium.htm

[4]https://www.iaea.org/publications/12346/geological-classification-of-uranium-deposits-and-description-of-selected-examples

[5]https://en.wikipedia.org/wiki/Caesium-137

[6]https://www.researchgate.net/publication/322645215_Application_of_Bayesian_and_Geostatistical_Modeling_to_the_Environmental_Monitoring_of_Cs137_at_the_Idaho_National_Laboratory

[7]http://www.gfinstruments.cz/index.php?menu=gi&smenu=igr&cont=surveyor_V_&ear=ov

[8] https://www.dji.com/uk/mavic

[9]http://vro.agriculture.vic.gov.au/dpi/vro/vrosite.nsf/pages/landform_glossary_radio

[10]https://www.researchgate.net/publication/323366353_Utilizing_UAV_and_3D_Computer_Vision_for_Visual_Inspection_of_a_Large_Gravity_Dam

[11]https://www.researchgate.net/profile/Peter_G_Martin

[12]https://doi.org/10.1016/j.jappgeo.2016.07.006

[13]https://www.mdpi.com/2072-4292/8/11/913/html

[14]https://www.tandfonline.com/loi/tres20

[15] https://www.harris.com/

[16] https://www.dji.com/uk/phantom

[17] https://www.routescene.com/the-3d-mapping-solution/uav-lidar-system/

[18] https://www.agisoft.com/pdf/photoscan-pro_1_4_en.pdf

[19] https://www.kromek.com/

[20] https://store.dji.com/product/matrice-600-pro

[21] LidarViewer for Desktop Software

[22] https://www.mathworks.com/matlabcentral/fileexchange/46350-inverse distance-weight-function

APPENDIX I

1.1 Karcmarz algorithm for ISL

```
clc;
clear all;
%%%%%DATA INPUT%%%%%
```

```
load isldroneResults20.mat;
load isldroneResults30.mat;
load isldroneResults40.mat;
load islxfourtythirty.mat;
load islxfourtythirtytwenty.mat;
load xfourtythirtytwentyfifteen.mat;
load droneResults40302015.mat;

%%%%%%%%UAV COEFFICIENT FROM WGS84 TO UTM%%%%%%%%%%%%%%
latCoef = 114491.8497;  %lat m/deg
longCoef = 71795.30699; %long m/deg

%DEM DATA INPUT%%%%%%%%%%%%%%%%%%%%%%%%%%%%%%%%%%%%%%%
A=Tiff('KOBACHIDEM5096.tif');
imageData1=read(A)+132;
imageData1(imageData1==-32635)=120.1325;
imageData1=imageData1';
[px1,py1]=size(imageData1);
LatRange1=51.34479854020763:-2.69257695e-05:(-2.69257695e-05*(py1-
1)+51.34479854020763);
LongRange1=30.1086943054718:4.299253577e-05:(4.299253577e-05*(px1-
1)+30.1086943054718);
controlx=repmat(LongRange1,80,1);
controlxx=controlx';
[px2,py2]=size(controlxx);
controly=repmat(LatRange1,96,1);
[px3,py3]=size(controly);

% % %%%%%%%KARCZMARZ ALGORTHM INPUT%%%%%%%%%%%%%
xfourtythirtytwentyfifteen= zeros(size(imageData1));
updates = 100000;%iteration number
damping=0.03;%damping factor
droneReadings = length(X40302015M);

% % % KARCZMARZ ALGORTHM CALCULATION FOR FL 15M%%%%%%%%%
for i=1:updates
   i
   randomDronePosition = randi([1 droneReadings]);
   if  VarName2(randomDronePosition) > 10
      xnew=(VarName5(randomDronePosition)-controlxx(:,:)).*longCoef;
      ynew=(VarName4(randomDronePosition)-controly(:,:)).*latCoef;
      znew= VarName7(randomDronePosition)-imageData1(:,:);
      radiusSquared15=(xnew.^2)+ (ynew.^2)+ (znew.^2);
      %radius15 = radiusSquared15.^0.5;
      A15=1./(radiusSquared15);
      bg=0.065;
      randomDroneCounts15 = VarName9(randomDronePosition);
```

```
      update15= A15.*(randomDroneCounts15 - sum(sum(xfifteen .*
A15))./sum(sum(A15)));
      xfifteen(:,:)=xfifteen(:,:)+(damping.*update15);
      xfifteen(xfifteen<bg)=bg;
   end
end

% RELATIVE ERROR CALCULATION OF INVERTED RESULTS FOR FL 15M%%%
droneResults15 = zeros(droneReadings, 6);
for i=1:droneReadings
   xnew=(VarName5(i)-controlxx(:,:)).*longCoef;
   ynew=(VarName4(i)-controly(:,:)).*latCoef;
   znew=VarName7(i)-imageData1(:,:);
   if  VarName2(i) > 10
      droneCounts15 = VarName9(i);
      radiusSquared15=(xnew.^2)+ (ynew.^2)+ (znew.^2);
      A15=1./radiusSquared15;
      droneCountsEstimate15 = sum(sum(xfifteen .* A15));
      relativeError15=abs(droneCounts15 - droneCountsEstimate15)./droneCounts15;
      droneResults15(i,:) = [VarName5(i), VarName4(i), VarName7(i), droneCounts15,
droneCountsEstimate15, relativeError15];
   end
end

%  KACMARZ ALGORTHM CALCULATION FOR FL 20M%
for i=1:updates
   i
   randomDronePosition = randi([1 droneReadings]);
   if  LIDAR20M(randomDronePosition) > 15
      xnew=(X20M(randomDronePosition)-controlxx(:,:)).*longCoef;
      ynew=(Y20M(randomDronePosition)-controly(:,:)).*latCoef;
      znew=Z20M(randomDronePosition)-imageData1(:,:);
      radiusSquared20=(xnew.^2)+ (ynew.^2)+ (znew.^2);
      A20=1./(radiusSquared20);
      bg=0.065;
      randomDroneCounts20 = CPS20M(randomDronePosition);
      update20= A20.*(randomDroneCounts20 - sum(sum(xtwenty .*
A20))./sum(sum(A20)));
      xtwenty(:,:)=xtwenty(:,:)+(damping.*update20);
      xtwenty(xtwenty<bg)=bg;
   end
end

%RELATIVE ERROR CALCULATION OF INVERTED RESULTS FOR FL 20M%
droneResults20 = zeros(droneReadings, 6);
for i=1:droneReadings
   xnew=(X20M(i)-controlxx(:,:)).*longCoef;
   ynew=(Y20M(i)-controly(:,:)).*latCoef;
```

```
   znew=Z20M(i)-imageData1(:,:);
   if  LIDAR20M(i) > 15
      droneCounts20 = CPS20M(i);
      radiusSquared20=(xnew.^2)+ (ynew.^2)+ (znew.^2);
       A20=1./(radiusSquared20);
      droneCountsEstimate20 = sum(sum(xtwenty .* A20));
      relativeError20=abs(droneCounts20 - droneCountsEstimate20)./droneCounts20;
      droneResults20(i,:) = [X20M(i), Y20M(i), Z20M(i), droneCounts20,
droneCountsEstimate20, relativeError20];
   end
end

% KARCZMARZ ALGORTHM CALCULATION FOR FL 30M%
for i=1:updates
   i
   randomDronePosition = randi([1 droneReadings]);
   if  LIDAR30M(randomDronePosition) > 25
      xnew=(X30M(randomDronePosition)-controlxx(:,:)).*longCoef;
      ynew=(Y30M(randomDronePosition)-controly(:,:)).*latCoef;
      znew=Z30M(randomDronePosition)-imageData1(:,:);
      radiusSquared30=(xnew.^2)+ (ynew.^2)+ (znew.^2);
      A30=1./(radiusSquared30);
      bg=0.065;
      randomDroneCounts30 = CPS30M(randomDronePosition);
      update30= A30.*(randomDroneCounts30 - sum(sum(xthirty .*
A30))./sum(sum(A30)));
      xthirty(:,:)=xthirty(:,:)+(damping.*update30);
      xthirty(xthirty<bg)=bg;
   end
end

%RELATIVE ERROR CALCULATION OF INVERTED RESULTS FOR FL 30M%%%%
droneResults30 = zeros(droneReadings, 6);
for i=1:droneReadings
   xnew=(X30M(i)-controlxx(:,:)).*longCoef;
   ynew=(Y30M(i)-controly(:,:)).*latCoef;
   znew=Z30M(i)-imageData1(:,:);
   if  LIDAR30M(i) > 25
      droneCounts30 = CPS30M(i);
      radiusSquared30=(xnew.^2)+ (ynew.^2)+ (znew.^2);
      A30=1./(radiusSquared30);
      droneCountsEstimate30 = sum(sum(xthirty .* A30));
      relativeError30=abs(droneCounts30 - droneCountsEstimate30)./droneCounts30;
      droneResults30(i,:) = [X30M(i), Y30M(i), Z30M(i), droneCounts30,
droneCountsEstimate30, relativeError30];
   end
end
```

```
% KARCZMARZ ALGORTHM CALCULATION FOR FL 40M%
for i=1:updates
  i
  randomDronePosition = randi([1 droneReadings]);
  if  LIDAR40M(randomDronePosition) > 25
    xnew=(X40M(randomDronePosition)-controlxx(:,:)).*longCoef;
    ynew=(Y40M(randomDronePosition)-controly(:,:)).*latCoef;
    znew=Z40M(randomDronePosition)-imageData1(:,:);
    radiusSquared40=(xnew.^2)+ (ynew.^2)+ (znew.^2);
    A40=1./(radiusSquared40);
    bg=0.065;
    randomDroneCounts40 = CPS40M(randomDronePosition);
    update40= A40.*(randomDroneCounts40 - sum(sum(xfourty .*
A40))./sum(sum(A40)));
    xfourty(:,:)=xfourty(:,:)+(damping.*update40);
    xfourty(xfourty<bg)=bg;
  end
end


%RELATIVE ERROR CALCULATION OF INVERTED RESULTS FOR FL 40M%
droneResults40 = zeros(droneReadings, 6);
for i=1:droneReadings
  xnew=(X40M(i)-controlxx(:,:)).*longCoef;
  ynew=(Y40M(i)-controly(:,:)).*latCoef;
  znew=Z40M(i)-imageData1(:,:);
  if  LIDAR40M(i) > 35
    droneCounts40 = CPS40M(i);
    radiusSquared40=(xnew.^2)+ (ynew.^2)+ (znew.^2);
    A40=1./(radiusSquared40);
    droneCountsEstimate40 = sum(sum(xfourty .* A40));
    relativeError40=abs(droneCounts40 - droneCountsEstimate40)./droneCounts40;
    droneResults40(i,:) = [X40M(i), Y40M(i), Z40M(i), droneCounts40,
droneCountsEstimate40, relativeError40];
  end
end


%PLOTTING INVERSION RESULTS FOR EACH ALTITUDE OF MULTI-ROTOR FLIGHTS%
figure(1)
subplot(2,2,1)
surf(imageData1,xfourty);
xlabel('Distance(m)','FontSize',12,'FontWeight','bold','Color','k');
ylabel('Distance(m)','FontSize',12,'FontWeight','bold','Color','k');
title('FL40 ART Result','FontSize',12,'FontWeight','bold','Color','k');
fig1=colorbar;
```

```
title(fig1,'Inverted Total Counts(cps)','FontSize',12,'FontWeight','bold','Color','k')
subplot(2,2,2)
surf(imageData1,xthirty);
title('FL30 ART Result','FontSize',12,'FontWeight','bold','Color','k');
xlabel('Distance(m)','FontSize',12,'FontWeight','bold','Color','k');
ylabel('Distance(m)','FontSize',12,'FontWeight','bold','Color','k');
fig2=colorbar;
title(fig2,'Inverted Total Counts(cps)','FontSize',12,'FontWeight','bold','Color','k')
subplot(2,2,3)
surf(imageData1,xtwenty);
fig3=colorbar;
title(fig3,'Inverted Total Counts(cps)','FontSize',12,'FontWeight','bold','Color','k')
title('FL20 ART Result','FontSize',12,'FontWeight','bold','Color','k');
xlabel('Distance(m)','FontSize',12,'FontWeight','bold','Color','k');
ylabel('Distance(m)','FontSize',12,'FontWeight','bold','Color','k');
subplot(2,2,4)
surf(imageData1,xfifteen);
title('FL15 ART Result','FontSize',12,'FontWeight','bold','Color','k');
xlabel('Distance(m)','FontSize',12,'FontWeight','bold','Color','k');
ylabel('Distance(m)','FontSize',12,'FontWeight','bold','Color','k');
fig4=colorbar;
title(fig4,'Inverted Total Counts(cps)','FontSize',12,'FontWeight','bold','Color','k')

%PLOTTING RELATIVE ERRORS FROM INVERTED TOTAL COUNTS FOR THE EACH
ALTITUDE OF MULTI-ROTOR FLIGHTS%
figure(2)
subplot(2,2,1)
histogram(droneResults40(:,6))
title('FL40','FontSize',12,'FontWeight','bold','Color','k');
ylabel('Number of Inverted Total Counts','FontSize',12,'FontWeight','bold','Color','k');
xlabel('Relative Error','FontSize',12,'FontWeight','bold','Color','k');
subplot(2,2,2)
histogram(droneResults30(:,6))
title('FL30','FontSize',12,'FontWeight','bold','Color','k');
ylabel('Number of Inverted Total Counts','FontSize',12,'FontWeight','bold','Color','k');
xlabel('Relative Error','FontSize',12,'FontWeight','bold','Color','k');
subplot(2,2,3)
histogram(droneResults20(:,6))
title('FL20','FontSize',12,'FontWeight','bold','Color','k');
ylabel('Number of Inverted Total Counts','FontSize',12,'FontWeight','bold','Color','k');
xlabel('Relative Error','FontSize',12,'FontWeight','bold','Color','k');
subplot(2,2,4)
histogram(droneResults15(:,6))
title('FL15','FontSize',12,'FontWeight','bold','Color','k');
ylabel('Number of Inverted Total Counts','FontSize',12,'FontWeight','bold','Color','k');
xlabel('Relative Error','FontSize',12,'FontWeight','bold','Color','k');
```

```
%COMBINATION OF MULTI-ROTOR FLIGHTS %%%%%%%%%%%%%%%%%%%%
% KARCZMARZ ALGORTHM CALCULATION FOR FL 40M + FL 30M%%%%%%%%%%
CPS30M=imresize(CPS30M,[unknowns 1]);
X30M=imresize(X30M,[unknowns 1]);
Y30M=imresize(Y30M,[unknowns 1]);
Z30M=imresize(Z30M,[unknowns 1]);
LIDAR30M=imresize(LIDAR30M,[unknowns 1]);
X4030M=[X40M;X30M];
Y4030M=[Y40M;Y30M];
Z4030M=[Z40M;Z30M];
CPS4030M=[CPS40M;CPS30M];
LIDAR4030M=[LIDAR40M;LIDAR30M];

for i=1:updates
  i
  randomDronePosition = randi([1 droneReadings]);
  if  LIDAR4030M(randomDronePosition) > 25
    xnew=(X4030M(randomDronePosition)-controlxx(:,:)).*longCoef;
    ynew=(Y4030M(randomDronePosition)-controly(:,:)).*latCoef;
    znew= Z4030M(randomDronePosition)-imageData1(:,:);
    radiusSquared4030=(xnew.^2)+ (ynew.^2)+ (znew.^2);
    A4030=1./(radiusSquared4030);
    bg=0.065;
    randomDroneCounts4030 = CPS4030M(randomDronePosition);
    update4030= A4030.*(randomDroneCounts4030 - sum(sum(xfourtythirty .*
A4030))./sum(sum(A4030)));
    xfourtythirty(:,:)=xfourtythirty(:,:)+(damping.*update4030);
    xfourtythirty(xfourtythirty<bg)=bg;
  end
end

% KARCZMARZ ALGORTHM CALCULATION FOR FL 40M + FL 30M + FL 20M %
X403020M=[X40M;X30M;X20M];
Y403020M=[Y40M;Y30M;Y20M];
Z403020M=[Z40M;Z30M;Z20M];
CPS403020M=[CPS40M;CPS30M;CPS20M];
LIDAR403020M=[LIDAR40M;LIDAR30M;LIDAR20M];
for i=1:updates
  i
  randomDronePosition = randi([1 droneReadings]);
  if  LIDAR403020M(randomDronePosition) > 15
    xnew=(X403020M(randomDronePosition)-controlxx(:,:)).*longCoef;
    ynew=(Y403020M(randomDronePosition)-controly(:,:)).*latCoef;
    znew= Z403020M(randomDronePosition)-imageData1(:,:);
    radiusSquared403020=(xnew.^2)+ (ynew.^2)+ (znew.^2);
    A403020=1./(radiusSquared403020);
```

```
      bg=0.065;
      randomDroneCounts403020 = CPS403020M(randomDronePosition);
      update403020= A403020.*(randomDroneCounts403020 -
sum(sum(xfourtythirtytwenty .* A403020))./sum(sum(A403020)));
      xfourtythirtytwenty(:,:)=xfourtythirtytwenty(:,:)+(damping.*update403020);
      xfourtythirtytwenty(xfourtythirtytwenty<bg)=bg;
   end
end

% KARCZMARZ ALGORTHM CALCULATION FOR FL 40M + FL 30M + FL 20M +FL15M
% X40302015M=[X40M;X30M;X20M;VarName5];
% Y40302015M=[Y40M;Y30M;Y20M;VarName4];
% Z40302015M=[Z40M;Z30M;Z20M;VarName7];
% CPS40302015M=[CPS40M;CPS30M;CPS20M;VarName9];
% LIDAR40302015M=[LIDAR40M;LIDAR30M;LIDAR20M;VarName2];
for i=1:updates
   i
   randomDronePosition = randi([1 droneReadings]);
   if  LIDAR40302015M(randomDronePosition) > 10
      xnew=(X40302015M(randomDronePosition)-controlxx(:,:)).*longCoef;
      ynew=(Y40302015M(randomDronePosition)-controly(:,:)).*latCoef;
      znew= Z40302015M(randomDronePosition)-imageData1(:,:);
      radiusSquared40302015=(xnew.^2)+ (ynew.^2)+ (znew.^2);
      A40302015=1./(radiusSquared40302015);
      bg=0.065;
      randomDroneCounts40302015 = CPS40302015M(randomDronePosition);
      update40302015= A40302015.*(randomDroneCounts40302015 -
sum(sum(xfourtythirtytwentyfifteen .* A40302015))./sum(sum(A40302015)));

xfourtythirtytwentyfifteen(:,:)=xfourtythirtytwentyfifteen(:,:)+(damping.*update40302
015);
      xfourtythirtytwentyfifteen(xfourtythirtytwentyfifteen<bg)=bg;
   end
end

%RELATIVE ERROR CALCULATION OF INVERTED RESULTS FOR FL 40M +FL 30M+ FL
%20M +FL 10M%
droneResults40302015 = zeros(droneReadings, 6);
for i=1:droneReadings
   xnew=(X40302015M(i)-controlxx(:,:)).*longCoef;
   ynew=(Y40302015M(i)-controly(:,:)).*latCoef;
   znew=Z40302015M(i)-imageData1(:,:);
   if  LIDAR40302015M(i) > 10
      droneCounts40302015 = CPS40302015M(i);
      radiusSquared40302015=(xnew.^2)+ (ynew.^2)+ (znew.^2);
      A40302015=1./(radiusSquared40302015);
      droneCountsEstimate40302015 = sum(sum(xfourtythirtytwentyfifteen .*
A40302015));
```

```
    relativeError40302015=abs(droneCounts40302015 -
droneCountsEstimate40302015)./droneCounts40302015;
    droneResults40302015(i,:) = [X40302015M(i), Y40302015M(i), Z40302015M(i),
droneCounts40302015, droneCountsEstimate40302015, relativeError40302015];
  end
end


%PLOTTING INVERSION RESULTS FOR THE COMBINATION OF MULTI-ROTORFLIGHTS
figure(2)
subplot(1,3,1)
surf(imageData1,xfourtythirty);
xlabel('Distance(m)','FontSize',12,'FontWeight','bold','Color','k');
ylabel('Distance(m)','FontSize',12,'FontWeight','bold','Color','k');
title('FL40+FL30 ART Result','FontSize',12,'FontWeight','bold','Color','k');
fig1=colorbar;
colormap('jet');
title(fig1,'Inverted Total Counts(cps)','FontSize',12,'FontWeight','bold','Color','k')
subplot(1,3,2)
surf(imageData1,xfourtythirtytwenty);
title('FL40+FL30+FL20 ART Result','FontSize',12,'FontWeight','bold','Color','k');
xlabel('Distance(m)','FontSize',12,'FontWeight','bold','Color','k');
ylabel('Distance(m)','FontSize',12,'FontWeight','bold','Color','k');
fig2=colorbar;
colormap('jet');
title(fig2,'Inverted Total Counts(cps)','FontSize',12,'FontWeight','bold','Color','k')
subplot(1,3,3)
surf(imageData1,xfourtythirtytwentyfifteen);
title('FL40+FL30+FL20+FL15 ART Result','FontSize',12,'FontWeight','bold','Color','k');
xlabel('Distance(m)','FontSize',12,'FontWeight','bold','Color','k');
ylabel('Distance(m)','FontSize',12,'FontWeight','bold','Color','k');
fig3=colorbar;
colormap('jet');
title(fig3,'Inverted Total Counts(cps)','FontSize',12,'FontWeight','bold','Color','k')

%PLOTTING INVERSION RESULTS FOR THE FL 15M AND FL 40M +FL 30M+ FL 20M+FL
%10M

figure(3)
subplot(1,2,1)
surf(imageData1,xfifteen);
fig1=colorbar;
colormap('hsv');
title(fig1,'Inverted Total Counts(cps)','FontSize',12,'FontWeight','bold','Color','k')
xlabel('Distance(m)','FontSize',12,'FontWeight','bold','Color','k');
ylabel('Distance(m)','FontSize',12,'FontWeight','bold','Color','k');
title('FL15 Inversion Result','FontSize',12,'FontWeight','bold','Color','k');
subplot(1,2,2)
```

```
surf(imageData1,xfourtythirtytwentyfifteen);
fig2=colorbar;
colormap('hsv');
title(fig2,'Inverted Total Counts(cps)','FontSize',12,'FontWeight','bold','Color','k')
title('FL40+FL30+FL20+FL15 Inversion
Result','FontSize',12,'FontWeight','bold','Color','k');
xlabel('Distance(m)','FontSize',12,'FontWeight','bold','Color','k');
ylabel('Distance(m)','FontSize',12,'FontWeight','bold','Color','k');

%RELATIVE ERROR CALCULATION OF INVERTED RESULTS FOR FL 15M AND FL 40M
+FL 30M+ FL 20M +FL 10M
figure(4)
subplot(1,2,1)
histogram(droneResults15(:,6))
title('FL15','FontSize',12,'FontWeight','bold','Color','k');
ylabel('Number of Inverted Total Counts','FontSize',12,'FontWeight','bold','Color','k');
xlabel('Relative Error','FontSize',12,'FontWeight','bold','Color','k');
subplot(1,2,2)
histogram(droneResults40302015(:,6))
title('FL40+FL30+FL20+FL15 ','FontSize',12,'FontWeight','bold','Color','k');
ylabel('Number of Inverted Total Counts','FontSize',12,'FontWeight','bold','Color','k');
xlabel('Relative Error','FontSize',12,'FontWeight','bold','Color','k');
```

1.2 Karcmarz algorithm for ISL plus energy attenuation

```
2   clc;
3   clear all;
4   load uav15mxcor.mat;
5   load uav15mycor.mat;
6   load uav15mcounts.mat;
7   load uav15mznewcor.mat;
8   load VarName2.mat;
9   load X20M.mat;
10  load Y20M.mat;
11  load Z20M.mat;
12  load CPS20M.mat;
13  load X30M.mat;
14  load Y30M.mat;
15  load Z30M.mat;
16  load CPS30M.mat;
17  load X40M.mat;
18  load Y40M.mat;
19  load Z40M.mat;
20  load CPS40M.mat;
21  load GROUNDKOBACHIX.mat;
22  load GROUNDKOBACHIY.mat;
23  load GROUNDKOBACHICPS.mat;
24  load LIDAR20M.mat;
```

```
load LIDAR30M.mat;
load LIDAR40M.mat;
load LIDARFIXEDWING1.mat;
load FIXEDWING1X.mat;
load FIXEDWING1Y.mat;
load FIXEDWING1Z.mat;
load CPSFIXEDWING1.mat;
load LIDARFIXEDWING2.mat;
load FIXEDWING2X.mat;
load FIXEDWING2Y.mat;
load FIXEDWING2Z.mat;
load CPSFIXEDWING2.mat;
load X1int.mat;
load X2int.mat;
load F1.mat;
load F2.mat;
load F3.mat;
load F4.mat;
%%%%%%%%%%%%%%%%%%%%%%%%%%%DEM DATA INPUT%%%%%%%%%%%%%%%%%%%%%%%%%%%%%%%
A=Tiff('KOBACHIDEM5096.tif');
imageData1=read(A)+132;
imageData1(imageData1==-32635)=120.1325;
imageData1=imageData1';
[px1,py1]=size(imageData1);
LatRange1=51.34479854020763:-2.69257695e-05:(-2.69257695e-05*(py1-1)+51.34479854020763);
LongRange1=30.1086943054718:4.299253577e-05:(4.299253577e-05*(px1-1)+30.1086943054718);
controlx=repmat(LongRange1,80,1);
controlxx=controlx';
[px2,py2]=size(controlxx);
controly=repmat(LatRange1,96,1);
[px3,py3]=size(controly);

xfourtythirtytwentyfifteen= zeros(size(imageData1));
a=size(xfourtythirtytwentyfifteen);
unknowns=a(:,1)*a(:,2);
updates = 100000;%100000 best
damping=0.08;%0.08 best
droneReadings = length(X40302015M);

%%%%%%%%%%%%%%%%%%%KACRMARZ ALGORTHM 15M CALCULATION%%%%%%%%%%%%%%%%%%%
for i=1:updates
    i
    randomDronePosition = randi([1 droneReadings]);
```

```
68    if VarName2(randomDronePosition) > 10
69       xnew=(VarName5(randomDronePosition)-controlxx(:,:)).*longCoef;
70       ynew=(VarName4(randomDronePosition)-controly(:,:)).*latCoef;
71       znew= VarName7(randomDronePosition)-imageData1(:,:);
72       radiusSquared15=(xnew.^2)+ (ynew.^2)+ (znew.^2);
73       radius15 = radiusSquared15.^0.5;
74       A15=(0.5.^(radius15./72))./(radius15.^2);
75       bg=0;
76       randomDroneCounts15 = VarName9(randomDronePosition);
77       update15= A15.*(randomDroneCounts15 - sum(sum(xfifteen .*
   A15))./sum(sum(A15)));
78       xfifteen(:,:)=xfifteen(:,:)+(damping.*update15);
79       xfifteen(xfifteen<bg)=bg;
80    end
81 end


82 %%%%%%%%%%%%%%%%%%%%%%%%%%%%%15M RELATIVE
   ERROR%%%%%%%%%%%%%%%%%%%%%%%%%%%%%
83 droneResults15 = zeros(droneReadings, 6);
84 for i=1:droneReadings
85    xnew=(VarName5(i)-controlxx(:,:)).*longCoef;
86    ynew=(VarName4(i)-controly(:,:)).*latCoef;
87    znew=VarName7(i)-imageData1(:,:);
88    if VarName2(i) > 10
89       droneCounts15 = VarName9(i);
90       radiusSquared15=(xnew.^2)+ (ynew.^2)+ (znew.^2);
91       radius15 = radiusSquared15.^0.5;
92       A15=(0.5.^(radius15./72))./(radius15.^2);
93       droneCountsEstimate15 = sum(sum(xfifteen .* A15));
94       relativeError15=abs(droneCounts15 -
   droneCountsEstimate15)./droneCounts15;
95       droneResults15(i,:) = [VarName5(i), VarName4(i), VarName7(i),
   droneCounts15, droneCountsEstimate15, relativeError15];
96    end
97 end
98
99 %%%%%%%%%%%%%%%%%%%%%%KACMARZ ALGORTHM 20M
   CALCULATION%%%%%%%%%%%%%%%%%%%%
100    for i=1:updates
101       i
102       randomDronePosition = randi([1 droneReadings]);
103       if LIDAR20M(randomDronePosition) > 15
104          xnew=(X20M(randomDronePosition)-controlxx(:,:)).*longCoef;
105          ynew=(Y20M(randomDronePosition)-controly(:,:)).*latCoef;
106          znew=Z20M(randomDronePosition)-imageData1(:,:);
107          radiusSquared20=(xnew.^2)+ (ynew.^2)+ (znew.^2);
108          radius20 = radiusSquared20.^0.5;
```

```
109         A20=(0.5.^(radius20./72))./(radius20.^2);
110         bg=0;
111         randomDroneCounts20 = CPS20M(randomDronePosition);
112         update20= A20.*(randomDroneCounts20 - sum(sum(xtwenty .*
    A20))./sum(sum(A20)));
113         xtwenty(:,:)=xtwenty(:,:)+(damping.*update20);
114         xtwenty(xtwenty<bg)=bg;
115       end
116    end
117
118    %%%%%%%%%%%%%%%%%%%%%%%%%%20M RELATIVE
    ERROR%%%%%%%%%%%%%%%%%%%%%%%%%%%
119    droneResults20 = zeros(droneReadings, 6);
120    for i=1:droneReadings
121       xnew=(X20M(i)-controlxx(:,:)).*longCoef;
122       ynew=(Y20M(i)-controly(:,:)).*latCoef;
123       znew=Z20M(i)-imageData1(:,:);
124       if  LIDAR20M(i) > 15
125          droneCounts20 = CPS20M(i);
126          radiusSquared20=(xnew.^2)+ (ynew.^2)+ (znew.^2);
127          radius20 = radiusSquared20.^0.5;
128          A20=(0.5.^(radius20./72))./(radius20.^2);
129          droneCountsEstimate20 = sum(sum(xtwenty .* A20));
130          relativeError20=abs(droneCounts20 -
    droneCountsEstimate20)./droneCounts20;
131          droneResults20(i,:) = [X20M(i), Y20M(i), Z20M(i), droneCounts20,
    droneCountsEstimate20, relativeError20];
132       end
133    end
134
135
136    %%%%%%%%%%%%%%%%%%KACMARZ ALGORTHM 30M
    CALCULATION%%%%%%%%%%%%%%%%%%%
137    for i=1:updates
138       i
139       randomDronePosition = randi([1 droneReadings]);
140       if  LIDAR30M(randomDronePosition) > 25
141          xnew=(X30M(randomDronePosition)-controlxx(:,:)).*longCoef;
142          ynew=(Y30M(randomDronePosition)-controly(:,:)).*latCoef;
143          znew=Z30M(randomDronePosition)-imageData1(:,:);
144          radiusSquared30=(xnew.^2)+ (ynew.^2)+ (znew.^2);
145          radius30 = radiusSquared30.^0.5;
146          A30=(0.5.^(radius30./72))./(radius30.^2);
147          bg=0;
148          randomDroneCounts30 = CPS30M(randomDronePosition);
149          update30= A30.*(randomDroneCounts30 - sum(sum(xthirty .*
    A30))./sum(sum(A30)));
150          xthirty(:,:)=xthirty(:,:)+(damping.*update30);
```

```
151         xthirty(xthirty<bg)=bg;
152       end
153    end
154
155    %%%%%%%%%%%%%%%%%%%%%%%%%%30M RELATIVE
    ERROR%%%%%%%%%%%%%%%%%%%%%%%%%%
156    droneResults30 = zeros(droneReadings, 6);
157    for i=1:droneReadings
158       xnew=(X30M(i)-controlxx(:,:)).*longCoef;
159       ynew=(Y30M(i)-controly(:,:)).*latCoef;
160       znew=Z30M(i)-imageData1(:,:);
161       if  LIDAR30M(i) > 25
162          droneCounts30 = CPS30M(i);
163          radiusSquared30=(xnew.^2)+ (ynew.^2)+ (znew.^2);
164          radius30 = radiusSquared30.^0.5;
165          A30=(0.5.^(radius30./72))./(radius30.^2);
166          droneCountsEstimate30 = sum(sum(xthirty .* A30));
167          relativeError30=abs(droneCounts30 -
    droneCountsEstimate30)./droneCounts30;
168          droneResults30(i,:) = [X30M(i), Y30M(i), Z30M(i), droneCounts30,
    droneCountsEstimate30, relativeError30];
169       end
170    end
171
172
173    %%%%%%%%%%%%%%%%%%%%KACMARZ ALGORTHM 40M
    CALCULATION%%%%%%%%%%%%%%%%%%%%
174    for i=1:updates
175       i
176       randomDronePosition = randi([1 droneReadings]);
177       if  LIDAR40M(randomDronePosition) > 25
178          xnew=(X40M(randomDronePosition)-controlxx(:,:)).*longCoef;
179          ynew=(Y40M(randomDronePosition)-controly(:,:)).*latCoef;
180          znew=Z40M(randomDronePosition)-imageData1(:,:);
181          radiusSquared40=(xnew.^2)+ (ynew.^2)+ (znew.^2);
182          radius40 = radiusSquared40.^0.5;
183          A40=(0.5.^(radius40./72))./(radius40.^2);
184          bg=0;
185          randomDroneCounts40 = CPS40M(randomDronePosition);
186          update40= A40.*(randomDroneCounts40 - sum(sum(xfourty .*
    A40))./sum(sum(A40)));
187          xfourty(:,:)=xfourty(:,:)+(damping.*update40);
188          xfourty(xfourty<bg)=bg;
189       end
190    end
191
192
```

```
193     %%%%%%%%%%%%%%%%%%%%%%%%%%%%40M RELATIVE
    ERROR%%%%%%%%%%%%%%%%%%%%%%%%%%%%
194     droneResults40 = zeros(droneReadings, 6);
195     for i=1:droneReadings
196         xnew=(X40M(i)-controlxx(:,:)).*longCoef;
197         ynew=(Y40M(i)-controly(:,:)).*latCoef;
198         znew=Z40M(i)-imageData1(:,:);
199         if  LIDAR40M(i) > 35
200             droneCounts40 = CPS40M(i);
201             radiusSquared40=(xnew.^2)+ (ynew.^2)+ (znew.^2);
202             radius40 = radiusSquared40.^0.5;
203             A40=(0.5.^(radius40./72))./(radius40.^2);
204             droneCountsEstimate40 = sum(sum(xfourty .* A40));
205             relativeError40=abs(droneCounts40 -
    droneCountsEstimate40)./droneCounts40;
206             droneResults40(i,:) = [X40M(i), Y40M(i), Z40M(i), droneCounts40,
    droneCountsEstimate40, relativeError40];
207         end
208     end
209
210
211     %%%%%%%%%%%%%%%%%%%%%%%%%%%%%%SEPERATELY
    FIGURES%%%%%%%%%%%%%%%%%%%%%%
212     figure(1)
213     subplot(2,2,1)
214     surf(imageData1,xfourty);
215     xlabel('Distance(m)','FontSize',12,'FontWeight','bold','Color','k');
216     ylabel('Distance(m)','FontSize',12,'FontWeight','bold','Color','k');
217     title('FL40 ART Result','FontSize',12,'FontWeight','bold','Color','k');
218     fig1=colorbar;
219     title(fig1,'Inverted Total Counts(cps)','FontSize',12,'FontWeight','bold','Color','k')
220     subplot(2,2,2)
221     surf(imageData1,xthirty);
222     title('FL30 ART Result','FontSize',12,'FontWeight','bold','Color','k');
223     xlabel('Distance(m)','FontSize',12,'FontWeight','bold','Color','k');
224     ylabel('Distance(m)','FontSize',12,'FontWeight','bold','Color','k');
225     fig2=colorbar;
226     title(fig2,'Inverted Total Counts(cps)','FontSize',12,'FontWeight','bold','Color','k')
227     subplot(2,2,3)
228     surf(imageData1,xtwenty);
229     fig3=colorbar;
230     title(fig3,'Inverted Total Counts(cps)','FontSize',12,'FontWeight','bold','Color','k')
231     title('FL20 ART Result','FontSize',12,'FontWeight','bold','Color','k');
232     xlabel('Distance(m)','FontSize',12,'FontWeight','bold','Color','k');
233     ylabel('Distance(m)','FontSize',12,'FontWeight','bold','Color','k');
234     subplot(2,2,4)
235     surf(imageData1,xfifteen);
236     title('FL15 ART Result','FontSize',12,'FontWeight','bold','Color','k');
```

```
237     xlabel('Distance(m)','FontSize',12,'FontWeight','bold','Color','k');
238     ylabel('Distance(m)','FontSize',12,'FontWeight','bold','Color','k');
239     fig4=colorbar;
240     title(fig4,'Inverted Total Counts(cps)','FontSize',12,'FontWeight','bold','Color','k')
241
242     figure(2)
243     subplot(2,2,1)
244     histogram(droneResults40(:,6))
245     title('FL40','FontSize',12,'FontWeight','bold','Color','k');
246     ylabel('Number of Inverted Total
    Counts','FontSize',12,'FontWeight','bold','Color','k');
247     xlabel('Relative Error','FontSize',12,'FontWeight','bold','Color','k');
248     subplot(2,2,2)
249     histogram(droneResults30(:,6))
250     title('FL30','FontSize',12,'FontWeight','bold','Color','k');
251     ylabel('Number of Inverted Total
    Counts','FontSize',12,'FontWeight','bold','Color','k');
252     xlabel('Relative Error','FontSize',12,'FontWeight','bold','Color','k');
253     subplot(2,2,3)
254     histogram(droneResults20(:,6))
255     title('FL20','FontSize',12,'FontWeight','bold','Color','k');
256     ylabel('Number of Inverted Total
    Counts','FontSize',12,'FontWeight','bold','Color','k');
257     xlabel('Relative Error','FontSize',12,'FontWeight','bold','Color','k');
258     subplot(2,2,4)
259     histogram(droneResults15(:,6))
260     title('FL15','FontSize',12,'FontWeight','bold','Color','k');
261     ylabel('Number of Inverted Total
    Counts','FontSize',12,'FontWeight','bold','Color','k');
262     xlabel('Relative Error','FontSize',12,'FontWeight','bold','Color','k');
263
264
265     %%%%%%%%%%%%%%%%%%%%%%%%%%%%COMBINED
    FIGURES%%%%%%%%%%%%%%%%%%%%%%%%%%%%
266     %%%%%%%%%%%%%%%%KACMARZ ALGORTHM 40M+30M
    CALCULATION%%%%%%%%%%%%%%%%%%%%
267     CPS30M=imresize(CPS30M,[unknowns 1]);
268     X30M=imresize(X30M,[unknowns 1]);
269     Y30M=imresize(Y30M,[unknowns 1]);
270     Z30M=imresize(Z30M,[unknowns 1]);
271     LIDAR30M=imresize(LIDAR30M,[unknowns 1]);
272     X4030M=[X40M;X30M];
273     Y4030M=[Y40M;Y30M];
274     Z4030M=[Z40M;Z30M];
275     CPS4030M=[CPS40M;CPS30M];
276     LIDAR4030M=[LIDAR40M;LIDAR30M];
277
278     %%%%%%%%%%
```

```
279     for i=1:updates
280         i
281         randomDronePosition = randi([1 droneReadings]);
282         if  LIDAR4030M(randomDronePosition) > 25
283             xnew=(X4030M(randomDronePosition)-controlxx(:,:)).*longCoef;
284             ynew=(Y4030M(randomDronePosition)-controly(:,:)).*latCoef;
285             znew= Z4030M(randomDronePosition)-imageData1(:,:);
286             radiusSquared4030=(xnew.^2)+ (ynew.^2)+ (znew.^2);
287             radius4030 = radiusSquared4030.^0.5;
288             A4030=(0.5.^(radius4030./72))./(radius4030.^2);
289             bg=0;
290             randomDroneCounts4030 = CPS4030M(randomDronePosition);
291             update4030= A4030.*(randomDroneCounts4030 - sum(sum(xfourtythirty .*
    A4030))./sum(sum(A4030)));
292             xfourtythirty(:,:)=xfourtythirty(:,:)+(damping.*update4030);
293             xfourtythirty(xfourtythirty<bg)=bg;
294         end
295     end
296
297
298     %%%%%%%%%%KACMARZ ALGORTHM 40M+30M+20M
    CALCULATION%%%%%%%%%%%%%%%%%%
299     X403020M=[X40M;X30M;X20M];
300     Y403020M=[Y40M;Y30M;Y20M];
301     Z403020M=[Z40M;Z30M;Z20M];
302     CPS403020M=[CPS40M;CPS30M;CPS20M];
303     LIDAR403020M=[LIDAR40M;LIDAR30M;LIDAR20M];
304     for i=1:updates
305         i
306         randomDronePosition = randi([1 droneReadings]);
307         if  LIDAR403020M(randomDronePosition) > 15
308             xnew=(X403020M(randomDronePosition)-controlxx(:,:)).*longCoef;
309             ynew=(Y403020M(randomDronePosition)-controly(:,:)).*latCoef;
310             znew= Z403020M(randomDronePosition)-imageData1(:,:);
311             radiusSquared403020=(xnew.^2)+ (ynew.^2)+ (znew.^2);
312             radius403020 = radiusSquared403020.^0.5;
313             A403020=(0.5.^(radius403020./72))./(radius403020.^2);
314             bg=0;
315             randomDroneCounts403020 = CPS403020M(randomDronePosition);
316             update403020= A403020.*(randomDroneCounts403020 -
    sum(sum(xfourtythirtytwenty .* A403020))./sum(sum(A403020)));
317
    xfourtythirtytwenty(:,:)=xfourtythirtytwenty(:,:)+(damping.*update403020);
318             xfourtythirtytwenty(xfourtythirtytwenty<bg)=bg;
319         end
320     end
321
322     % %
```

```
323     %KACMARZ ALGORTHM 40M+30M+20M+15M CALCULATION%%%%%%
324     % X40302015M=[X40M;X30M;X20M;VarName5];
325     % Y40302015M=[Y40M;Y30M;Y20M;VarName4];
326     % Z40302015M=[Z40M;Z30M;Z20M;VarName7];
327     % CPS40302015M=[CPS40M;CPS30M;CPS20M;VarName9];
328     % LIDAR40302015M=[LIDAR40M;LIDAR30M;LIDAR20M;VarName2];
329     for i=1:updates
330       i
331       randomDronePosition = randi([1 droneReadings]);
332       if  LIDAR40302015M(randomDronePosition) > 10
333         xnew=(X40302015M(randomDronePosition)-controlxx(:,:)).*longCoef;
334         ynew=(Y40302015M(randomDronePosition)-controly(:,:)).*latCoef;
335         znew= Z40302015M(randomDronePosition)-imageData1(:,:);
336         radiusSquared40302015=(xnew.^2)+ (ynew.^2)+ (znew.^2);
337         radius40302015 = radiusSquared40302015.^0.5;
338         A40302015=(0.5.^(radius40302015./72))./(radius40302015.^2);
339         bg=0;
340         randomDroneCounts40302015 = CPS40302015M(randomDronePosition);
341         update40302015= A40302015.*(randomDroneCounts40302015 -
    sum(sum(xfourtythirtytwentyfifteen .* A40302015))./sum(sum(A40302015)));
342
    xfourtythirtytwentyfifteen(:,:)=xfourtythirtytwentyfifteen(:,:)+(damping.*update40
    302015);
343         xfourtythirtytwentyfifteen(xfourtythirtytwentyfifteen<bg)=bg;
344       end
345     end
346
347     %COMBINED 40302015M RELATIVE ERROR%%%%%%%%%%%%%%%%
348     droneResults40302015 = zeros(droneReadings, 6);
349     for i=1:droneReadings
350       xnew=(X40302015M(i)-controlxx(:,:)).*longCoef;
351       ynew=(Y40302015M(i)-controly(:,:)).*latCoef;
352       znew=Z40302015M(i)-imageData1(:,:);
353       if  LIDAR40302015M(i) > 10
354         droneCounts40302015 = CPS40302015M(i);
355         radiusSquared40302015=(xnew.^2)+ (ynew.^2)+ (znew.^2);
356         radius40302015 = radiusSquared40302015.^0.5;
357         A40302015=(0.5.^(radius40302015./72))./(radius40302015.^2);
358         droneCountsEstimate40302015 = sum(sum(xfourtythirtytwentyfifteen .*
    A40302015));
359         relativeError40302015=abs(droneCounts40302015 -
    droneCountsEstimate40302015)./droneCounts40302015;
360         droneResults40302015(i,:) = [X40302015M(i), Y40302015M(i),
    Z40302015M(i), droneCounts40302015, droneCountsEstimate40302015,
    relativeError40302015];
361       end
362     end
```

```
%%%%COMBINED FIGURES%%%%%%%%%%%%%%%%%%%%%%
figure(2)
subplot(1,3,1)
surf(imageData1,xfourtythirty);
xlabel('Distance(m)','FontSize',12,'FontWeight','bold','Color','k');
ylabel('Distance(m)','FontSize',12,'FontWeight','bold','Color','k');
title('FL40+FL30 ART Result','FontSize',12,'FontWeight','bold','Color','k');
fig1=colorbar;
colormap('hot');
title(fig1,'Inverted Total Counts(cps)','FontSize',12,'FontWeight','bold','Color','k')
subplot(1,3,2)
surf(imageData1,xfourtythirtytwenty);
title('FL40+FL30+FL20 ART Result','FontSize',12,'FontWeight','bold','Color','k');
xlabel('Distance(m)','FontSize',12,'FontWeight','bold','Color','k');
ylabel('Distance(m)','FontSize',12,'FontWeight','bold','Color','k');
fig2=colorbar;
colormap('hot');
title(fig2,'Inverted Total Counts(cps)','FontSize',12,'FontWeight','bold','Color','k')
subplot(1,3,3)
surf(imageData1,xfourtythirtytwentyfifteen);
fig3=colorbar;
colormap('hot');
title('FL40+FL30+FL20+FL15 ART
Result','FontSize',12,'FontWeight','bold','Color','k');
xlabel('Distance(m)','FontSize',12,'FontWeight','bold','Color','k');
ylabel('Distance(m)','FontSize',12,'FontWeight','bold','Color','k');

%%%%%%%%%%%%%%%%%%%%%%%%%%%%
figure(3)
subplot(1,2,1)
surf(imageData1,xfifteen);
fig1=colorbar;
colormap('hsv');
title(fig1,'Inverted Total Counts(cps)','FontSize',12,'FontWeight','bold','Color','k')
xlabel('Distance(m)','FontSize',12,'FontWeight','bold','Color','k');
ylabel('Distance(m)','FontSize',12,'FontWeight','bold','Color','k');
title('FL15 Inversion Result','FontSize',12,'FontWeight','bold','Color','k');
subplot(1,2,2)
surf(imageData1,xfourtythirtytwentyfifteen);
fig2=colorbar;
colormap('hsv');
title(fig2,'Inverted Total Counts(cps)','FontSize',12,'FontWeight','bold','Color','k')
title('FL40+FL30+FL20+FL15 Inversion
Result','FontSize',12,'FontWeight','bold','Color','k');
xlabel('Distance(m)','FontSize',12,'FontWeight','bold','Color','k');
ylabel('Distance(m)','FontSize',12,'FontWeight','bold','Color','k');

```

```
figure(4)
subplot(1,2,1)
histogram(droneResults15(:,6))
title('FL15','FontSize',12,'FontWeight','bold','Color','k');
ylabel('Number of Inverted Total
Counts','FontSize',12,'FontWeight','bold','Color','k');
xlabel('Relative Error','FontSize',12,'FontWeight','bold','Color','k');
subplot(1,2,2)
histogram(droneResults40302015(:,6))
title('FL40+FL30+FL20+FL15 ','FontSize',12,'FontWeight','bold','Color','k');
ylabel('Number of Inverted Total
Counts','FontSize',12,'FontWeight','bold','Color','k');
xlabel('Relative Error','FontSize',12,'FontWeight','bold','Color','k');
```

1.3. Full Inversion Process with HSGI Technique

```
clc;
clear all;
format long
load FIXEDWING1LIDARLATLONGAMGLCOUNTS;
load FIXEDWING2LIDARLATLONGAMGLCOUNTS;
load MULTIROTOR15MLIDARLATLONGAMGLCOUNTS;
load MULTIROTOR20MLIDARLATLONGAMGLCOUNTS;
load MULTIROTOR30MLIDARLATLONGAMGLCOUNTS;
load MULTIROTOR40MLIDARLATLONGAMGLCOUNTS;
load WHOLEDATAMULTIROTOR15M.mat;
load WHOLEDATAMULTIROTOR20M.mat;
load WHOLEDATAMULTIROTOR30M.mat;
load WHOLEDATAMULTIROTOR40M.mat;
load EACHCHANNELTOTALCOUNTS15.mat;
load EACHCHANNELTOTALCOUNTS20.mat;
load EACHCHANNELTOTALCOUNTS30.mat;
load EACHCHANNELTOTALCOUNTS40.mat;
load EACHCHANNELTOTALCOUNTSFIXEDWING1.mat;
load EACHCHANNELTOTALCOUNTSFIXEDWING2.mat;
load LASTMU.mat;
%%%%UAV COEFFICIENT FROM WGS84 TO UTM%%%%%%%%%%%%%
latCoef = 114491.8497;  %lat m/deg
longCoef = 71795.30699; %long m/deg

%BIG KOBACHI DEM DATA INPUT%%%%%%%%%%%%%%%%%%%%
LatRange2=51.3480:-0.0000141891:51.3417;
LongRange2=30.1064:1.55405e-05:30.1133;
z=[110:0.0202702702:119];
imageData2=repmat(z,445,1)';
control2x=repmat(LatRange2,445,1);
control2y=repmat(LongRange2,445,1);
NW = 111;
```

```
451     NE = 111;
452     SE = 117;
453     SW = 119;
454     XPixels = 445;
455
456     %KACMARZ ALGORTHM BIG KOBACHI INPUT%%%%%%%%%%%%%%
457     xkobachi= zeros(XPixels,XPixels);
458     kobachiy=[MULTIROTOR20MLIDARLATLONGAMGLCOUNTS(500:7000,2);MULT
        IROTOR30MLIDARLATLONGAMGLCOUNTS(866:7200,2);MULTIROTOR40MLIDARL
        ATLONGAMGLCOUNTS(253:6570,2);FIXEDWING1LIDARLATLONGAMGLCOUNTS(1
        700:2069,2);FIXEDWING2LIDARLATLONGAMGSLCOUNTS(1700:2069,2)];
459     kobachix=[MULTIROTOR20MLIDARLATLONGAMGLCOUNTS(500:7000,3);MULT
        IROTOR30MLIDARLATLONGAMGLCOUNTS(866:7200,3);MULTIROTOR40MLIDARL
        ATLONGAMGLCOUNTS(253:6570,3);FIXEDWING1LIDARLATLONGAMGLCOUNTS(1
        700:2069,3);FIXEDWING2LIDARLATLONGAMGSLCOUNTS(1700:2069,3)];
460     kobachiz=[MULTIROTOR20MLIDARLATLONGAMGLCOUNTS(500:7000,4);MULT
        IROTOR30MLIDARLATLONGAMGLCOUNTS(866:7200,4);MULTIROTOR40MLIDARL
        ATLONGAMGLCOUNTS(253:6570,4);FIXEDWING1LIDARLATLONGAMGLCOUNTS(1
        700:2069,4);FIXEDWING2LIDARLATLONGAMGSLCOUNTS(1700:2069,4)];
461     CPSKOBACHI=[MULTIROTOR20MLIDARLATLONGAMGLCOUNTS(500:7000,5);M
        ULTIROTOR30MLIDARLATLONGAMGLCOUNTS(866:7200,5);MULTIROTOR40MLID
        ARLATLONGAMGLCOUNTS(253:6570,5);FIXEDWING1LIDARLATLONGAMGLCOUN
        TS(1700:2069,5);FIXEDWING2LIDARLATLONGAMGSLCOUNTS(1700:2069,5)];
462     Lidarkobachi=[MULTIROTOR20MLIDARLATLONGAMGLCOUNTS(500:7000,1);M
        ULTIROTOR30MLIDARLATLONGAMGLCOUNTS(866:7200,1);MULTIROTOR40MLID
        ARLATLONGAMGLCOUNTS(253:6570,1);FIXEDWING1LIDARLATLONGAMGLCOUN
        TS(1700:2069,1);FIXEDWING2LIDARLATLONGAMGSLCOUNTS(1700:2069,1)];
463     Eachchannelcounts=[EACHCHANNELTOTALCOUNTS20(:,:);EACHCHANNELTOT
        ALCOUNTS30(:,:);EACHCHANNELTOTALCOUNTS40(:,:);EACHCHANNELTOTALCOU
        NTSFIXEDWING1(:,:);EACHCHANNELTOTALCOUNTSFIXEDWING2(:,:)];
464     kobachiy=[MULTIROTOR15MLIDARLATLONGAMGLCOUNTS(300:7350,2);MULT
        IROTOR20MLIDARLATLONGAMGLCOUNTS(500:7000,2);MULTIROTOR30MLIDARL
        ATLONGAMGLCOUNTS(866:7200,2);MULTIROTOR40MLIDARLATLONGAMGLCOUN
        TS(253:6570,2);FIXEDWING1LIDARLATLONGAMGLCOUNTS(1700:2069,2);FIXED
        WING2LIDARLATLONGAMGSLCOUNTS(1700:2069,2)];
465     kobachix=[MULTIROTOR15MLIDARLATLONGAMGLCOUNTS(300:7350,3);MULT
        IROTOR20MLIDARLATLONGAMGLCOUNTS(500:7000,3);MULTIROTOR30MLIDARL
        ATLONGAMGLCOUNTS(866:7200,3);MULTIROTOR40MLIDARLATLONGAMGLCOUN
        TS(253:6570,3);FIXEDWING1LIDARLATLONGAMGLCOUNTS(1700:2069,3);FIXED
        WING2LIDARLATLONGAMGSLCOUNTS(1700:2069,3)];
466     kobachiz=[MULTIROTOR15MLIDARLATLONGAMGLCOUNTS(300:7350,4);MULT
        IROTOR20MLIDARLATLONGAMGLCOUNTS(500:7000,4);MULTIROTOR30MLIDARL
        ATLONGAMGLCOUNTS(866:7200,4);MULTIROTOR40MLIDARLATLONGAMGLCOUN
        TS(253:6570,4);FIXEDWING1LIDARLATLONGAMGLCOUNTS(1700:2069,4);FIXED
        WING2LIDARLATLONGAMGSLCOUNTS(1700:2069,4)];
467     CPSKOBACHI=[MULTIROTOR15MLIDARLATLONGAMGLCOUNTS(300:7350,5);M
        ULTIROTOR20MLIDARLATLONGAMGLCOUNTS(500:7000,5);MULTIROTOR30MLID
        ARLATLONGAMGLCOUNTS(866:7200,5);MULTIROTOR40MLIDARLATLONGAMGLC
```

```
OUNTS(253:6570,5);FIXEDWING1LIDARLATLONGAMGLCOUNTS(1700:2069,5);FIX
EDWING2LIDARLATLONGAMGSLCOUNTS(1700:2069,5)];
468     Lidarkobachi=[MULTIROTOR15MLIDARLATLONGAMGLCOUNTS(300:7350,1);M
ULTIROTOR20MLIDARLATLONGAMGLCOUNTS(500:7000,1);MULTIROTOR30MLID
ARLATLONGAMGLCOUNTS(866:7200,1);MULTIROTOR40MLIDARLATLONGAMGLC
OUNTS(253:6570,1);FIXEDWING1LIDARLATLONGAMGLCOUNTS(1700:2069,1);FIX
EDWING2LIDARLATLONGAMGSLCOUNTS(1700:2069,1)];
469     Eachchannelcounts=[EACHCHANNELTOTALCOUNTS15(:,:);EACHCHANNELTOT
ALCOUNTS20(:,:);EACHCHANNELTOTALCOUNTS30(:,:);EACHCHANNELTOTALCOU
NTS40(:,:);EACHCHANNELTOTALCOUNTSFIXEDWING1(:,:);EACHCHANNELTOTALC
OUNTSFIXEDWING2(:,:)];
470     squeezeFactor = 16;
471     newChannelLength = length(Eachchannelcounts(1,:))/squeezeFactor;
472     channels = 1:4096;
473     Energies = (0.00000002.*(channels.^2))+(0.0003.*channels)+0.0104;
474     for nn=1:newChannelLength
475         squeezedChannel=sum(Eachchannelcounts(:,(nn-
    1)*squeezeFactor+1:nn*squeezeFactor),2);
476         ChannelCountsSqueezed(:,nn) = squeezedChannel;
477         MuSqueezed(nn) = mean(N15((nn-1)*squeezeFactor+1:nn*squeezeFactor));
478         EnergiesSqueezed(nn) = mean(Energies((nn-
    1)*squeezeFactor+1:nn*squeezeFactor));
479
480     end
481
482     Xmax = max(kobachix);
483     Xmin = min(kobachix);
484     Ymax = max(kobachiy);
485     Ymin = min(kobachiy);
486     [control2x,control2y] = meshgrid(Xmin:(Xmax - Xmin)./(XPixels-1):Xmax,...
487                     Ymin:(Ymax - Ymin)./(XPixels-1):Ymax);
488     control2y = flip(control2y,1);
489
490     [Xmesh,Ymesh] = meshgrid(0:(Xmax - Xmin).*longCoef/(XPixels-1):(Xmax -
    Xmin).*longCoef,...
491                     0:(Ymax - Ymin).*latCoef/(XPixels-1):(Ymax - Ymin).*latCoef);
492     Ymesh = flip(Ymesh,1);
493     Xrange = (Xmax - Xmin).*longCoef;
494     Yrange = (Ymax - Ymin).*latCoef;
495
496     imageData2 = Xmesh.*((Ymesh/Yrange).*(NE+SW-SE-NW)+SE-SW)./Xrange +
    (Ymesh/Yrange).*(NW-SW)+SW;
497
498
499     mu=N15;
500     a=size(xkobachi);
501     unknowns2=a(:,1)*a(:,2);
502     updates2 = 150000;
```

```
503     damping2=0.05;
504     droneReadings2 = length(kobachix);
505     probabilities = zeros(size(droneReadings2));
506     heights = [15,20,30,40,6,6];
507     minimumHeights = heights - 5;
508     datasetEdges = cumsum(
    [length(MULTIROTOR15MLIDARLATLONGAMGLCOUNTS(:,2)),
    length(MULTIROTOR20MLIDARLATLONGAMGLCOUNTS(:,2)),
    length(MULTIROTOR30MLIDARLATLONGAMGLCOUNTS(:,2)),
    length(MULTIROTOR40MLIDARLATLONGAMGLCOUNTS(:,2)), ...
509                     length(FIXEDWING1LIDARLATLONGAMGLCOUNTS(:,2)),
    length(FIXEDWING2LIDARLATLONGAMGSLCOUNTS(:,2))]);
510     dataset = 1;
511       for dronePos=1:droneReadings2
512         xnew2=(kobachix(dronePos)-control2x(:,:)').*longCoef;
513         ynew2=(kobachiy(dronePos)-control2y(:,:)).*latCoef;
514         znew2=kobachiz(dronePos)-imageData2(:,:);
515         radiusSquared2=(xnew2.^2)+ (ynew2.^2)+ (znew2.^2);
516         radius2 = radiusSquared2.^0.5;
517         A2=(exp(radius2.*mu)./(radius2.^2);
518         prob = sum(sum(A2));
519         if dronePos > datasetEdges(dataset)
520           dataset = dataset + 1;
521         end
522         if or(Lidarkobachi(dronePos) < minimumHeights(dataset), dataset==6)
523           prob = 0;
524         end
525         if isnan(prob)
526           prob = 0;
527         end
528           probabilities(dronePos)= prob;
529       end
530     probabilities = probabilities./sum(probabilities);
531     randomDronePositions = randsrc(updates2, 1, [1:1:droneReadings2;
    probabilities]);
532
533     %KACMARZ ALGORTHM KOBACHI WHOLE AREA CALCULATION%%%%%%
534     hypercube = zeros(16,445,445);
535     droneResults2= zeros(16, droneReadings2, 6);
536
537     loop through all the channels
538     parfor
539
540     workers = 12; %make this zero for laptop testing or 16 for bluecrystal
541     parfor (channel = 1:16,workers)
542     for channel = 15:16
543       lookup the mu value for this channel
544       mu = 100*MuSqueezed(channel);
```

```
545       xkobachi = zeros(445,445);
546       calculate the probabilities for this mu value
547          dataset = 1;
548          for dronePos=1:droneReadings2
549             xnew2=(kobachix(dronePos)-control2x(:,:)').*longCoef;
550             ynew2=(kobachiy(dronePos)-control2y(:,:)).*latCoef;
551             znew2=kobachiz(dronePos)-imageData2(:,:);
552             radiusSquared2=(xnew2.^2)+ (ynew2.^2)+ (znew2.^2);
553             radius2 = radiusSquared2.^0.5;
554             A2=(exp(radius2.*mu)./(radius2.^2);
555             prob = sum(sum(A2));
556             if dronePos > datasetEdges(dataset)
557                dataset = dataset + 1;
558             end
559             if or(Lidarkobachi(dronePos) < minimumHeights(dataset), dataset==6)
560                prob = 0;
561             end
562             if isnan(prob)
563                prob = 0;
564             end
565                probabilities(dronePos)= prob;
566          end
567          probabilities = probabilities./sum(probabilities);
568          randomDronePositions = randsrc(updates2, 1, [1:1:droneReadings2;
    probabilities]);
569
570
571       for i=1:updates2
572          randomDronePosition = randomDronePositions(i);
573          randomDronePosition = randi([1 droneReadings2]);
574          xnew2=(kobachix(randomDronePosition)-control2x).*longCoef;
575          ynew2=(kobachiy(randomDronePosition)-control2y).*latCoef;
576          znew2=kobachiz(randomDronePosition)-imageData2;
577          radiusSquared2=(xnew2.^2)+ (ynew2.^2)+ (znew2.^2);
578          radius2 = radiusSquared2.^0.5;
579          A2=(exp(-radius2.*mu)).(radius2.^2);
580          bg2=0.0001;
581          randomDroneCounts2 = Eachchannelcounts(randomDronePosition,
    channel);
582          update2= A2.*(randomDroneCounts2 - sum(sum(xkobachi .*
    A2))./sum(sum(A2)));
583          xkobachi(:,:)=xkobachi(:,:)+(damping2.*update2);
584          xkobachi(xkobachi<bg2)=bg2;
585          if mod(i,100) == 0
586             status = [i, channel, randomDronePosition,
    kobachiz(randomDronePosition)]
587          end
588       end
```

```
589
590         hypercube(channel,:,:) = xkobachi;
591         droneResults_temp = zeros(droneReadings2, 6);
592         for i=1:droneReadings2
593             xnew2=(kobachix(i)-control2x).*longCoef;
594             ynew2=(kobachiy(i)-control2y).*latCoef;
595             znew2=kobachiz(i)-imageData2;
596             droneCounts2 = Eachchannelcounts(i, channel);
597             radiusSquared2=(xnew2.^2)+ (ynew2.^2)+ (znew2.^2);
598             radius2 = radiusSquared2.^0.5;
599             A2=(exp(-radius2.*mu))./(radius2.^2);
600             droneCountsEstimate2 = sum(sum(xkobachi .* A2));
601             relativeError2=abs(droneCounts2 - droneCountsEstimate2)./droneCounts2;
602             droneResults_temp(i,:) = [kobachix(i), kobachiy(i), kobachiz(i),
    droneCounts2, droneCountsEstimate2, relativeError2];
603         end
604         droneResults2(channel,:,:) = droneResults_temp;
605
606     end
607
608     save('Results','hypercube','droneResults2');
609
610     quit
611
612     %%%%%%%%RESULTS INTERPRETATION%%%%%%%%%%%%%%%%%%
613     figure (1)
614     subplot(4,4,1)
615     imagesc(squeeze(hypercube(1,:,:)))
616     title('0.01 MeV 0.09 MeV')
617     subplot(4,4,2)
618     imagesc(squeeze(hypercube(2,:,:)))
619     title('0.09 MeV 0.17 MeV')
620     subplot(4,4,3)
621     imagesc(squeeze(hypercube(3,:,:)))
622     title('0.17 MeV 0.25 MeV')
623     subplot(4,4,4)
624     imagesc(squeeze(hypercube(4,:,:)))
625     title('0.25 MeV 0.34 MeV')
626     subplot(4,4,5)
627     imagesc(squeeze(hypercube(5,:,:)))
628     title('0.34 MeV 0.43 MeV')
629     subplot(4,4,6)
630     imagesc(squeeze(hypercube(6,:,:)))
631     title('0.43 MeV 0.52 MeV')
632     subplot(4,4,7)
633     imagesc(squeeze(hypercube(7,:,:)))
634     title('0.52 MeV 0.61 MeV')
635     subplot(4,4,8)
```

```
636     imagesc(squeeze(hypercube(8,:,:)))
637     title('0.61 MeV 0.71 MeV')
638     subplot(4,4,9)
639     imagesc(squeeze(hypercube(9,:,:)))
640     title('0.71 MeV 0.81 MeV')
641     subplot(4,4,10)
642     imagesc(squeeze(hypercube(10,:,:)))
643     title('0.81 MeV 0.91 MeV')
644     subplot(4,4,11)
645     imagesc(squeeze(hypercube(11,:,:)))
646     title('0.91 MeV 1.01 MeV')
647     subplot(4,4,12)
648     imagesc(squeeze(hypercube(12,:,:)))
649     title('1.01 MeV 1.12 MeV')
650     subplot(4,4,13)
651     imagesc(squeeze(hypercube(13,:,:)))
652     title('1.12 MeV 1.23 MeV')
653     subplot(4,4,14)
654     imagesc(squeeze(hypercube(14,:,:)))
655     title('1.23 MeV 1.34 MeV')
656     subplot(4,4,15)
657     imagesc(squeeze(hypercube(15,:,:)))
658     title('1.34 MeV 1.46 MeV')
659     subplot(4,4,16)
660     imagesc(squeeze(hypercube(16,:,:)))
661     title('1.46 MeV 1.57 MeV')
662
```

1.4. Energy Calibration

```
1.  clc;
2.  clear all;
3.  format long;
4.  load NEWENERGYCHANNELFIXEDWING.mat;
5.  load FIXEDWING1LIDARLATLONGAMGLCOUNTS.mat;
6.  load droneResults15.mat;
7.
8.  % %load new_x.dat;
9.  airrofixedwing1=0.0012341;
10. channelnumber=1:4096;
11. distance=7200;
12. % CHANNELFIXEDWING1=NEWENERGYCHANNELFIXEDWING(:,2:2:end);
13. energy=(0.00000002.*(channelnumber.^2))+(0.0003.*channelnumber)+0.0104;
14. LOGE=log10(energy);
15. n1=(-LOGE).^0;
16. n2=(-LOGE).^1;
17. n3=(-LOGE).^2;
```

```
n4=(-LOGE).^3;
n5=(-LOGE).^4;
an1=-1.1945.*n1;
an2=0.49234.*n2;
an3=-0.12414.*n3;
an4=-0.056958.*n4;
an5=0.061026.*n5;
sum=an1+an2+an3+an4+an5;
muro=10.^sum;
mufixedwing1=muro.*airrofixedwing1;
dimensionmufixedwing1=size(mufixedwing1);
attenuationfixedwing1=exp(-airrofixedwing1.*distance.*muro);
```

1.5. Calculator for Energy Calibration in Excel format

E (mev)	0.05						
an	-1.1945	0.49234	-0.12414	-0.056958	0.061026		
n	0	1	2	3	4		
log10(E)	-1.301029996	-1.30103	-1.30103	-1.30103	-1.30103		
-log10(E)^n	1	1.30103	1.69267905	2.20222622	2.86516237		log10(mu/density)
an*(-log10(E))^n	-1.1945	0.64054911	-0.21012918	-0.1254344	0.1748494	=	-0.714665072
						mu/density	0.1929012
						mu	0.00023804
						distance (m)	72
						distance (cm)	7200
						density	0.001234
						attenuation	18.02%
CALCULATIONS							
RESULTS							
INPUTS							

1.6. Interpolation for radiation intensity in Kobachi Weighbridge

```
Q=300;
A=Tiff('smallkobachi.tif');
imageData2=read(A)+132;
imageData2(imageData2==-32635)=120.1325;
imageData2=imageData2';
imageData2=imresize(imageData2,[300 300]);

X1min = min(VarName5);
X1max = max(VarName5);
X2min = min(VarName4);
X2max = max(VarName4);
[X1int,X2int] = meshgrid(X1min:(X1max - X1min)/(Q-1):X1max,...
                         X2min:(X2max - X2min)/(Q-1):X2max);
F1=idw([VarName5(:,1),VarName4(:,1)],VarName9,[X1int(:),X2int(:)],1,inf,24) ;
F2=idw([X20M(:,1),Y20M(:,1)],CPS20M,[X1int(:),X2int(:)],1,inf,24) ;
F3=idw([X30M(:,1),Y30M(:,1)],CPS30M,[X1int(:),X2int(:)],1,inf,24) ;
F4=idw([X40M(:,1),Y40M(:,1)],CPS40M,[X1int(:),X2int(:)],1,inf,24) ;
```

```
figure(6)
imagesc(imageData2)
[c,h2]=contourf(X1int,X2int,reshape(F1,Q,Q),50);
colorbar
colormap('jet');
h2.ContourZLevel = 15;
hold on
[d,h3]=contourf(X1int,X2int,reshape(F2,Q,Q),50);
colorbar
colormap('jet');
h3.ContourZLevel = 140;
hold on
[e,h4]=contourf(X1int,X2int,reshape(F3,Q,Q),50);
colorbar
colormap('jet');
h4.ContourZLevel = 150;
hold on
[f,h5]=contourf(X1int,X2int,reshape(F4,Q,Q),50);
colorbar
colormap('jet');
h5.ContourZLevel = 160;
xlabel({'Longitude X(m)'},'FontWeight','bold','FontSize',12,...
    'FontName','Cambria');
ylabel({'Latitude  Y(m)'},'FontWeight','bold','FontSize',12,...
    'FontName','Cambria');
zlabel({'Height Z(m)'},'FontWeight','bold','FontSize',12,...
    'FontName','Cambria');
title({'Total Counts (cps)'},'FontSize',12,'FontName','Cambria');
```

1.7. Interpolation for radiation intensity in Kobachi Mechanical Yard

```
clc;
clear all;
load MULTIROTOR15MLIDARLATLONGAMGLCOUNTS;
load MULTIROTOR20MLIDARLATLONGAMGLCOUNTS;
load MULTIROTOR30MLIDARLATLONGAMGLCOUNTS;
load MULTIROTOR40MLIDARLATLONGAMGLCOUNTS;
GROUNDDATA = csvread('INTERPOLATIONGROUNDDATA.csv');
longCoef = 71795.30699;
latCoef = 114491.8497;

MULTIROTOR15MLIDARLATLONGAMGLCOUNTS(:,1)=MULTIROTOR15MLIDARLA
TLONGAMGLCOUNTS(:,5)/exp(-0.00710*14);
MULTIROTOR20MLIDARLATLONGAMGLCOUNTS(:,1)=MULTIROTOR20MLIDARLA
TLONGAMGLCOUNTS(:,5)/exp(-0.00710*19);
MULTIROTOR30MLIDARLATLONGAMGLCOUNTS(:,1)=MULTIROTOR30MLIDARLA
TLONGAMGLCOUNTS(:,5)/exp(-0.00710*29);
```

```
15. MULTIROTOR40MLIDARLATLONGAMGLCOUNTS(:,1)=MULTIROTOR40MLIDARLA
    TLONGAMGLCOUNTS(:,5)/exp(-0.00710*39);
16.
17. BIGDATA=[[GROUNDDATA(:,1);MULTIROTOR15MLIDARLATLONGAMGLCOUNTS(3
    00:7350,2);MULTIROTOR20MLIDARLATLONGAMGLCOUNTS(500:7000,2);MULTIR
    OTOR30MLIDARLATLONGAMGLCOUNTS(866:7200,2);MULTIROTOR40MLIDARLA
    TLONGAMGLCOUNTS(253:6570,2)],[GROUNDDATA(:,2);MULTIROTOR15MLIDARL
    ATLONGAMGLCOUNTS(300:7350,3);MULTIROTOR20MLIDARLATLONGAMGLCOU
    NTS(500:7000,3);MULTIROTOR30MLIDARLATLONGAMGLCOUNTS(866:7200,3);M
    ULTIROTOR40MLIDARLATLONGAMGLCOUNTS(253:6570,3)],...
18.
    [GROUNDDATA(:,4);MULTIROTOR15MLIDARLATLONGAMGLCOUNTS(300:7350,1);
    MULTIROTOR20MLIDARLATLONGAMGLCOUNTS(500:7000,1);MULTIROTOR30ML
    IDARLATLONGAMGLCOUNTS(866:7200,1);MULTIROTOR40MLIDARLATLONGAMG
    LCOUNTS(253:6570,1)]];
19.
20.
21. BIGDATA(:,1) = (BIGDATA(:,1) - min(BIGDATA(:,1))).*longCoef;
22. BIGDATA(:,2) = (BIGDATA(:,2) - min(BIGDATA(:,2))).*latCoef;
23.
24.
25. X1min = min(BIGDATA(:,1));
26. X1max = max(BIGDATA(:,1));
27. X2min = min(BIGDATA(:,2));
28. X2max = max(BIGDATA(:,2));
29.
30. [X1int,X2int] = meshgrid(0:(X1max - X1min)/(Q-1):(X1max - X1min),...
31.                         0:(X2max - X2min)/(Q-1):(X2max - X2min));
32.
33. F1int=idw([BIGDATA(:,1),BIGDATA(:,2)],BIGDATA(:,3),[X1int(:),X2int(:)],1,inf,24);
34. figure(1)
35. contourf(X1int,X2int,reshape(F1int,Q,Q),50);
36. colorbar
37. xlabel('Distance Y(m)');
38. ylabel('Distance X(m)');
39. title('GROUND AND MULTIROTOR SURVEY');
40. legend('Total Counts (cps)');
41. axis equal tight
```

1.8. IDW Open-Source

```
1.  function Fint = idw(X0,F0,Xint,p,rad,L)
2.  if nargin < 6
3.     L = 2;
4.     if nargin < 5
5.        rad = inf;
6.        if nargin < 4
7.           p = 2;
```

```
        end
    end
end
% Basic dimensions
N = size(X0,1); % Number of samples
M = size(X0,2); % Number of variables
Q = size(Xint,1); % Number of interpolation points
% Inverse distance weight output
Fint = zeros(Q,1);
for ipos = 1:Q
    % Distance matrix
    DeltaX = X0 - repmat(Xint(ipos,:),N,1);
    DabsL = zeros(size(DeltaX,1),1);
    for ncol = 1:M
        DabsL = DabsL + abs(DeltaX(:,ncol)).^L;
    end
    Dmat = DabsL.^(1/L);
    Dmat(Dmat==0) = eps;
    Dmat(Dmat>rad) = inf;

    % Weights
    W = 1./(Dmat.^p);

    % Interpolation
    Fint(ipos) = sum(W.*F0)/sum(W);
end
end
```